Geochemical and Isotopic Evolution of Late Oligocene Magmatism in Quchan, NE Iran

H. S. Moghadam[1,2,3] , Q. L. Li[1] , M. Kirchenbaur[4], D. Garbe-Schönberg[5] , F. Lucci[6] , W. L. Griffin[7], and G. Ghorbani[2]

[1]State Key Laboratory of Lithospheric Evolution, Institute of Geology and Geophysics, Chinese Academy of Sciences, Beijing, China, [2]School of Earth Sciences, Damghan University, Damghan, Iran, [3]Now at FB4-Dynamics of the Ocean Floor, GEOMAR, Helmholtz-Zentrum für Ozeanforschung Kiel, Kiel, Germany, [4]Institute of Mineralogy, Geochemistry, Leibniz University Hannover, Hannover, Germany, [5]Institute of Geosciences, CAU Kiel University, Kiel, Germany, [6]Dipartimento di Scienze, Universita "Rome Tre", Rome, Italy, [7]Arc Centre of Excellence for Core to Crust Fluid Systems and GEMOC ARC National Key Centre, Department of Earth and Planetary Sciences, Macquarie University, Sydney, NSW, Australia

Abstract Magmatic activity that accompanied the collision between Arabia and Eurasia at ~27 Ma, provides unique opportunities for understanding the triggers and magma reservoirs for collisional magmatism and its different styles in magmatic fronts and back-arcs. We present new ages and geochemical-isotopic results for magmatic rocks that formed during the collision between Arabia and Eurasia in NE Iran, which was a back-arc region to the main magmatic arcs of Iran. Our new zircon U-Pb ages indicate that collisional magmatism began at ~24 Ma in the NE Iran back-arc, although magmatism in this area started in the Late Cretaceous time and continued until the Pleistocene. The collisional igneous rocks are characteristically bimodal, and basaltic-andesitic and dacitic-rhyolitic components show significant isotopic differences; $\varepsilon Nd(t) = +4.4$ to $+7.4$ and $\varepsilon Hf(t) = +5.4$ to $+9.5$ for mafic rocks and $\varepsilon Nd(t) = +0.2$ to $+8.4$ and $\varepsilon Hf(t) = +3.4$ to $+12.3$ for silicic rocks. The isotopic values and modeling suggest that fractional crystallization and assimilation-fractional crystallization played important roles in the genesis of felsic rocks in the NE Iran collisional zone. Trace element and isotopic modeling further emphasize that the main triggers of the magmatism in NE Iran comprise a depleted to the enriched mantle and the Cadomian continental crust of Iran. Our results also emphasize the temporal magmatic variations in the NE Iran back-arc from Late Cretaceous to Pleistocene.

Plain Language Summary Collisional and postcollisional magmatism are common in most continental arcs, occurring after the closure of oceanic basins and thus during and after the collision between the continental blocks. The best examples of these types of magmatism are reported along the Alpine-Himalayan orogenic belt including the Zagros orogen of Iran, which is the result of a collision between Arabia and Eurasia at ~27 Ma. Subduction-related Late Cretaceous to Late Oligocene and collision-related Late Oligocene to Pleistocene magmatic rocks are abundant in the Iran magmatic front (the Urumieh-Dokhtar magmatic belt) and back-arcs and their occurrences are related to the subduction of Neotethyan oceanic lithosphere beneath central Iran. Collisional magmatism differs in several respects from subduction-related magmatism and can be mainly controlled by a pre-existing depleted mantle as well as an enriched refertilized mantle which can record traces of metasomatism by the previous subduction of altered oceanic crust and overlying sediments. Continental crust, which could become thicker during the collision, also plays an important role in the magma genesis. All these parameters were involved during the generation of collisional magmas in the NE Iran back-arc and have been modeled using geochemical and isotopic data.

1. Introduction

Various types of magmatism can occur at different stages of convergence in active continental margins—both in magmatic front and back-arc regions of the continental arcs—changing from tholeiitic, calc-alkaline to high-K calc-alkalic magmatism related to subduction of the oceanic slab to alkaline, ultrapotassic, and adakitic magmatism during continental collision and then orogenic collapse. It has been suggested that magma outpourings in continental arcs comprise combined contributions from the mantle wedge, oceanic

slab and continental crust (Miller et al., 1994; Straub et al., 2010). The relative importance of these contributions is assumed to vary during the lifespan of the continental arcs and can also change after subduction ceases and magmatism is transferred to collisional and postcollisional regimes. In collisional regimes, active subduction has ceased but pre-existing subduction can leave a metasomatized, young sub-continental lithospheric mantle, such as the E-MORB-like mantle that may have been the source of postcollisional magmas in Central Anatolia (Reid et al., 2017). The metasomatized mantle in both subduction- and collision-related settings can be melted to produce a series of magmatic rocks with high concentrations of incompatible elements along with depletion in Nb-Ta, such as shoshonites and/or ultrapotassic rocks (Li et al., 2002; Liu et al., 2014; Tian et al., 2017) and even magmatic rocks without depletion in Nb-Ta such as the igneous rocks from the Argentinian back-arc region (in contrast to the Chilean volcanic front) of the southern Andean magmatic system (e.g., Jacques et al., 2013, 2014). Furthermore, the role of the continental crust will increase in arc magmatism in collisional settings with a thickened lithosphere. The role of refertilized lithospheric mantle, and especially continental crust, is expected to increase from the magmatic front to the back-arcs and/or rear-arcs, as observed in central to South America (e.g., Aragon et al., 2013; Sadofsky et al., 2007) and/or Tibet (e.g., Alexander et al., 2019).

There are several ambiguities regarding magmatism in collisional settings such as: (a) What is the relative importance of each compositional reservoir, including mantle and crust, on collisional magmatism (e.g., Chung et al., 2005; Huang et al., 2019; Seghedi et al., 2019)? (b) Do geochemical and isotopic signatures of continental crust overprint the mantle-derived magmas (e.g., Davidson, 1996; Jahn et al., 1999)? Answering these questions is crucial for understanding the role of continental collision in defining the geochemical and isotopic characteristics of erupting magmas. Collision-related igneous rocks can have variable geochemical signatures, ranging from adakitic (high Sr/Y, La/Yb rocks) to shoshonitic and ultrapotassic and rarely, to Oceanic Island Basalt (OIB)-type alkaline rocks (e.g., Chung et al., 2005). The continental collision can also produce bimodal magmatic suites, in which silicic rocks are usually accompanied by basaltic rocks (e.g., Gómez-Tuena et al., 2018; Kelemen & Behn, 2016; Maunder et al., 2016; Mayen et al., 2017).

Recent advances in numerical modeling support the generation of silicic magmas by assimilation and fractional crystallization (AFC) accompanying crustal melting during the intrusion of basaltic melts from the upper mantle, particularly in regions with thickened continental crust (Annen et al., 2006a; Meade et al., 2014; Patchett, 1980). The AFC processes are considered to be the main mechanisms for the formation of silicic magmas with adakitic (high Sr/Y and La/Yb) signatures (Stern & Kilian, 1996; J.-F. Xu et al., 2002; W.-C. Xu et al., 2015). Assimilation and fractional crystallization processes occur at deep crustal levels (∼20–30 km deep)– mostly associated with large intrusions of intermediate to felsic composition in the lower crust; in "deep crustal hot zones" (Annen et al., 2006a; Wan et al., 2018) and/or in mafic zones (Walker et al., 2015), where differentiating mantle-derived magmas interact with pre-existing crust, in MASH (combined Mixing, Assimilation, Storage, and Homogenization) zones.

The close association of the similarly aged basaltic-intermediate and felsic rocks—such as the magmatic calc-alkaline to adakitic rocks recorded from south Quchan in NE Iran—can be used to investigate the role of FC and AFC processes in the formation of felsic and/or adakitic rocks in a collisional setting. The basaltic lavas can be further used to unravel the mantle source of the magmatic precursors. NE Iran is a back-arc magmatic belt that contains Late Cretaceous to Cenozoic magmatic rocks. Silicic magmatic rocks from south Quchan (Figure 1a) occupy an area of ∼2,000–3,000 km² in NE Iran. These rocks are suggested to show a long-lived magmatic activity from Oligocene to Pleistocene (K-Ar ages; Bauman et al., 1983; Shabanian et al., 2012) and are associated with Late Oligocene (24–23 Ma) basaltic-andesitic magmatism in the region. Mafic-intermediate volcanic rocks have been geochemically classified as high-Mg andesites to basalts as well as high-Nb hawaiites and mugearites (Ahmadi et al., 2017), whereas silicic rocks display adakitic signatures (Shabanian et al., 2012). Both basaltic-andesitic and felsic magmatism have occurred in a subduction-related context from Oligocene to Pleistocene time but after the collision between Iran and Arabia that commenced at ∼27 Ma (McQuarrie & van Hinsbergen, 2013). Therefore, these rocks present a "collisional" perspective, and we prefer to use the term "collision-related" (vs. "postcollisional") for describing these rocks, as the collision between Arabia and Iran is still ongoing and these rocks do not occur in a "relaxation" period after the main collisional event ceased.
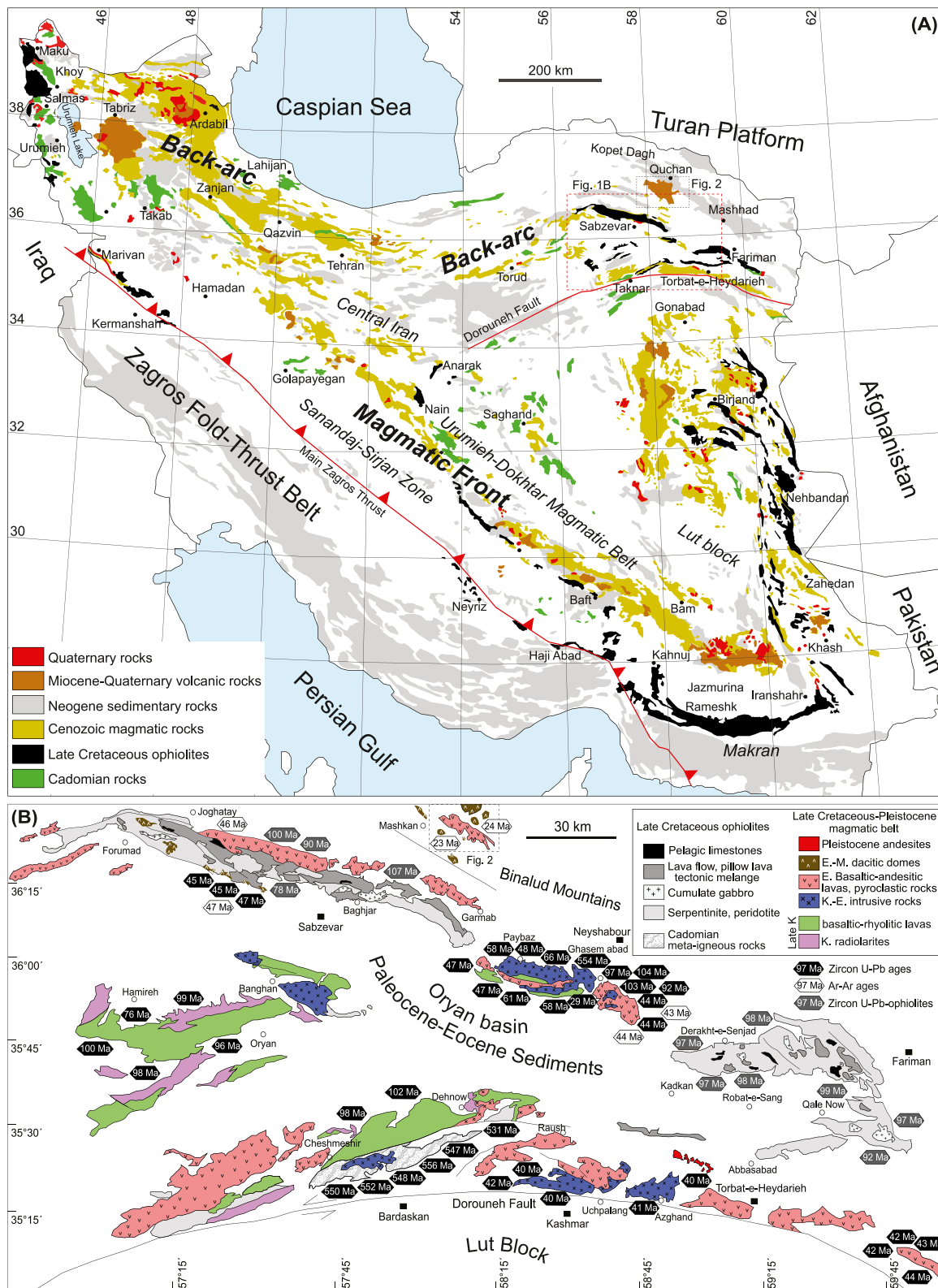
Figure 1. (a) Simplified geological map of Iran emphasizing Ediacaran-Early Cambrian (Cadomian) magmatic rocks, Mesozoic ophiolites and Cenozoic magmatic rocks from the back-arc and magmatic front. (b) Geological map of the Sabzevar-Torbat-e-Heydarieh region, north of the Dorouneh Fault, showing the distribution of ophiolites and Mesozoic-Cenozoic to Pleistocene back-arc rocks. Zircon U-Pb data on ophiolites and magmatic rocks are from Kazemi et al. (2019), Moghadam, Corfu, et al. (2014), Moghadam, Li, Li, et al. (2020), Moghadam, Li, et al. (2015), Moghadam et al. (2016), and Sepidbar et al. (2018). Ar-Ar data are from Ahmadi et al. (2017) and Moghadam, Li, Li, et al. (2020).

In this study, we present the first systematic geochemical, isotopic and geochronological (zircon U-Pb) study of Late Oligocene (~24 Ma) collision-related bimodal magmatism (silicic and mafic rocks) from NE Iran back-arc (south Quchan). The primary goals of this paper are (a) to characterize– based on their geochemical and isotopic signatures– the sources and origin of collision-related mafic magmatic rocks from NE Iran; (b) to understand the role and relationship between fractional crystallization (FC), AFC and recharge, evacuation, and fractional crystallization (REFC) in the genesis of felsic and/or adakitic rocks via their mafic precursors; and (c) to establish in a broader sense the relationships between magmatism, crustal growth and the role of MASH zones in generating silicic and adakitic rocks within continental arcs. This study has the potential to bring about a step-change in assessing the causes of the geochemical-isotopic variations in collisional magmatism of NE Iran, which can be tapped from the lithospheric mantle and the Late Neoproterozoic-Early Paleozoic continental crust of Iran.

2. Geological Setting

The backbone of the Arabia-Eurasia collision zone, the Zagros orogen, was built through Neotethyan subduction, magmatism and collision between several continental blocks including Iran and Anatolia (Berberian & King, 1981). These continental blocks have an Ediacaran-Early Paleozoic (Cadomian) crust and have been rifted from Gondwana in Late Paleozoic time and accreted to Eurasia during Triassic-Jurassic time (Stampfli & Borel, 2002). The Cadomian magmatic rocks exposed in several segments of Iran (Figure 1a) have ages of 620–500 Ma (Moghadam et al., 2021). The rifting of Gondwana in the Late Paleozoic (Permian) caused the opening of the Neotethyan ocean in western parts of the Iranian blocks and the consumption of Paleotethys in the northeastern parts (Berberian & King, 1981). The collision between the Iranian continental blocks and Eurasia during Triassic time led to the closure of the Paleotethyan ocean. The subduction of the Paleotethyan oceanic lithosphere beneath Eurasia (Turan platform) and then collision between the Iranian continental blocks and Eurasia are marked by the presence of a Late Paleozoic suture zone (Late Paleozoic ophiolites through Mashhad to Fariman), Carboniferous-Permian arc magmatism and Late Triassic collisional I- and S-type granites in NE Iran (Alavi, 1991; Mirnejad et al., 2013; Zanchetta et al., 2013). There was a passive margin along western Iran from Late Triassic to Early Cretaceous time, with accommodation of Jurassic continental and Early Cretaceous marine sediments leading to collapse of this margin (Azizi & Stern, 2020; Azizi et al., 2018), and then subduction initiation in Late Cretaceous. The subduction initiation along western Iran (Main Zagros Thrust, Figure 1) led to the opening of several back-arc basins such as the Late Cretaceous Sabzevar-Torbat-e-Heydarieh basin.

Igneous activity in Iran has been continuous from Late Cretaceous (~110 Ma) up to the Pleistocene as a result of the subduction of the Neotethyan oceanic crust beneath Iran from Late Cretaceous to Oligocene and then through the collision between Arabia and Iran from ~27 Ma onward (McQuarrie & van Hinsbergen, 2013). The subduction was accompanied by the development of a continental (Andean-type) magmatic arc, parallel to but ~150–200 km from the Zagros suture zone (Main Zagros Thrust), known as the Urumieh-Dokhtar Magmatic Belt (UDMB) (Figure 1a). The UDMB thus outlines the magmatic front (MF) of the Neotethyan subduction. Magmatic rocks are also abundant in northwestern to northeastern parts of the UDMB and are considered as the products of a back-arc (BA) magmatism. Previous geochronological data suggest the UDMB experienced magmatic flare-ups in the Eocene (~54 Ma until 37 Ma, subduction-related magmatism) and the Miocene (20–5 Ma, collision-related magmatism) (Chiu et al., 2013; Verdel et al., 2007). However, recent data show that the high magmatic fluxes did not occur at the same time in the magmatic front and back-arcs. The UDMB (the magmatic front) magmatism seems to be subdivided into two distinct episodes: ~80–70 Ma and ~50 Ma present, with protracted magmatic activity lasting from 40 Ma to the present (Sepidbar et al., 2019), while the back-arc magmatic flare-ups occurred at 110–80 and 75–35 Ma in the NE Iran back-arc and 55–35 Ma in the NW Iran back-arc (Moghadam, Li, Li, et al., 2020).

Collisional and postcollisional igneous rocks occur widely along the entire length of the collision zone (e.g., Allen et al., 2013; Kheirkhah et al., 2013, 2015; Neill et al., 2013). The initiation of postcollisional magmatism in Iran and Anatolia is suggested to occur diachronously, at 15–11 Ma (Lin et al., 2020). The last magmatic expressions in the Iranian plateau seem to be OIB-type (HIMU-like) basaltic edifices (e.g., Allen et al., 2011; Kheirkhah et al., 2015), although other lithologies including ultrapotassic rocks and adakites have been also reported (e.g., Pang et al., 2015, 2016).

Below we subdivide the Cenozoic Iran arc into the magmatic front and the NE Iran back-arc and discuss these sub-provinces separately.

2.1. Magmatic Front

The UDMB is a 50–80 km wide volcano-plutonic belt that defines the magmatic front and trends NW-SE for >1,000 km across Iran between 28° and 39°N (Figure 1). The UDMB evolved for ~80 m.yr. from when subduction began underneath the Iranian Plateau in Late Cretaceous time, continuing as a mature arc in Paleogene with a magmatic flare-up during the Eocene (Verdel et al., 2011), before swapping magmatic style into collisional high magmatic fluxes following the collision with Arabia during Late Oligocene (~27 Ma). The UDMB arc started with the eruption of low-K tholeiitic and calc-alkaline magmas. A magmatic lull occurred during the Early Paleocene time, accompanying the uplift of the Zagros forearc ophiolites (Moghadam & Stern, 2011). The uplift is evidenced by the presence of lower Paleocene conglomerates, rich in ophiolitic fragments, which cover the ophiolites and are also present in the UDMB. The magmatism restarted in the Middle-Upper Paleocene with the eruption of pyroclastic rocks and lavas. Middle to Late Paleocene igneous rocks have calc-alkaline characteristics and most of them show mantle-like juvenile isotopic signatures (Moghadam, Li, Li, et al., 2020). Eocene igneous rocks are abundant and dominantly high-K calc-alkaline. Late Miocene to Pleistocene UDMB igneous rocks have adakitic and ultrapotassic geochemical signatures (Pang et al., 2015, 2016). Miocene adakitic lavas are mainly present in the UDMB and are interpreted as products of melting of the eclogitic parts of a thickened lower continental crust in a postcollisional setting (e.g., Deng et al., 2018; Wan et al., 2018).

2.2. Back-Arc Magmatism in NE Iran

Back-arc igneous activity occurred along an NW-NE arcuate belt >1,200 km long (Figure 1a) during the latest Cretaceous to Pleistocene, with the eruption of marine to subaerial magmatic rocks, including thick sequences of marine pyroclastic rocks (Ballato et al., 2011; Verdel et al., 2011). Magmatism in the NE Iran back-arc started in the latest Cretaceous and continued through the Paleogene-Neogene to the Pleistocene. The Late Cretaceous to Neogene magmatic rocks are distributed north and south of the Sabzevar-Torbat-e-Heydarieh ophiolitic belt, but also intrude the ophiolites to the north and south (Figure 1b). The Sabzevar-Torbat-e-Heydarieh ophiolites are considered as fragments of a Late Cretaceous back-arc oceanic basin associated with subduction initiation along what is now the Zagros orogen. Late Cretaceous igneous rocks with zircon U-Pb ages of 104–92 Ma are abundant in the NE Iran back-arc (Figure 1b) (Alaminia et al., 2013; Kazemi et al., 2019). The Late Cretaceous sequence is largely marine, comprising low to high-K calc-alkaline rhyolitic to dacitic-andesitic lavas, felsic tuffs and radiolarites. Subaerial lavas including alternating basalts-andesites and dacites are also common. These are overlain by both Middle Paleocene-Eocene terrigenous sediments (Oryan basin; Figure 1b) and Mid-Late Paleocene-Eocene acidic to intermediate pyroclastic rocks with intercalated basaltic to andesitic lavas. In the NE back-arc, Late Cretaceous intrusions (104–76 Ma) were emplaced into thick sequences of Cretaceous terrigenous sediments as well as pyroclastic and volcanic rocks (Mazhari et al., 2019).

A thick pile of magmatic rocks in the NE Iran back-arc occurred after the emplacement and exhumation of the Sabzevar-Torbat-e-Heydarieh ophiolites in the Latest Cretaceous-Middle Paleocene time. The postophiolite subduction-related magmatism started in the Mid-Late Paleocene with the eruption of pyroclastic rocks and interlayered lavas and continued to the Early Eocene with the outpouring of basaltic to andesitic melts. Intermediate to felsic plutonic rocks with Latest Cretaceous-Paleocene (66–58 Ma) ages also occur in NE Iran back-arc (Figure 1b). Latest Cretaceous-Paleocene plutonic rocks have low-K tholeiitic to calc-alkaline geochemical signatures, and their radiogenic bulk rock Nd and zircon Hf isotope characteristics suggest derivation from a depleted mantle (Moghadam, Li, Li, et al., 2020). Eocene volcanic and plutonic rocks (47–40 Ma) are mostly high-K calc-alkaline, but adakitic rocks are also common. These rocks show traces of AFC processes within the middle-upper crust (Moghadam, Li, Li, et al., 2020).

Collisional magmatism in the NE Iran back-arc began at 27 Ma and continued to the Late Miocene (~10 Ma) and even to the Pleistocene (Kheirkhah et al., 2015). Most of the collision-related mafic to felsic volcanic rocks in the back-arc region of NE Iran occur south of Quchan and also in W-NW Sabzevar (Rostami-Hossouri

et al., 2020) (Figure 1a). Pleistocene subaerial andesites also occur north Torbat-e-Heydarieh. The felsic rocks in south Quchan appear both as volcanic domes 1–4 km wide and as lava flows with K-Ar ages of 19.5 ± 0.5 to 2.3 ± 0.1 (Ghasemi et al., 2010). The felsic rocks are accompanied by andesitic to basaltic lava flows. The volcanic domes are intruded into Eocene, but occasionally Miocene, volcano-sedimentary sequences including sandstones, marls, tuffites and shales (Figure 2). Lava flows rest on Miocene red shales and marls. There are xenoliths of sedimentary hosts within the felsic rocks, which suggest assimilation of the crustal rocks and contamination of the magma. Volcanic rocks are also covered by Pliocene-Pleistocene un-sorted conglomerates. Geochemically the felsic rocks have adakitic signatures and were generated during local tectonic activity in NE Iran-Kopet Dagh (Bauman et al., 1983; Shabanian et al., 2012). Mafic rocks were suggested to include high-Mg andesites to basaltic as well as high-Nb hawaiites and mugearites and show ^{40}Ar-^{39}Ar ages of 23.1 ± 0.3 and 22.9 ± 0.5 Ma (Ahmadi et al., 2017). Dacitic lava flows yielded ages of 24.1 ± 0.4 and 23.2 ± 0.5 Ma (Ahmadi et al., 2017).

3. Analytical Procedures

This paper deals with the Late Oligocene volcanic (both mafic and felsic) rocks from south Quchan. We also compare our results with compiled data on the Late Cretaceous-Pleistocene magmatic rocks of NE Iran (Moghadam, Li, Li, et al., 2020). We have used six main analytical procedures: (a) JEOL wavelength-dispersive electron probe X-ray micro-analyzer (JXA 8800R) to determine the composition of minerals at Institute of Geology and Geophysics (IGG-CAS), China; (b) X-Ray Fluorescence (XRF) and Inductively Coupled Plasma-Mass Spectrometry (ICP-MS) for whole-rock major- and trace-element analyses at Institute of Geosciences, Kiel University, Germany; (c) Cathodoluminescence imaging of zircons at IGG-CAS; (d) Secondary-ion microprobe (SIMS) analysis for U-Pb zircon ages at IGG-CAS; (e) Multi-Collector Inductively Coupled Plasma-Mass Spectrometry (MC-ICP-MS) to analyze zircon Lu-Hf isotopes at IGG-CAS; (f) The Sr-Nd-Hf-Pb whole-rock isotope composition of the bulk rocks were analyzed using a MC-ICP-MS at University of Bonn/Köln. We have studied >70 samples petrographically; 26 were used for whole-rock chemical analysis, 4 for SIMS U-Pb zircon ages and zircon Lu-Hf analysis and 21 for Sr-Nd-Pb-Hf isotopes. We have selected fresh samples for whole-rock geochemistry. We sampled different geographic locations to cover all rock units from all parts of the studied area. Analytical details are described in Supporting Information S1.

4. Results

4.1. Sample Descriptions

Our Late Oligocene samples from NE Iran include basalts, olivine basalts, andesites and dacites-rhyolites (Figure 2). Olivine basalts contain clinopyroxene phenocrysts and large crystals of olivine (∼2–3 mm), with interstitial plagioclase laths (Figures S1a and S1b), whereas basalts comprise clinopyroxene and plagioclase with fine-grained olivine in the groundmass. The groundmass of the investigated samples is dominated by clinopyroxene + plagioclase lath + Fe-Ti oxides + glass ± olivine. Olivine in the basaltic rocks is fresh in most cases and contains inclusions of alumina-rich spinel. Andesitic rocks contain more plagioclase and clinopyroxene microphenocrysts than basalts, without olivine. Iron-titanium oxides occur in small amounts (<2 vol.%) in andesites. These mafic rocks show holocrystalline to intergranular texture. Some andesites contain plagioclase + sanidine microlites and clinopyroxene microphenocrysts and show trachytic textures. Amphibole is absent in olivine basalts but occurs as rare needles in the groundmass of andesites and rarely in basalts.

Most felsic rocks have dacite and rhyolitic composition. Dacites contain plagioclase and sanidine phenocrysts with rounded quartz. Modal abundances of quartz and sanidine phenocrysts are higher in the rhyolites than in the dacites. Plagioclases are zoned and show sieve texture in the cores (Figures S1c and S1d). Zoned amphiboles with resorbed rims are also present in dacites (Figures S1e and S1f). The groundmass of dacites contains glass, plagioclase microlites, sanidine and quartz. Dacites and rhyolites show hyaloporphyritic and microlitic to cryptocrystalline textures.

4.2. Mineral Geochemistry

We have analyzed olivine, pyroxene, plagioclase, amphibole and oxides from Late Oligocene basalts and dacites. Olivine phenocrysts in basalts have forsterite contents of 69.7%–85%. Olivine shows zonation; the cores
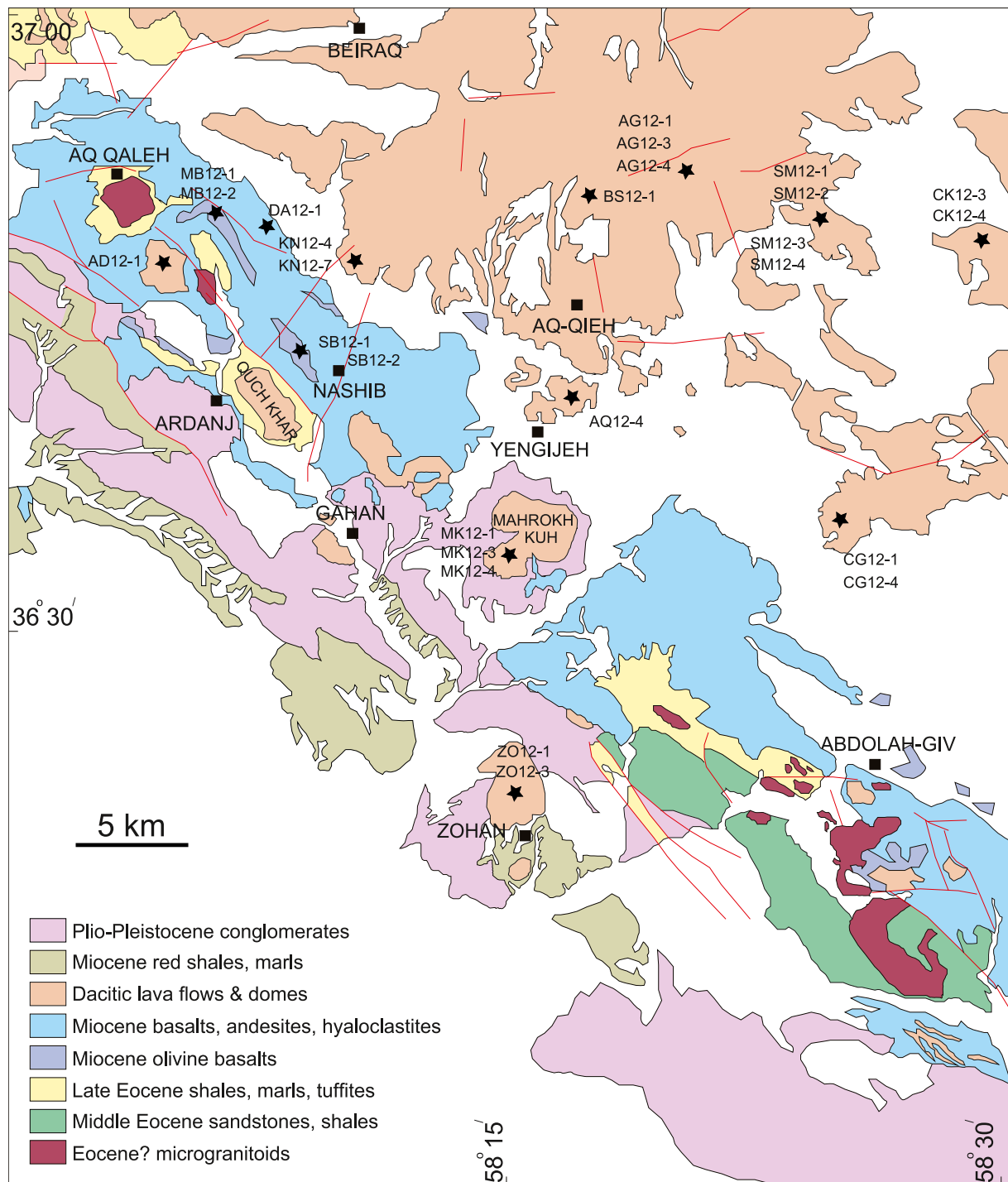
Figure 2. Simplified geological map of Quchan (Mashkan) showing the location of samples selected for geochemistry (modified after the geological 1/100,000 map of Mashkan, Geological Survey of Iran [Gamshidi et al., 2000]).

of olivine crystals have higher forsterite content (Fo ~85%) than their rims (Fo ~69.7%). Their NiO content varies from 0.04 to 0.15 wt%. Clinopyroxene in basalts is diopside (Figure 3a). The cores of the plagioclase phenocrysts in basalts have compositions from bytownite to labradorite (An = 50.7–81.5) (Figure 3b), except for some grains which show andesine (An = 47.1–48.4) composition toward the rims. Some plagioclase from sample MB12-1 also shows more sodic compositions toward the rims (An = 17.6–26.1) with high K_2O
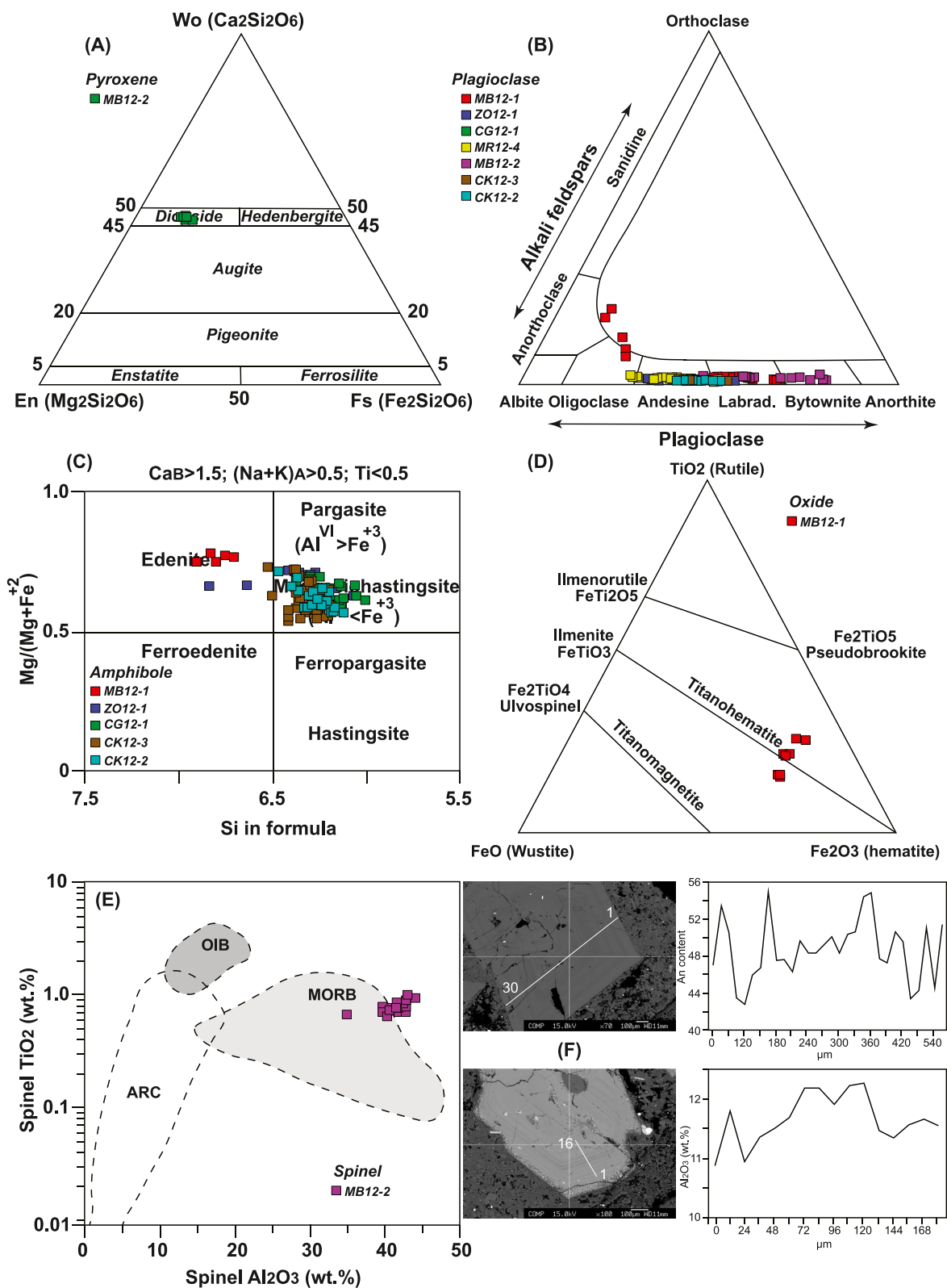
Figure 3.
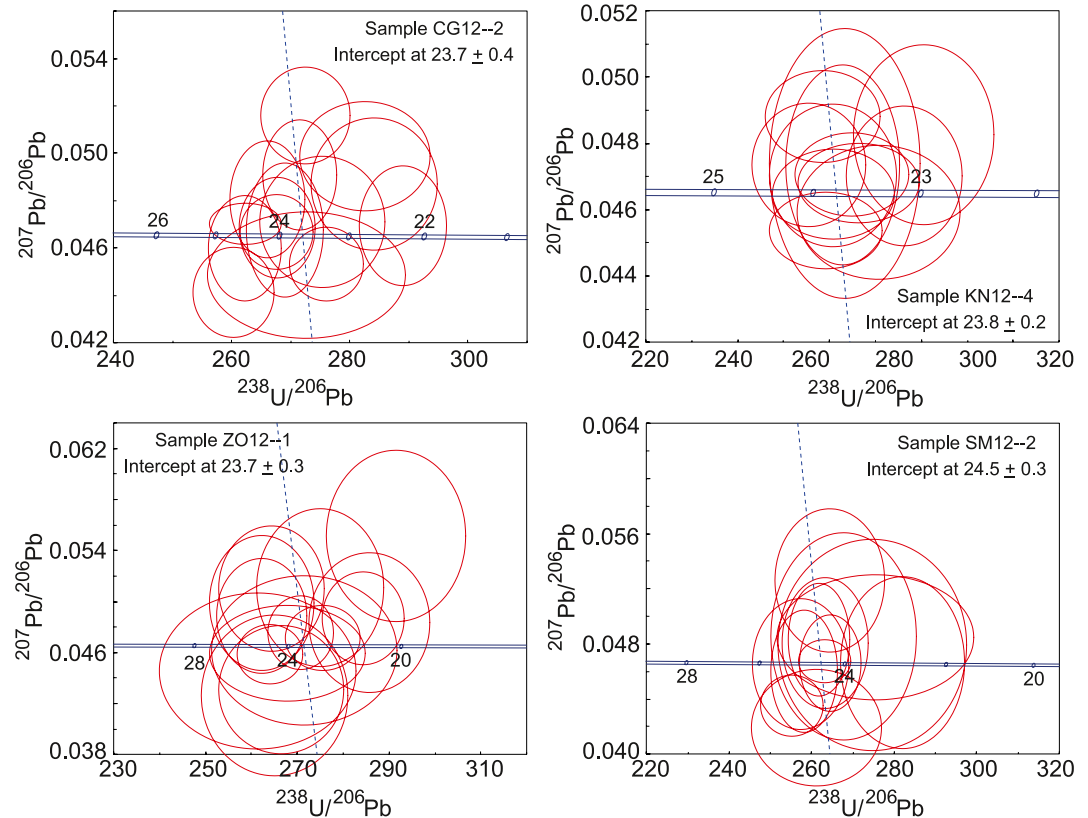
Figure 4. U-Pb inverse-Concordia diagrams ($^{207}Pb/^{206}Pb$ vs. $^{238}U/^{206}Pb$) for zircons from Quchan dacites and rhyolites.

content (Figure 3b). Plagioclase from dacites has oligoclase to labradorite composition (An = 29–56.3) and displays oscillatory zoning. The anorthite content is variable within each compositional band (Figures 3f and S2). Most amphibole phenocrysts in dacites have a pargasite composition whereas amphibole in basalts shows an edenitic signature (Figure 3c).

Amphiboles also show oscillatory zonation and Al_2O_3 content varies in different bands (Figure S2). There seem to be two different amphiboles in dacites; one group has high-Mg cores, while the second type shows low-Mg cores; both show oscillatory zoning toward the rim (Figure S2). Oxide micro-phenocrysts in basalts are compositionally similar to titanohematite. Spinel in basalts occurs as inclusions in olivine phenocrysts and has high Al contents (Cr#; 0.21–0.23). In a TiO_2 versus Al_2O_3 diagram, the spinels have similarities to spinel from mid-oceanic ridge basalts (MORB) (Figure 3e).

4.3. Zircon U-Pb Ages

We have dated four samples from dacitic domes and lavas from the NE Iran back-arc. Sample CG12-2 is from a dacitic dome. Zircons from this sample are medium-to coarse-grained (~80–100 µm) and show oscillatory zoning. Seventeen analyses from this sample show an intercept age of 23.7 ± 0.4 Ma (Figure 4). Two inherited cores give ages of 98 and 224 Ma. These inherited cores show the assimilation of older rocks by the Quchan Oligocene magmas. The common-lead content of the zircons is $f_{206} < 2.4\%$.

Figure 3. (a) En-Wo-Fs classification diagram (Morimoto, 1988) for clinopyroxenes in Quchan basalts. (b) Triangular plot for classification of the Quchan feldspars (Deer et al., 1992). (c) Mg/Mg + Fe^{+2} versus Si cation binary plot (Leake, Woolley, Arps, et al., 1997) for the classification of Quchan amphiboles. (d) Triangular TiO_2-FeO-Fe$_2O_3$ plot for the classification of Quchan Fe-Ti oxides (Deer et al., 1992). (e) TiO_2 versus Al_2O_3 diagram (Kamenetsky et al., 2001) for discrimination of spinels from Quchan basalts. (f) Compositional profiles for anorthite content in plagioclase (upper panel) and Al_2O_3 in amphibole (lower panel) from Quchan dacites.

Table 1
X-Ray Fluorescence Bulk-Rock Analyses of the Quchan (NE Iran Back-Arc) Volcanic Rocks

Sample	DA 12-1	CG 12-4	MB 12-1	MB 12-2	SB 12-1	SB 12-2	AG 12-3	AQ 12-4	AD 12-1	BS 12-1	KN 12-4	KN 12-7	CG 12-1
Rock type	Basalt	Basalt	Basalt	Basalt	Andesite	Andesite	Andesite	Dacite	Dacite	Dacite	Dacite	Dacite	Dacite
GPS (N)	N36,48,34	N36,37,43	N36,49,21	N36,49,21	N36,43,17	N36,43,17	N36,40,36	N36,53,12	N36,51,17	N36,51,59	N36,46,58	N36,46,58	N36,37,43
GPS (E)	E58,08,46	E58,26,44	E58,07,19	E58,07,19	E58,25,53	E58,25,53	E58,22,19	E58,18,11	E58,06,07	E58,17,36	E58,10,10	E58,10,10	E58,26,44
SiO_2	53.41	49.10	48.21	47.91	58.01	58.18	61.15	66.17	66.23	68.02	66.92	67.55	65.37
Al_2O_3	16.87	15.51	17.19	17.16	17.52	17.51	16.60	16.20	16.18	15.84	15.96	15.95	15.91
Fe_2O_3	7.00	12.98	8.92	8.86	5.92	5.84	5.23	3.24	2.62	2.62	2.83	2.88	2.30
MnO	0.11	0.37	0.14	0.14	0.08	0.09	0.06	0.05	0.02	0.05	0.04	0.06	0.02
MgO	5.18	5.04	7.11	6.78	4.17	3.87	3.67	1.55	1.25	0.61	1.46	1.36	2.16
CaO	5.96	5.93	7.98	8.71	6.93	6.90	3.22	4.02	4.43	4.15	4.11	4.05	7.00
Na_2O	5.20	4.23	4.44	4.21	3.71	3.68	5.12	3.76	6.33	4.12	4.00	4.05	3.38
K_2O	1.62	1.33	1.32	1.34	1.15	1.17	1.18	1.80	0.42	1.83	1.74	1.76	0.16
TiO_2	1.09	2.80	1.54	1.54	0.70	0.71	0.77	0.37	0.51	0.33	0.34	0.34	0.39
P_2O_5	0.49	0.34	0.45	0.45	0.25	0.25	0.22	0.15	0.23	0.11	0.10	0.10	0.13
SO_3	0.16	0.18	0.15	0.15	0.13	0.13	0.11	0.12	0.13	0.10	0.09	0.08	0.08
L.O.I.	2.18	1.02	1.81	2.21	0.30	0.42	2.36	1.56	1.02	0.70	0.87	0.76	3.20
Total	99.48	99.14	99.48	99.70	99.04	98.90	99.81	99.14	99.51	98.63	98.61	99.08	100.20

Sample ZO12-1 is taken from a dacitic lava flow. Zircons from this sample are coarse-grained (~100–150 μm). Most zircons show oscillatory zonation, although some of them are weakly zoned. Fifteen analyses were obtained from this sample. Common-lead content is low in most grains; with $f_{206} < 1.5\%$. Some grains have a higher common lead with $f_{206} = 2.6$–5.4. Zircons from this sample show an intercept age of 23.7 ± 0.3 Ma (Figure 4).

Sample KN12-4 is from a dacitic dome. Zircons from this sample are medium-to coarse-grained (~80–130 μm) with oscillatory zoning, although some zircons have only weak oscillatory zonation. Seventeen analyses from magmatic zircons show an intercept age of 23.8 ± 0.2 Ma (Figure 4). The common-lead content of magmatic zircons from this sample is $f_{206} < 2.8$.

Sample SM12-2 is taken from a dacitic dome. Fifteen analyzed magmatic zircons with oscillatory zonation show an intercept age of 24.5 ± 0.3 Ma, which is interpreted to be the crystallization age of this sample. The zircons have a common lead with $f_{206} < 5.4$.

The new ages obtained in this study range from ~25 to 24 Ma (Late Oligocene), which is in accordance with the reported ^{40}Ar-^{39}Ar ages (23–24 Ma; Ahmadi et al., 2017) for mafic and felsic rocks. However, some felsic volcanic rocks/domes seem to have younger K-Ar ages of 19.5 ± 0.5 to 2.3 ± 0.1 (Ghasemi et al., 2010).

4.4. Bulk Rock Geochemistry

The Oligocene magmatic rocks from Quchan have mafic and felsic compositions and are represented by basaltic to andesitic rocks ($SiO_2 = 47.9$–61.2 wt%) and dacites to rhyolites ($SiO_2 = 65.4$–70.9 wt%) (Table 1). In plots of total alkalis ($K_2O + Na_2O$) versus silica (SiO_2) (TAS diagram– Figure 6a), these rocks range across fields from trachy-basalts and trachy-basaltic andesite to andesite, dacite and rhyolite.

Mafic lavas contain 5–7.1 wt% MgO, <102 ppm Ni, <26 ppm Sc, and <169 ppm Cr (Table 2), indicating that these lavas do not represent primary magma compositions, but have instead undergone significant crystal fractionation. Felsic rocks have 0.4–2.2 wt% MgO, with low <30 ppm Cr and <10 ppm Ni. Mineral fractionation trends can be seen in plots of SiO_2, P_2O_5, Sc, Ni, V, Nb, Sr, and Y versus MgO for Quchan mafic and felsic magmatic rocks (Figure 5). In these plots, with decreasing MgO content the abundances of all these

CK 12-3	CK 12-4	ZO 12-1	ZO 12-3	AG 12-4	SM 12-1	SM 12-2	SM 12-4	SM 12-3	MR 12-1	MR 12-3	MR 12-4	AG 12-1
Dacite	Dacite	Dacite	Dacite	Dacite	Dacite	Dacite	Dacite	Dacte	Rhyolite	Rhyolite	Rhyolite	Rhyolite
N36,48,42	N36,48,12	N36,41,46	N36,41,46	N36,40,06	N36,47,09	N36,47,09	N36,47,30	N36,47,09	N36,45,54	N36,45,54	N36,45,54	N36,40,36
E58,31,16	E58,31,46	E58,14,23	E58,14,23	E58,29,29	E58,24,30	E58,24,30	E58,26,47	E58,24,30	E58,13,51	E58,13,51	E58,13,51	E58,22,19
69.39	67.49	69.03	68.99	69.65	68.76	69.59	67.66	66.93	70.95	70.84	70.89	70.54
16.15	15.97	16.10	16.20	16.40	16.25	16.41	15.91	15.75	15.91	15.88	15.86	15.24
2.16	2.88	2.10	2.06	1.92	1.92	2.00	2.78	1.87	1.80	1.88	1.83	1.84
0.04	0.05	0.04	0.04	0.04	0.04	0.04	0.03	0.02	0.04	0.04	0.04	0.01
0.75	1.34	0.86	0.87	0.88	1.05	0.91	1.06	1.90	0.56	0.54	0.65	0.36
3.80	4.19	3.86	3.83	3.99	4.47	4.03	4.16	6.38	3.20	3.17	3.32	3.80
4.37	4.25	4.37	4.37	4.51	4.34	4.44	4.10	3.89	4.43	4.42	4.48	4.08
1.58	1.76	1.72	1.67	1.37	1.48	1.45	1.81	0.42	1.95	2.00	1.97	1.68
0.28	0.37	0.27	0.27	0.25	0.25	0.25	0.35	0.37	0.23	0.24	0.24	0.22
0.09	0.11	0.10	0.10	0.09	0.09	0.09	0.11	0.13	0.08	0.09	0.09	0.07
0.10	0.11	0.15	0.10	0.07	0.11	0.09	0.13	0.10	0.09	0.08	0.13	0.08
0.51	0.76	0.47	0.45	1.07	0.77	0.27	1.02	0.45	0.33	0.35	0.39	1.56
99.37	99.44	99.21	99.09	100.38	99.69	99.71	99.27	98.35	99.70	99.66	100.04	99.58

elements decrease from mafic rocks toward felsic rocks, except for SiO_2 which increases. Dacite sample AD12-1 has a high Nb content (26.3 ppm), similar to basalts. These trends could reflect fractionation of ferromagnesian minerals such as olivine, pyroxene and amphibole as well as apatite and Fe-Ti oxides. The high Nb content in sample AD12-1 could be related to higher levels of contamination with continental crust (see next section).

The Quchan volcanic rocks are mostly calc-alkaline (Figure 6b). They have both low and high Sr/Y and $La_{(n)}/Yb_{(n)}$ ratios (19.4–71.9 and 3.8–20.2, respectively). Most felsic volcanic rocks have adakitic signatures in plots of Sr/Y versus Y and $La_{(n)}/Yb_{(n)}$ versus $Yb_{(n)}$ (Figures 6c and 6d), except for samples AD12-1, AG12-1, AG12-4, and CG12-1. The basalts are similar to normal arc-related rocks.

We have normalized the rare earth- and trace-elements data from Quchan rocks to chondrite and N-MORB. In the N-MORB-normalized diagram, we have followed the order of trace-element incompatibility in MORBs and oceanic basalts proposed by (Sun & McDonough, 1989). In an N-MORB-normalized diagram, dacites and rhyolites are enriched in LREE ($La_{(n)}/Yb_{(n)} \sim 8.6$–36.3) (Figure 7a), with negative anomalies in Nb, Ta, and Ti (e.g., $Nb_{(n)}/La_{(n)} \sim 0.4$–1.1) and positive anomalies in Sr, Ba, Th, and U (e.g., $Th_{(n)}/La_{(n)} \sim 5.1$–9.9) (Figure 7b). Dacites and rhyolites have no significant Eu anomaly while also displaying a spoon-shaped MREE-HREE pattern (Figure 7b). Andesites and basalts are also enriched in LREE compared to HREE with $La_{(n)}/Yb_{(n)} \sim 6.7$–24.5 (Figure 7c). These rocks are also depleted in Nb-Ta (e.g., $Nb_{(n)}/La_{(n)} \sim 0.6$–1.1) and enriched in Rb, Th, U, and Sr (e.g., $Th_{(n)}/La_{(n)} \sim 2.5$–10.8) (Figure 7d). However, some dacites (adakitic samples SM12-3 and ZO12-3) and basalts (sample MB12-2) do not show depletion in Nb-Ta. The contents of incompatible elements including large ion lithophile elements (LILEs) and high field strength elements (HFSEs) are high in Quchan back-arc volcanic rocks, compared to N-MORBs., whereas heavy rare earth elements (HREEs) show depletion.

4.5. Radiogenic Isotopes

We analyzed Late Oligocene volcanic rocks for Sr-Nd-Pb-Hf isotopes (Table 3) and dacite-rhyolite zircons for Lu-Hf isotopes. Basalts and andesites show small spreads in initial $^{87}Sr/^{86}Sr_{(t)}$ (0.704–0.705) and $\varepsilon Nd(t)$ values (+4.4 to +7.4). Dacites and rhyolites have initial $^{87}Sr/^{86}Sr_{(t)}$ and $\varepsilon Nd(t)$ values of 0.704–0.705 and +0.2 to +8.4, respectively. In a Sr-Nd isotope correlation diagram (Figure 8a), most Quchan data show a
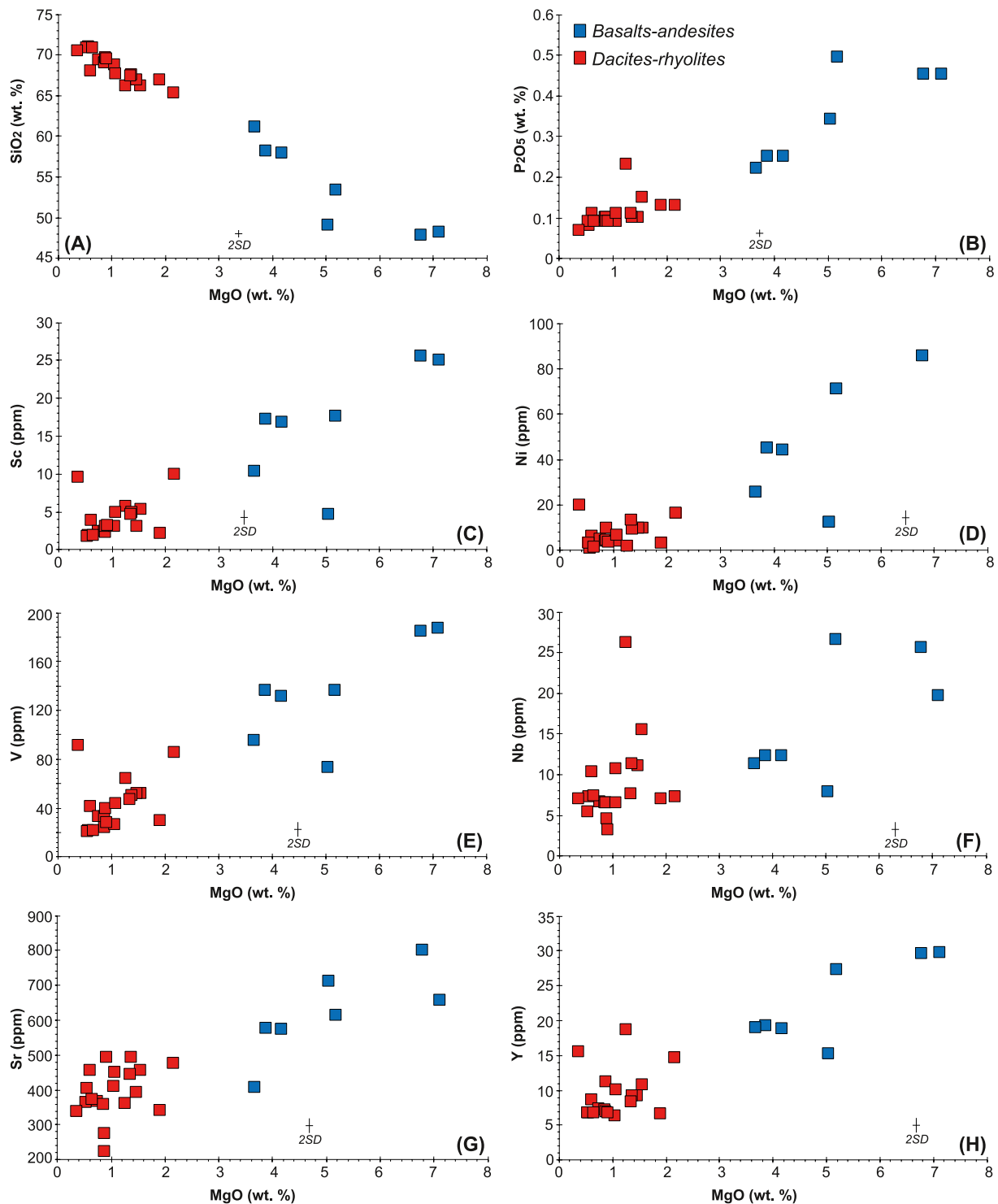
Figure 5. SiO_2, P_2O_5, Sc, Ni, V, Nb, Sr, and Y versus MgO content of the Quchan magmatic rocks. With decreasing MgO, the content of all elements—except SiO_2—show decreasing which could show fractionation of ferromagnesian minerals such as olivine, pyroxene, amphibole, apatite and Fe-Ti oxides.

good negative correlation, although two non-adakitic samples (dacite sample CG12-1 and rhyolite sample AG12-1) have higher $^{87}Sr/^{86}Sr_{(t)}$ at a given $^{143}Nd/^{144}Nd$ and could reflect late-stage processes, e.g., alteration and/or assimilation of altered host rocks such as tuffites or marls and/or biotite-rich Cadomian paragneisses which are abundant in NE Iran. Assimilation of the biotite-rich Cadomian rocks could explain

Table 2
Trace-Element ICPMS Data for Quchan (NE Iran Back-Arc) Volcanic Rocks

Standard and duplicates			Duplicates							
Sample ID (µg/g)	JA-1 Literatur	JA-1	CK 12-3	CK 12-3	CK 12-3	CK 12-3	KN 12-4	KN 12-4	KN 12-4	KN 12-4
Li	10.500	8.706	14.756	14.673	14.730	14.725	16.183	16.290	16.152	16.219
Sc	28.400	19.212	2.394	2.427	2.418	2.425	3.115	3.134	3.153	3.165
V	105.000	111.568	33.265	33.880	33.889	33.885	51.606	52.668	52.945	53.130
Cr	7.300	3.982	9.126	9.333	9.318	9.412	13.423	13.548	13.760	13.811
Co	11.800	9.697	3.507	3.451	3.506	3.450	5.715	5.770	5.751	5.848
Ni	1.800	0.877	5.140	5.206	5.286	5.169	9.800	9.901	9.892	9.952
Cu	42.200	41.783	21.731	21.782	21.881	21.834	31.121	31.144	31.342	31.218
Zn	90.600	88.274	26.884	27.182	27.307	26.915	35.885	36.051	36.174	36.047
Ga	17.300	17.097	15.675	15.719	15.729	15.576	15.767	15.918	15.869	15.942
Rb	11.800	7.443	6.602	6.622	6.572	6.557	12.832	12.570	12.551	12.551
Sr	266.000	243.578	366.301	369.255	378.699	371.628	393.033	391.128	397.223	396.842
Y	30.600	34.549	7.413	7.375	7.413	7.343	9.298	9.279	9.229	9.184
Zr	88.300	82.118	102.635	102.586	102.438	101.795	116.079	116.808	116.808	116.371
Nb	1.700	1.248	6.647	6.652	6.678	6.591	11.150	11.185	11.175	11.125
Cs	0.640	0.605	0.644	0.648	0.651	0.650	0.752	0.749	0.755	0.757
Ba		291.853	402.042	406.342	407.429	410.097	379.189	377.148	386.720	384.048
La	5.100	4.400	9.676	9.680	9.656	9.700	13.731	13.678	13.692	13.731
Ce	13.500	11.669	17.290	17.276	17.325	17.290	26.505	26.272	26.398	26.379
Pr	1.980	1.948	1.982	1.972	1.980	1.974	2.698	2.686	2.681	2.688
Nd	11.000	10.367	7.368	7.323	7.294	7.328	9.849	9.883	9.825	9.800
Sm	3.520	3.327	1.453	1.463	1.438	1.429	1.894	1.883	1.894	1.893
Eu	1.170	1.125	0.485	0.483	0.479	0.480	0.635	0.637	0.632	0.631
Gd	4.360	4.139	1.367	1.365	1.377	1.368	1.781	1.768	1.785	1.767
Tb	0.770	0.716	0.193	0.193	0.191	0.191	0.244	0.246	0.247	0.245
Dy	4.530	4.780	1.081	1.077	1.080	1.080	1.366	1.369	1.374	1.378
Ho	0.940	1.021	0.213	0.216	0.214	0.213	0.269	0.269	0.269	0.268
Er	3.010	2.884	0.599	0.596	0.598	0.599	0.745	0.746	0.742	0.742
Tm	0.480	0.442	0.098	0.098	0.098	0.098	0.119	0.119	0.118	0.118
Yb	2.920	2.954	0.651	0.646	0.644	0.647	0.779	0.775	0.779	0.779
Lu	0.470	0.460	0.106	0.106	0.105	0.105	0.126	0.127	0.125	0.125
Hf	2.410	2.443	2.556	2.561	2.539	2.536	2.796	2.809	2.817	2.801
Ta	0.100	0.094	0.447	0.451	0.447	0.447	0.839	0.842	0.840	0.833
W	3.900	0.441	0.298	0.291	0.290	0.291	0.260	0.258	0.253	0.253
Pb	5.800	5.678	8.105	8.125	8.027	8.073	7.923	7.898	7.836	7.836
Th	0.820	0.690	2.804	2.804	2.766	2.779	5.184	5.180	5.126	5.107
U	0.340	0.358	0.826	0.823	0.816	0.820	1.481	1.476	1.464	1.454

the radiogenic Sr-isotope compositions of some Quchan felsic rocks, but biotite does not have high U/Pb and thus cannot explain the lack of disturbance in the Pb isotopic composition of these rocks. However, sample CG12-1 has higher CaO and LOI contents compared to other dacites, whereas sample AG12-1 has higher LOI relative to other rhyolites, which would be consistent with their high $^{87}Sr/^{86}Sr_{(t)}$ being related to alteration. Sample AD12-1 has higher $^{87}Sr/^{86}Sr_{(t)}$ and lower $\varepsilon Nd(t)$ than other dacites and rhyolites and

Table 2
Continued

Samples	Basalt	Basalt	Basalt	Basalt	Andesite	Andesite	Andesite	Dacite	Dacite	Dacite	Dacite	Dacite
Sample ID (µg/g)	CG 12-4	DA 12-1	MB 12-1	MB 12-2	AG 12-3	SB 12-1	SB 12-2	AD 12-1	AG 12-4	AQ 12-4	BS 12-1	CG 12-1
Li	10.865	30.684	20.802	18.549	33.591	13.253	16.550	11.315	17.914	9.162	9.880	9.731
Sc	4.685	17.701	25.116	25.617	10.406	16.908	17.300	5.669	3.112	5.271	3.819	9.934
V	73.350	136.394	187.499	185.298	95.129	131.340	136.234	64.225	39.355	52.124	41.672	85.400
Cr	19.392	71.359	168.633	116.752	29.395	46.817	72.495	2.773	22.991	13.102	12.453	29.888
Co	1.926	24.261	35.089	32.974	16.288	19.644	19.357	4.018	2.793	6.051	4.672	4.629
Ni	12.504	70.973	102.854	85.660	25.857	44.259	45.133	2.094	9.780	6.597	6.154	16.580
Cu	6.748	20.915	44.168	49.326	28.692	13.886	12.132	5.462	2.561	20.304	20.517	11.547
Zn	6.833	64.402	71.348	72.578	25.722	58.198	58.109	110.974	25.571	57.603	39.639	12.138
Ga	13.241	18.296	16.269	16.067	15.405	17.720	17.900	17.307	13.578	18.036	16.727	14.833
Rb	7.350	39.956	18.229	18.958	22.306	24.207	24.189	2.130	17.006	20.741	16.895	3.401
Sr	712.556	613.607	658.782	800.925	407.422	574.273	576.492	362.514	224.654	456.922	455.564	475.453
Y	15.272	27.352	29.703	29.556	19.058	18.879	19.245	18.672	11.300	10.843	8.640	14.755
Zr	116.435	230.123	202.040	204.766	151.012	150.082	152.726	231.861	108.981	145.202	115.872	110.667
Nb	7.892	26.676	19.749	25.599	11.399	12.293	12.286	26.288	4.642	15.564	10.394	7.335
Cs	0.184	4.294	0.979	0.533	0.666	0.329	0.371	0.180	0.968	0.638	0.384	0.592
Ba	113.813	424.873	272.661	298.188	194.782	250.488	256.210	268.828	216.015	502.842	471.324	75.683
La	7.424	43.275	24.558	24.678	16.180	24.031	24.178	35.975	10.793	25.699	18.304	9.218
Ce	17.529	75.014	48.346	48.574	30.629	40.974	41.199	59.834	17.555	41.441	29.607	19.828
Pr	2.253	7.903	5.751	5.763	3.553	4.429	4.499	6.726	2.105	4.306	3.191	2.486
Nd	9.536	28.318	22.859	23.018	13.866	16.442	16.626	22.887	7.709	14.890	11.394	10.103
Sm	2.195	5.024	4.774	4.806	2.911	3.138	3.199	3.814	1.567	2.501	2.018	2.194
Eu	0.633	1.598	1.632	1.644	0.935	1.030	1.043	1.078	0.474	0.788	0.664	0.671
Gd	2.222	4.964	4.955	4.975	2.991	3.159	3.220	3.515	1.601	2.294	1.841	2.215
Tb	0.341	0.695	0.738	0.742	0.452	0.456	0.467	0.478	0.243	0.299	0.243	0.336
Dy	2.079	4.035	4.414	4.441	2.725	2.702	2.767	2.686	1.484	1.624	1.331	2.049
Ho	0.431	0.798	0.880	0.883	0.554	0.548	0.561	0.528	0.310	0.312	0.257	0.418
Er	1.237	2.191	2.402	2.404	1.551	1.533	1.577	1.466	0.904	0.858	0.693	1.191
Tm	0.200	0.330	0.354	0.356	0.241	0.238	0.242	0.228	0.151	0.133	0.110	0.192
Yb	1.343	2.156	2.315	2.319	1.612	1.587	1.606	1.546	1.052	0.864	0.699	1.310
Lu	0.219	0.337	0.359	0.353	0.256	0.251	0.254	0.247	0.178	0.139	0.113	0.213
Hf	2.757	4.380	3.806	3.852	3.148	3.108	3.129	4.726	2.658	3.292	2.803	2.604
Ta	0.582	0.954	0.700	1.375	0.712	0.723	0.735	1.543	0.342	0.935	0.542	0.525
W	0.253	0.538	0.256	0.289	0.218	0.333	0.462	0.336	0.282	0.420	0.261	0.254
Pb	3.746	4.397	3.020	3.012	4.748	5.406	5.651	17.414	6.046	9.760	8.597	2.849
Th	3.833	8.411	2.977	2.964	3.378	5.825	5.809	12.266	4.088	7.006	5.145	4.392
U	0.893	1.671	0.766	0.773	1.017	1.313	1.286	2.802	0.875	1.812	1.418	0.977

Note. Reference for the analytical procedure: Garbe-Schönberg (1993).

plots toward the Ediacaran-Early Cambrian (Cadomian) crust of Iran. All these non-adakitic samples (CG12-1, AG12-1, and AD12-1) have low Rb (2.1–10.8 ppm) and high Rb/Sr (0.006–0.03) compared to other felsic samples. Rhyolite sample AG12-1 has higher $\varepsilon Nd(t)$ and $\varepsilon Hf(t)$ than mafic rocks. Most Quchan

Dacite	Dacite	Dacite	Dacite	Dacite	Dacite	Dacite	Dacite	Dacite	Dacite	Rhyolite	Rhyolite	Rhyolite	Rhyolite
CK 12-3	CK 12-4	KN 12-4	KN 12-7	SM 12-1	SM 12-2	SM 12-3	SM 12-4	ZO 12-1	ZO 12-3	AG 12-1	MR 12-1	MR 12-3	MR 12-4
14.756	13.813	16.183	19.423	15.826	10.754	8.101	13.412	16.338	13.501	31.066	16.375	12.533	9.730
2.394	4.724	3.115	4.976	3.058	3.234	2.117	4.893	2.467	2.227	9.536	1.844	1.774	1.829
33.265	47.239	51.606	50.449	26.160	28.311	30.031	43.365	33.427	23.661	91.337	21.208	20.665	21.576
9.126	25.146	13.423	18.634	11.011	8.722	4.190	14.316	8.926	10.068	27.948	4.498	4.400	5.904
3.507	6.131	5.715	6.003	3.189	3.084	2.657	5.328	3.352	3.070	11.126	1.582	2.228	1.955
5.140	13.406	9.800	9.389	4.024	3.452	3.229	6.639	3.889	4.560	19.820	0.975	3.103	1.416
21.731	23.927	31.121	23.440	21.060	14.430	16.186	21.920	19.946	20.419	39.621	12.132	11.239	9.619
26.884	36.350	35.885	37.089	30.173	29.365	28.347	39.476	35.250	32.718	43.305	25.512	29.861	27.047
15.675	17.120	15.767	16.974	16.234	16.760	15.976	17.163	16.175	15.947	14.975	16.646	16.459	16.307
6.602	14.524	12.832	26.862	7.802	15.554	4.828	16.611	9.585	5.132	10.752	20.596	18.534	13.609
366.301	443.763	393.033	493.920	410.314	492.916	340.411	450.218	359.503	276.290	338.049	405.535	364.768	373.154
7.413	8.377	9.298	9.281	6.422	6.846	6.639	10.091	7.294	6.954	15.519	6.786	6.852	6.730
102.635	102.262	116.079	116.928	84.473	80.840	89.718	121.312	101.749	101.628	122.088	117.698	93.363	94.950
6.647	7.704	11.150	11.309	6.511	3.208	7.034	10.698	6.608	6.536	7.068	7.341	5.497	7.481
0.644	0.917	0.752	1.228	0.376	0.945	0.800	1.018	0.735	0.520	1.058	0.692	0.770	0.762
402.042	453.569	379.189	430.883	349.163	350.444	298.343	490.809	348.172	318.180	201.888	479.210	484.191	481.493
9.676	12.916	13.731	18.749	10.627	11.584	6.989	18.376	9.108	6.189	12.150	16.312	15.392	13.144
17.290	23.189	26.505	29.635	16.919	17.975	14.279	30.963	15.719	13.045	22.325	25.079	23.795	20.931
1.982	2.427	2.698	3.330	2.013	2.169	1.501	3.226	1.802	1.356	2.639	2.905	2.828	2.473
7.368	8.965	9.849	11.786	7.389	7.825	5.763	11.504	6.729	5.314	10.481	10.101	9.931	8.918
1.453	1.723	1.894	2.110	1.444	1.493	1.246	2.119	1.401	1.183	2.266	1.756	1.783	1.676
0.485	0.568	0.635	0.683	0.496	0.506	0.432	0.683	0.487	0.433	0.711	0.591	0.583	0.555
1.367	1.629	1.781	1.932	1.336	1.387	1.197	1.989	1.318	1.180	2.363	1.522	1.567	1.504
0.193	0.223	0.244	0.258	0.183	0.189	0.170	0.269	0.188	0.171	0.357	0.197	0.203	0.200
1.081	1.252	1.366	1.420	0.989	1.038	0.957	1.507	1.056	0.982	2.184	1.045	1.055	1.044
0.213	0.246	0.269	0.275	0.190	0.198	0.190	0.295	0.208	0.196	0.452	0.200	0.198	0.195
0.599	0.682	0.745	0.754	0.519	0.541	0.515	0.802	0.578	0.549	1.281	0.546	0.534	0.521
0.098	0.108	0.119	0.119	0.083	0.087	0.085	0.126	0.095	0.092	0.201	0.089	0.084	0.085
0.651	0.723	0.779	0.781	0.534	0.561	0.548	0.817	0.628	0.596	1.369	0.573	0.540	0.537
0.106	0.118	0.126	0.125	0.084	0.089	0.089	0.131	0.101	0.098	0.220	0.093	0.086	0.086
2.556	2.571	2.796	2.815	2.296	2.156	2.328	2.979	2.580	2.550	2.846	2.870	2.449	2.468
0.447	0.528	0.839	0.855	0.415	0.178	0.459	0.748	0.367	0.444	0.475	0.515	0.228	0.473
0.298	0.227	0.260	0.276	0.183	0.086	0.203	0.291	0.189	0.170	0.308	0.158	0.112	0.192
8.105	9.394	7.923	9.959	8.828	9.382	8.543	10.545	9.601	7.788	7.893	9.775	9.593	9.150
2.804	3.714	5.184	5.940	2.743	3.078	2.293	5.391	2.681	2.141	3.331	4.000	3.811	3.537
0.826	1.111	1.481	1.544	1.020	1.179	0.890	1.666	1.009	0.924	1.018	1.257	1.119	1.125

rocks plot in a trend defined by Paleocene-Eocene to Pleistocene magmatic rocks of NE Iran (Figure 8a). This trend runs between a depleted mantle (DM), similar to the mantle source of arc tholeiites and the Cadomian continental crust of Iran.

Table 3

Bulk-Rock Sr-Nd-Pb-Hf Isotope Analyses of the Quchan (NE Iran Back-Arc) Volcanic Rocks

Sample	Rock type	$^{206}Pb/^{204}Pb$	(% 1s.e.)	$^{207}Pb/^{204}Pb$	(% 1s.e.)	$^{208}Pb/^{204}Pb$	(% 1s.e.)	$^{143}Nd/^{144}Nd$	2sd	εNd ($t=0$)	$^{87}Sr/^{86}Sr$	2sd	$^{176}Hf/^{177}Hf$	2sd	εHf ($t=0$)	Pb	Th	U
MB 12-1	Basalt	18.479	0.003	15.561	0.003	38.573	0.004	0.512861	0.000007	4.35	0.704364	0.000011	0.283038	0.000005	8.95	3.02	2.98	0.77
MB 12-2	Basalt	18.485	0.002	15.561	0.003	38.580	0.003	0.512854	0.000007	4.22	0.705028	0.000011	0.283044	0.000006	9.16	3.01	2.96	0.77
DA 12-1	Basalt	18.682	0.005	15.596	0.006	38.978	0.006	0.512902	0.000007	5.30	0.704859	0.000009	0.282928	0.000003	5.06	4.40	8.41	1.67
SB 12-2	Andesite	18.513	0.006	15.578	0.007	38.675	0.007	0.513005	0.000008	7.32	0.703977	0.000010	0.283043	0.000004	9.11	5.65	5.81	1.29
AG 12-3	Andesite	18.534	0.002	15.607	0.003	38.679	0.003									4.75	3.38	1.02
SB 12-1	Andesite	18.523	0.002	15.577	0.002	38.695	0.003									5.41	5.82	1.31
AG 12-4	Dacite	18.302	0.002	15.534	0.003	38.325	0.003	0.512894	0.000011	5.00	0.704257	0.000013	0.283121	0.000009	11.89	6.05	4.09	0.87
CG 12-1	Dacite	18.446	0.002	15.562	0.003	38.566	0.003	0.512876	0.000009	4.64	0.705075	0.000010				2.85	4.39	0.98
KN 12-7	Dacite	18.573	0.002	15.606	0.002	38.758	0.003	0.512640	0.000014	0.20	0.704444	0.000011	0.282911	0.000006	4.46	9.96	5.94	1.54
SM 12-2	Dacite	18.523	0.002	15.592	0.002	38.678	0.003	0.512781	0.000018	2.95	0.703990	0.000013	0.283067	0.000006	9.98	9.38	3.08	1.18
AQ 12-4	Dacite	18.598	0.005	15.615	0.006	38.831	0.006	0.512820	0.000008	3.70	0.704474	0.000009	0.282890	0.000004	3.73	9.76	7.01	1.81
CK 12-4	Dacite	18.523	0.002	15.595	0.002	38.678	0.002	0.512842	0.000008	4.14	0.704263	0.000010	0.282997	0.000006	7.49	9.39	3.71	1.11
SM 12-1	Dacite	18.523	0.002	15.593	0.003	38.678	0.003	0.512947	0.000009	6.19	0.704080	0.000010	0.283071	0.000004	10.11	8.83	2.74	1.02
SM 12-4	Dacite	18.559	0.003	15.609	0.003	38.742	0.003									10.54	5.39	1.67
ZO 12-1	Dacite	18.534	0.002	15.594	0.003	38.690	0.003	0.512955	0.000008	6.34	0.704136	0.000010	0.283060	0.000004	9.74	9.60	2.68	1.01
AD 12-1	Dacite	18.748	0.002	15.642	0.002	39.055	0.003	0.512630	0.000007	−0.16	0.705470	0.000011	0.282870	0.000004	3.00	17.41	12.27	2.80
BS 12-1	Dacite	18.554	0.003	15.604	0.003	38.750	0.004	0.512833	0.000010	3.97	0.704315	0.000010	0.282944	0.000003	5.62	8.60	5.14	1.42
MR 12-1	Rhyolite	18.534	0.002	15.591	0.002	38.688	0.003	0.512789	0.000009	2.94	0.704189	0.000013	0.283045	0.000008	9.21	9.77	4.00	1.26
MR 12-3	Rhyolite	18.545	0.003	15.595	0.004	38.707	0.004	0.512967	0.000009	6.58	0.704175	0.000013	0.283053	0.000005	9.49	9.59	3.81	1.12
MR 12-4	Rhyolite	18.543	0.004	15.594	0.004	38.702	0.004	0.512990	0.000010	7.03	0.704340	0.000008	0.283050	0.000004	9.38	9.15	3.54	1.12
AG 12-1	Rhyolite	18.524	0.002	15.602	0.003	38.670	0.003	0.513056	0.000009	8.31	0.704773	0.000008	0.283099	0.000006	11.10	7.89	3.33	1.02
JA-1	Standard							0.513188	0.000021	10.89	0.703526	0.000012	0.283267	0.000005	17.04			

The εHf(t) values for basalts and andesites vary between +5.4 and +9.5. These samples fall both along and below the mantle array in a plot of εHf(t) versus εNd(t) (Figure 8b). The εHf(t) values for felsic rocks range from +3.4 to +12.3. They plot parallel to, but mostly below, the mantle array, in a trend between the depleted mantle and the Cadomian continental crust of Iran. Initial $^{206}Pb/^{204}Pb_{(t)}$ and $^{208}Pb/^{204}Pb_{(t)}$ ratios for basalts and andesites vary from 18.42 to 18.59 and 38.49 to 38.82, respectively. The $^{207}Pb/^{204}Pb_{(t)}$ ratios of these rocks (15.56–15.60) are similar to those of the Paleocene-Eocene magmatic rocks from NE Iran (Figures 8c and 8d). The initial $^{206}Pb/^{204}Pb_{(t)}$ and $^{208}Pb/^{204}Pb_{(t)}$ ratios for dacites and rhyolites vary from 18.27 to 18.71 and 38.27 to 38.40, respectively. The $^{207}Pb/^{204}Pb_{(t)}$ ratio in these felsic samples ranges from 15.53 to 15.64 and are similar to the $^{207}Pb/^{204}Pb_{(t)}$ of Quchan basalts and andesites.

In the thorogenic-Pb isotope plot (Figure 8c), the Quchan igneous rocks fall in a narrow linear array, well above the Northern Hemisphere Reference Line (NHRL) of (Hart, 1984), with Δ8/4 of 75–56 (Figure S3). The samples define a trend between the depleted mantle and Cadomian crust (=CC) reservoirs (Figures 8c and S3). On the uranogenic Pb diagram (Figure 8d), the investigated samples plot above the NHRL (Δ7/4 to 6–12, Figure S3) and overlap with the Paleocene-Eocene igneous rocks of NE Iran. High uranogenic-Pb isotope ratios of Quchan rocks may show the involvement of an enriched mantle. This enriched mantle could be the result of contamination and/or re-fertilization of a depleted mantle source with marine sediments through the subduction of the Neotethyan oceanic lithosphere beneath Iran, creating a metasomatized lithospheric mantle. This type of enriched lithospheric mantle has also been suggested for the formation of high-K rocks from the Mediterranean region (e.g., Conticelli et al., 2009; Cvetkovic et al., 2013). A metasomatized enriched mantle with radiogenic Pb (Δ8/4 > 45) is also suggested as the source of postcollisional (Pleistocene-Holocene) volcanism in Central Anatolia (Reid et al., 2017). Sample AD12-1 has higher thorogenic and uranogneic Pb isotope ratios whereas sample AG12-4 has lower values of thorogenic and uranogneic Pb. Both samples are non-adakitic dacites with low Sr/Y and

Lu	Hf	Nd	Sm	Rb	Sr	206/204i	207/204i	208/204i	^{87}Rb/^{86}Sr	^{87}Sr/^{86}Sri	^{147}Sm/^{144}Nd	^{143}Nd/^{144}Nd	εNd (t = 24)	^{176}Lu/^{177}Hf	^{176}Hf/^{177}Hfi	εHf (t = 24)	Δ 7/4	Δ 8/4	Δ Hf
0.36	3.81	22.86	4.77	18.23	658.78	18.417	15.558	38.493	0.080	0.704336	0.126	0.512840	4.58	0.013522	0.283032	9.28	7.07	60.02	0.07
0.35	3.85	23.02	4.81	18.96	800.93	18.422	15.558	38.500	0.068	0.705004	0.126	0.512834	4.44	0.013132	0.283038	9.50	6.98	60.08	0.48
0.34	4.38	28.32	5.02	39.96	613.61	18.587	15.592	38.821	0.188	0.704792	0.107	0.512884	5.44	0.011024	0.282923	5.43	8.59	72.19	−4.98
0.25	3.13	16.63	3.20	24.19	576.49	18.457	15.576	38.591	0.121	0.703934	0.116	0.512986	7.42	0.011658	0.283037	9.47	8.38	64.93	−3.72
0.26	3.15	13.87	2.91	22.31	407.42	18.481	15.604	38.621									11.02	65.09	
0.25	3.11	16.44	3.14	24.21	574.27	18.463	15.574	38.607									8.20	65.81	
0.18	2.66	7.71	1.57	17.01	224.65	18.266	15.532	38.271	0.219	0.704180	0.122	0.512874	5.24	0.009624	0.283117	12.28	6.13	56.02	2.15
0.21	2.60	10.10	2.19	3.40	475.45	18.362	15.558	38.441	0.021	0.705068	0.131	0.512854	4.85				7.68	61.45	
0.12	2.81	11.79	2.11	26.86	493.92	18.534	15.604	38.709	0.157	0.704388	0.108	0.512622	0.32	0.006358	0.282908	4.90	10.37	67.45	1.65
0.09	2.16	7.82	1.49	15.55	492.92	18.492	15.591	38.652	0.091	0.703957	0.115	0.512762	3.04	0.005927	0.283065	10.44	9.55	66.81	3.38
0.14	3.29	14.89	2.50	20.74	456.92	18.552	15.613	38.773	0.131	0.704428	0.101	0.512803	3.85	0.006073	0.282888	4.18	11.09	71.63	−4.02
0.12	2.57	8.97	1.72	14.52	443.76	18.493	15.594	38.646	0.095	0.704230	0.116	0.512823	4.24	0.006563	0.282994	7.94	9.82	66.04	−0.80
0.08	2.30	7.39	1.44	7.80	410.31	18.495	15.592	38.653	0.055	0.704060	0.118	0.512928	6.28	0.005266	0.283068	10.58	9.57	66.56	−1.02
0.13	2.98	11.50	2.12	16.61	450.22	18.520	15.608	38.700									10.91	68.20	
0.10	2.58	6.73	1.40	9.59	359.50	18.508	15.593	38.667	0.077	0.704108	0.125	0.512934	6.41	0.005617	0.283058	10.20	9.59	66.42	−1.58
0.25	4.73	22.89	3.81	2.13	362.51	18.708	15.640	38.997	0.017	0.705464	0.100	0.512614	0.15	0.007493	0.282866	3.43	12.16	75.20	0.42
0.11	2.80	11.39	2.02	16.89	455.56	18.514	15.602	38.702	0.107	0.704277	0.107	0.512816	4.10	0.005794	0.282941	6.08	10.42	69.17	−2.46
0.09	2.87	10.10	1.76	20.60	405.53	18.503	15.590	38.655	0.147	0.704137	0.105	0.512772	3.24	0.004650	0.283043	9.68	9.33	65.81	2.35
0.09	2.45	9.93	1.78	18.53	364.77	18.516	15.594	38.675	0.147	0.704123	0.108	0.512950	6.71	0.005025	0.283051	9.96	9.59	66.20	−2.23
0.09	2.47	8.92	1.68	13.61	373.15	18.512	15.593	38.670	0.105	0.704302	0.113	0.512972	7.14	0.005013	0.283048	9.84	9.49	66.19	−2.95
0.22	2.85	10.48	2.27	10.75	338.05	18.492	15.601	38.636	0.092	0.704740	0.130	0.513035	8.36	0.011060	0.283094	11.47	10.54	65.16	−3.04

La$_{(n)}$/Yb$_{(n)}$. The radiogenic Pb isotopes of some felsic rocks can also show assimilation of Cadomian continental crust during magma ascent.

Zircons from dacites and rhyolites display εHf(t) from +13.7 to −6.5. The highly variable εHf(t) values for these rocks again could attest to contamination with the Cadomian continental crust.

5. Discussion

The composition of magmas erupted in subduction-related continental arcs can reflect an interplay between the mantle source composition and processes occurring during melt generation and ascent to the arc surface. These processes may take place in the mantle (e.g., mixing of sediment/slab melts and fluids into a depleted mantle) or crust (e.g., MASH or assimilation-fractional crystallization which can incorporate lower- or upper continental crust during magma ascent and storage). Heterogeneities within the mantle and/or lower-crustal reservoirs can result in geochemical variations in magma composition (e.g., Rapp et al., 2008; Stracke, 2012; Willbold & Stracke, 2006, 2010). In addition to source heterogeneities, continental middle to the upper crust, especially in the case of collisional systems, can contribute to final magma compositions. Below, we first explore the characteristics of the mantle source in the Quchan area using basaltic rocks, and then we use the basaltic rocks to understand the origin and evolution of Quchan felsic and/or adakitic rocks. To unravel the genesis of the felsic/adakitic rocks, we first focus on the geochemical signatures of these rocks as well as the composition of their amphiboles and then use the FC, AFC, and REFC models to show the evolution of the major- and trace-elements from basaltic rocks into intermediate and then into felsic/adakitic rocks. Finally, we will use the Sr, Nd, and Pb isotopes to see if the isotopic signatures of the Quchan rocks are solely controlled by a depleted mantle and its interaction with crustal components via assimilation, or whether an enriched mantle source is required.
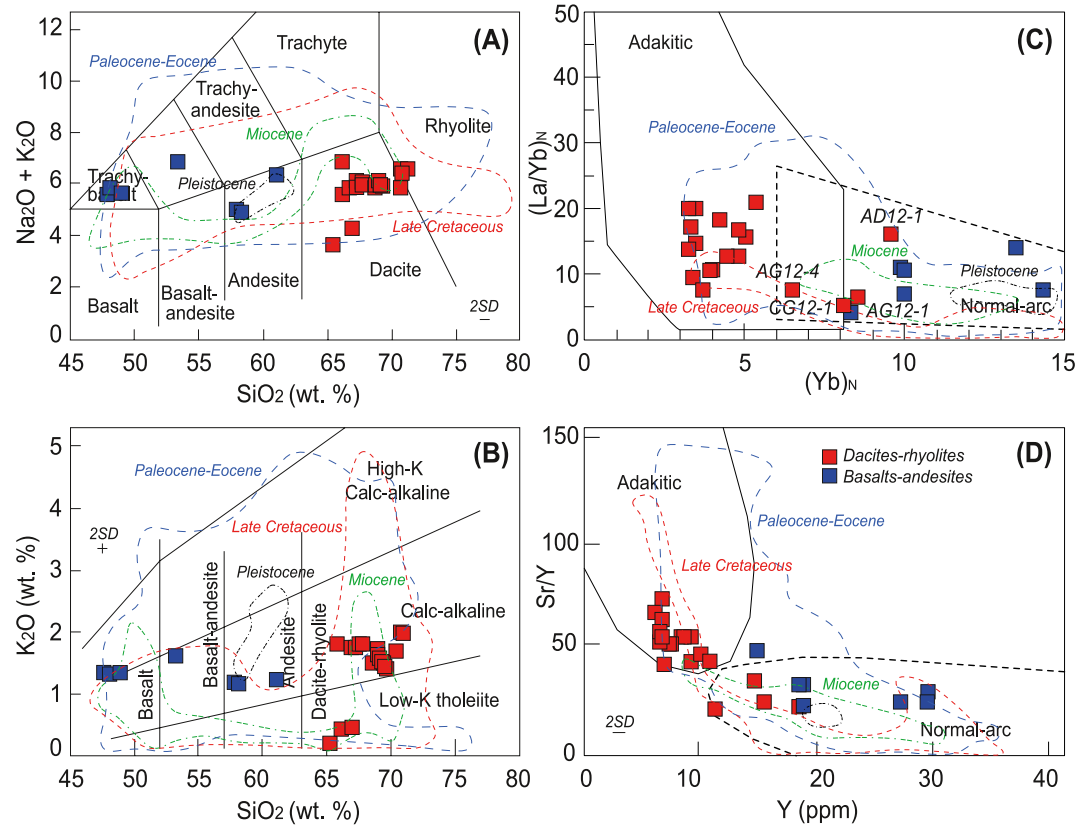
Figure 6. $Na_2O + K_2O$ and K_2O versus SiO_2 discrimination diagrams (a and b) for the classification of Quchan volcanic rocks (modified after Lebas et al. [1986]). $La_{(n)}/Yb_{(n)}$ versus $Yb_{(n)}$ (c) and Sr/Y versus Y diagrams for discriminating Quchan volcanic rocks (compositional domains for adakite and normal arc rocks are according to Castillo [2012] and Defant and Drummond [1990]). Geochemical data for Late Cretaceous to Pleistocene magmatic rocks are from Moghadam, Li, Li, et al. (2020).

5.1. Source Characteristics

Postcollisional Oligocene magmas in NE Iran could come from the melting of a metasomatized mantle, with traces of the previous subduction, from Late Cretaceous to Oligocene, before the continental collision occurred. Therefore, several complex processes, including the interaction of subducting sediments/sediment melts with a depleted mantle, could enrich the mantle wedge or the sub-continental lithospheric mantle.

The Quchan volcanic rocks isotopically plot in a trend between the depleted mantle and the Cadomian continental crust (Figure 8) and their isotopic and trace-element signatures rule out a depleted MORB-type mantle as a unique source for the genesis of these rocks. The presence of spinels with high TiO_2 and Al_2O_3 in near primitive basaltic rocks (Figure 3e) could also eliminate a depleted mantle as the source of Quchan mafic rocks. Although crustal processes such as AFC could lead to the generation of felsic rocks, these processes are inadequate to cause the range of trace elements and isotopic compositions observed in basalts (see Section 5.3.4). Instead, we suggest some aspects of the wide range in trace elements and Sr, Nd, Hf and Pb isotopic composition of the Quchan volcanic rocks can be inherited from heterogeneity within the mantle. Both source heterogeneities and contamination with the Cadomian continental crust of Iran could generate such trace element and isotopic variations.

Most volcanic rocks from Quchan are fractionated silicic rocks and the primary mantle-derived basaltic rocks needed to unravel the mantle composition are rare. However, some basalt samples with high Mg# (57%–59%) and with $\varepsilon Nd(t) = 5.4$–4.4; $\varepsilon Hf(t) = 9.5$–5.4 have high Nb/U (~9–26) and low Zr/Nb (~9–15), which suggests that these samples could allow the extrapolation of the composition of the primary man-
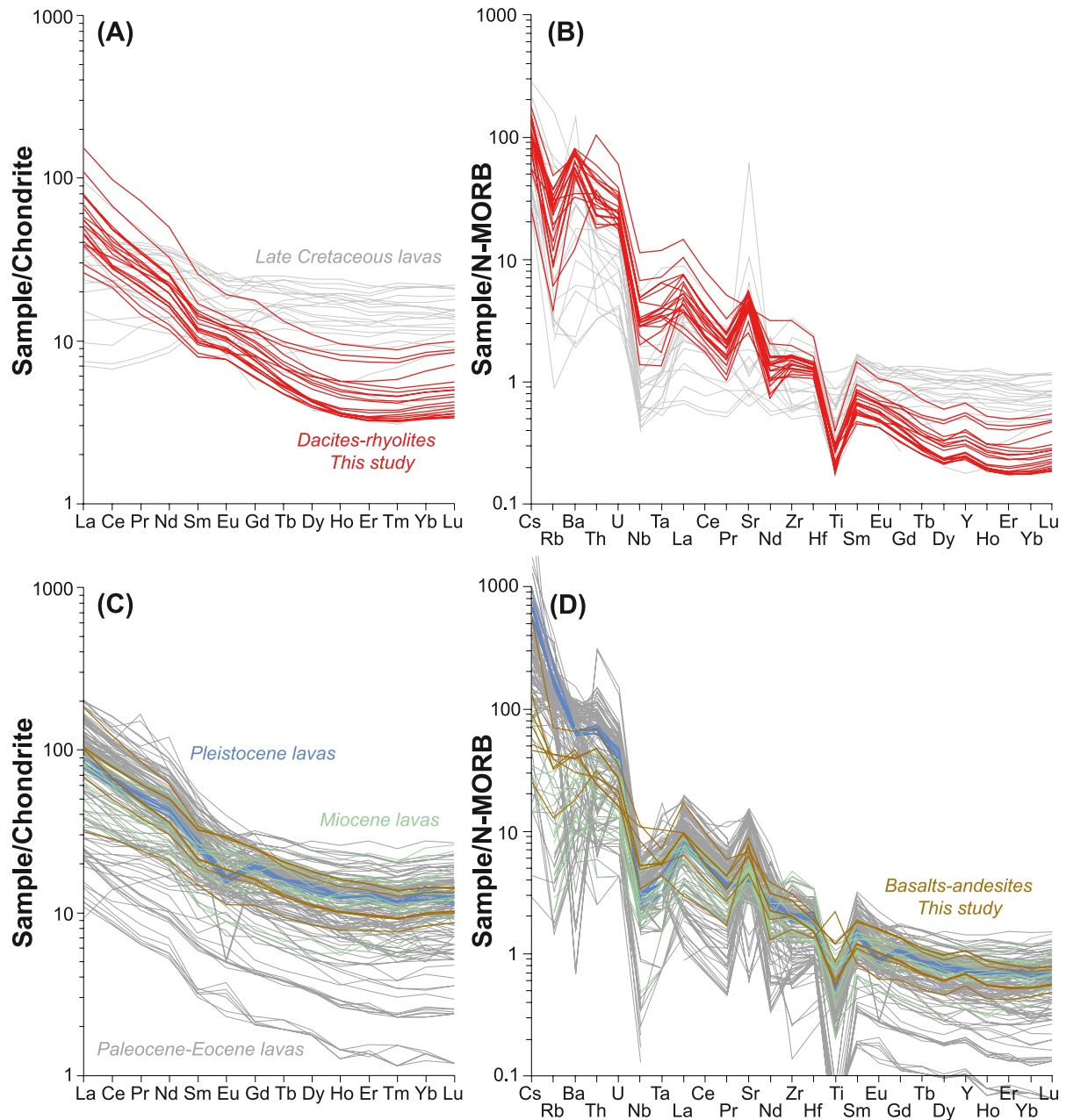
Figure 7. Chondrite- and N-MORB-normalized REE and trace-element patterns of NE Iran BA igneous rocks from different magmatic episodes. Normalization data are from Sun and McDonough (1989). Geochemical data for Late Cretaceous to Pleistocene magmatic rocks are from Moghadam, Li, Li, et al. (2020). The Palaeocene-Eocene geochemical data are heterogenous, and describing these heterogeneities is beyond the scope of this paper, but these data support the case for complex magmatic plumbing systems that evolve in continental arcs.

tle melts. As such, we have applied a simple mixing model and subsequent partial melting considering a Depleted Mantle (DM) that was metasomatized by bulk mixing with altered oceanic crust and terrigenous sediments (Figure 9). Our model is not a unique solution to explain the genesis of all basaltic rocks, but this model is geologically reasonable for a region that has been experienced long-time subduction from Late Cretaceous to Late Oligocene. For modeling, we have used three basaltic samples with MgO ∼5–7 wt%, that is, samples MB12-1, MB12-2, and DA12-1. In order to examine the source mantle composition and processes, we used the PRIMACALC2 spreadsheet, which allows an estimation of a primary melt in equilibrium with the upper mantle (Kimura & Ariskin, 2014).
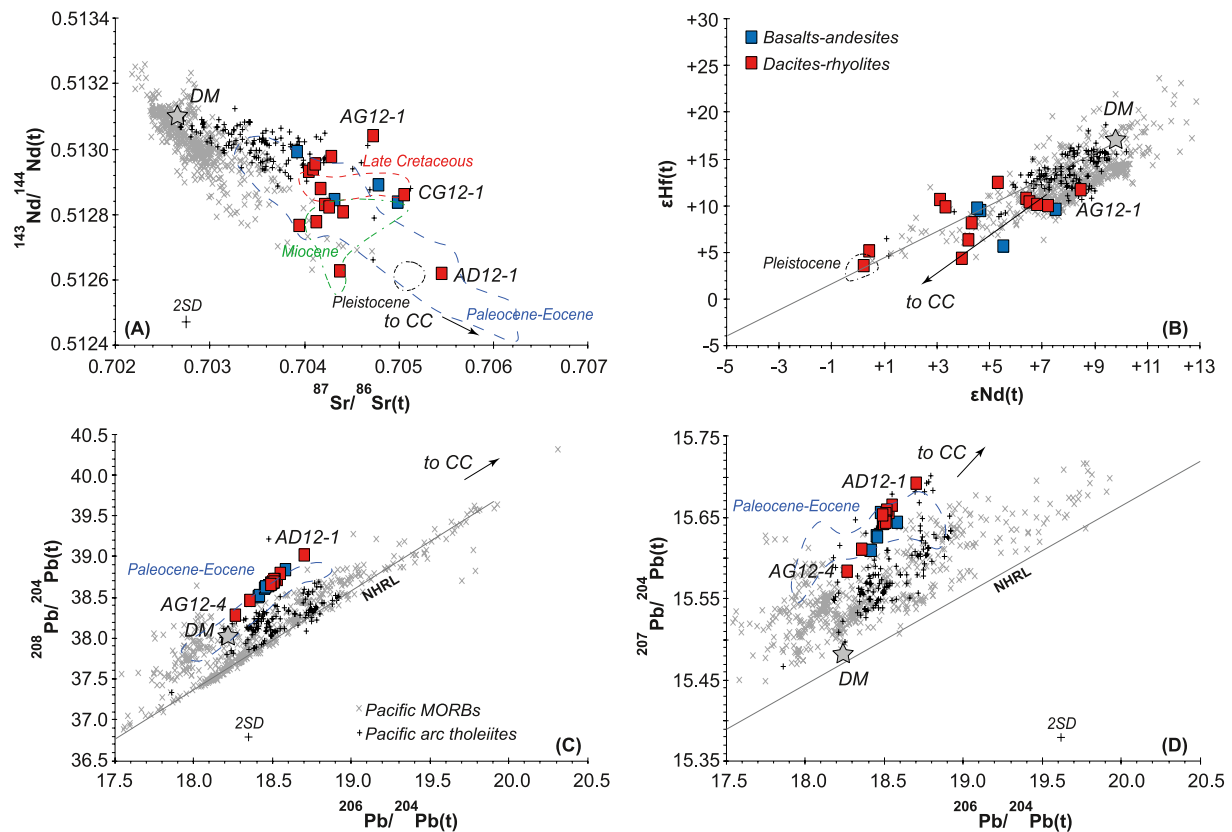
Figure 8. (a) $^{143}Nd/^{144}Nd$ versus $^{87}Sr/^{86}Sr$ plot for Quchan volcanic rocks compared with the depleted mantle (DM) (Zindler & Hart, 1986). (b) $\varepsilon Hf(t)$ versus $\varepsilon Nd(t)$ for Quchan volcanic rocks. Mantle array after (Vervoort & Blichert-Toft, 1999) is defined as $\varepsilon Hf = 1.4 \times \varepsilon Nd + 2.8$. (c) $^{208}Pb/^{204}Pb$ versus $^{206}Pb/^{204}Pb$ and (d) $^{207}Pb/^{204}Pb$ versus $^{206}Pb/^{204}Pb$ diagrams for Quchan lavas. The Northern Hemisphere Reference Line (NHRL) is from Hart (1984). Data on Pacific MORBs and Pacific arc tholeiites are from EarthChem (https://www.earthchem.org). The composition of Cadomian continental crust (CC) comes from Moghadam, Li, Griffin, et al. (2020). Geochemical data for Late Cretaceous to Pleistocene magmatic rocks are from Moghadam, Li, Li, et al. (2020). All data including those for MORBs and arc tholeiites have been corrected for 24 Ma radiogenic growth.

Data for the altered oceanic crust and terrigenous sediments, DM, mantle modal mineralogy and bulk Kd, come from (Iveson et al., 2018; Jacques et al., 2014; Kimura et al., 2009; Nandedkar et al., 2016; Saginor et al., 2013; Workman & Hart, 2005; Zhang et al., 2019). The bulk partition coefficients assume mantle mineralogy of 45% olivine, 19% clinopyroxene, 23% orthopyroxene, 10% amphibole and 3% garnet. Subsequently, we assumed aggregated fractional melting of the mixed source (DM + altered oceanic crust and trench sediments) with variable degrees of melting. All modeling parameters are presented in Table S6. Since both the degree of melting and ratio of DM to altered oceanic crust and trench sediments are unknown, we applied an iterative method whereby both unknowns have been changed until the composition of the modeled melt resembled the selected Quchan basalts. Our model (modeled melt (1) in Figure 9) indicates that a 90:6:4 mixture of DM and terrigenous trench sediment and altered oceanic crust, with 5% aggregated fractional melting, will closely match the trace-element abundances of our target basalts (Figure 9). Higher proportions of altered oceanic crust and trench sediments or different melting percentages give patterns that do not match our samples. However, the modeled melt has slightly lower Sr (±Nb) than the target samples, but also anomalies in Pb, U, and Rb. The modeled melt has a positive anomaly in Pb compared to our basalts. The Pb content in the subduction-related magmas is very dependent on the amount and the composition of subducting sediments. The target basalts instead have a peak in Sr and sample MB12-2 does not show depletion in Nb-Ta, which is different from the modeled Nb-Ta depleted melt. We thus emphasize that two basaltic samples with Nb-Ta depletion could come from melting of a metasomatized mantle (i.e., a mixture of DM and terrigenous trench sediment + altered oceanic crust), similar to the modeled melt. Sample MB12-2 without Nb-Ta depletion is alike to the enriched MORBs and could come from partial melting of an enriched mantle. Similar mantle sources have been considered for the formation of postcollisional magmas
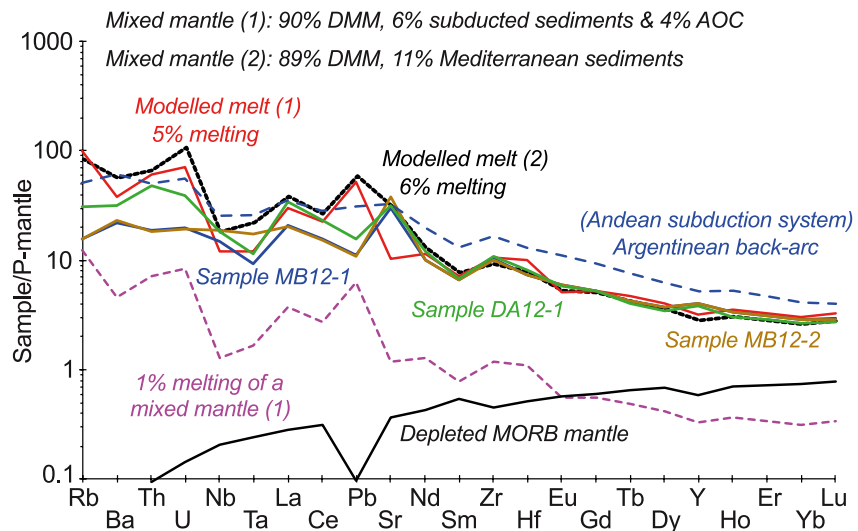
Figure 9. Sample/primary-mantle normalized diagram for the primary Quchan melts (basaltic samples including MB12-1, MB12-2 and AD12-1) in equilibrium with mantle– calculated using PRIMACALC2 (Kimura & Ariskin, 2014). Modeled melts (melts [1 and 2]) assumes 5% and 6% aggregated fractional melting of the mixed (90% DM + 6% subducted sediments + 4% altered oceanic crust, AOC and/or 89% DM + 11% Eastern Mediterranean Sea sediments) mantle sources. For compression, we also show the modeled melt after 1% aggregated fractional melting of the mixed mantle (1). Data and parameters for these calculations are provided in Table S6. Data on Argentinian back-arc average basalt is from Jacques et al. (2013, 2014).

in Central Anatolia (Reid et al., 2017) and Quaternary basaltic lavas from the Argentinean back-arc region of the southern Andean subduction system (e.g., Jacques et al., 2013, 2014). This basalt sample MB12-2 has radiogenic Pb isotopic composition– with $\Delta 7/4 = 6.98$ and $\Delta 8/4 = 60.08$ (Figure S3)—consistent with formation in a subduction-related setting.

It is possible that the altered oceanic crust and trench sediments and/or the "ambient mantle" composition we selected for our model are different from those that prevailed in the magmatic source of Quchan rocks. Unlike recent subduction systems, it is hard to evaluate the compositions of the source mantle and subducted materials for an ancient subduction system like the Cenozoic arcs of Iran. For further testing of our model, we have used the average composition of Eastern Mediterranean Sea sediments (Klaver et al., 2015), to mix with a depleted mantle. Our new model (modeled melt (2)) support that an 89:11 mixture of DM and Eastern Mediterranean Sea sediments– with 6% aggregated fractional melting– again closely match with the trace-element composition of our target basalts, excluding positive anomalies in Pb, Rb, Ba, Th, and U and less negative anomalies in Nb-Ta than our target samples. The positive anomalies in the above-mentioned elements could be related to the nature of the presumed subducting sediments (the Eastern Mediterranean Sea sediments) which have marl and mudstone composition.

5.2. Petrogenesis of Adakites

5.2.1. Amphibole as a Precursor

Experimental studies emphasize the role of amphibole fractionation during the crystallization and geochemical evolution of subduction-related, H_2O-rich magmas (e.g., Carmichael, 2002; Grove et al., 2002, 2003, 2006, 2012). These studies attest to the importance of amphibole crystallization and its effect on the HREE to MREE patterns and probably it is a key for producing adakitic signatures in some magmatic rocks from continental arcs (e.g., Davidson et al., 2007; Hidalgo et al., 2011). Extreme amphibole fractionation could be considered as a mechanism for the formation of spoon-like HREE to MREE patterns in Quchan felsic samples and also can reconcile some elemental ratios such as La/Nb, Nb/U, $Dy_{(n)}/Yb_{(n)}$, $La_{(n)}/Sm_{(n)}$, and Dy/Dy* which are keys for recognizing the adakitic signature (see next section). We believe the composition of amphibole phenocrysts from Quchan felsic rocks can give a representative indicator of the magmatic processes

during the formation of adakitic-like geochemical signatures. For this purpose, the mineral formulae for amphiboles were re-calculated following the spreadsheet supplied by (Ridolfi et al., 2010), and re-interpreted by (Hidalgo et al., 2011). In this spreadsheet, the Fe^{+3}/Fe^{+2} ratio is re-calculated by charge balance after correcting the tetrahedral (Si, Al, and Ti) plus octahedral (Al, Ti, Cr, Fe, Mn, and Mg) cations to 13 (Leake, Woolley, Birch, et al., 1997). This calculation shows that amphiboles from Quchan felsic rocks mostly have Tschermakitic pargasite composition, with ~0.02–0.4 apfu Na cation (atoms per formula unit = apfu) in site A, but with 1.5–1.8 Ca and 0.2–0.5 Na cations in site B and 0.08–0.2 Ti in Site C, and were in equilibrium with calc-alkaline melts. Site A also contains a noticeable amount of K (0.04–0.2).

In a plot of $Al^{(T)}$ (total Al = $^{[6]}Al$ + $^{[4]}Al$) versus $^{[4]}Al$, considering the Al# content ($=^{[6]}Al/^{[6]}Al$ + $^{[4]}Al$) (Figure S4), all amphiboles from Quchan felsic rocks follow a common compositional trend. The $Al^{(T)}$ of these amphiboles ranges between 1.6 to 2.2, with Al# between 0.12 and 0.28. Our data show that these amphiboles have higher Al# content than amphiboles from shallow volcanic rocks (with Al# = 0) and even some analyzed spots from amphiboles (toward the cores of grains) have an Al# content comparable to high-P crustal and/or mantle-derived (experimental) amphiboles (with Al# = 0.21) (Hidalgo et al., 2011; Ridolfi et al., 2010). Thermobarometric calculations record pressures of 4–6 Kbar and temperatures ranging from 834 to 900°C. Oxygen fugacity can be calculated from the amphibole composition (Ridolfi et al., 2010) using the amphibole magnesium index (Mg*): $\Delta NNO = 1.644\ Mg* - 4.01$ (where $Mg* = Mg + Si/47 - ^{[6]}Al/9 - 1.3^{[6]}Ti + Fe^{+3}/3.7 + Fe^{+2}/5.2 - ^BCa/20 - ^ANa/2.8 + ^A[t]/9.5$). The calculated values range from log-fO_2 −13.7 to −10.5, and ΔNNO = −0.6 to +1.8. For comparison, the ΔNNO for calc-alkaline magmas is suggested to be in the range of −1 to +3 (Carmichael, 1991; Hidalgo et al., 2011; Ridolfi et al., 2010).

The relationships between temperature (834–900°C) and H_2O_{melt} (7–9.5; inferred from amphibole composition) indicates maximum stability for the formation and fractionation of Quchan amphiboles in the middle-lower crust (e.g., Müntener et al., 2001). Finally, these P, P_{H2O}, and T estimates on amphiboles from different Quchan rocks could suggest that differentiation of the Quchan melts occurred at *ca* 14–20 km depth (assuming an average crust density of 2,700 kg/m³ [e.g., Lucci et al., 2020; Rossetti et al., 2017] in the middle crust), although amphiboles with high Al# (Al# >0.2) may suggest greater depths. Therefore, our data are consistent with the observation that parts of amphiboles (or amphibole cores) crystallized earlier, in the deeper crust– and probably in deep crustal hot zones. Crystallization of H_2O-rich magmas similar to the parental melts of Quchan lavas (with H_2O_{melt} = 7 to 9.5) in the middle to lower crust (at >~7 km) will lead to amphibole appearing as the first mineral on the liquidus of basaltic to andesitic melts (Carmichael, 2002; Moore & Carmichael, 1998; Rooney et al., 2011). However, amphibole fractionation in the lower-middle crust is supposed to follow the earlier crystallization of olivine and pyroxene in the upper mantle-lower crust (e.g., Hidalgo et al., 2011; Rooney et al., 2011), which is also consistent with our fractional-crystallization modeling (see below).

5.2.2. Geochemical Evaluation of Quchan Adakites

Several models have been suggested for the origin of adakites including melting of the eclogitic parts of subducting oceanic crust and/or eclogitic segments of the lower continental crust (e.g., Castillo, 2006; Chiaradia et al., 2009; Kay & Kay, 2002; Kolb et al., 2013; Rapp & Watson, 1995). Garnet and/or amphibole fractionation along with AFC processes at the base of the thickened continental crust has been also considered as a candidate for the genesis of adakites (e.g., Chiaradia, 2009; Hidalgo & Rooney, 2014; Hidalgo et al., 2011). AFC and/or MASH processes have been suggested as the main trigger for the formation of both silicic and adakitic magmas in the lower continental crust, in deep crustal hot zones, where mantle-derived magmas are being modified (Annen et al., 2006a).

Our new geochemical data show that the Late Oligocene Quchan felsic volcanic rocks show both normal arc (±mafic volcanic rocks) and adakitic compositions. Fractionated Quchan felsic rocks show shallower slopes in plots of Th/Yb, Ba/Yb, and La/Yb versus Nb/Yb (Figures 10a, 10b, and 10e), which can reflect enrichment in Nb and depletion in Yb and Y because of crystal fractionation. The Quchan adakitic rocks have higher Nb/Yb and Th/Yb than basalts and andesites, but some non-adakitic samples (AD12-1, AG12-1, AG12-4, and CG12-1) have similar ratios to basalts and andesites. The Quchan Oligocene adakites have Nb/Yb, La/Yb, Th/Yb, and Ba/Yb similar to highly fractionated Eocene adakitic-like dacitic-rhyolitic domes (barren adakites) from NW Sabzevar and are geochemically distinct from Eocene, fertile (Cu-Au-
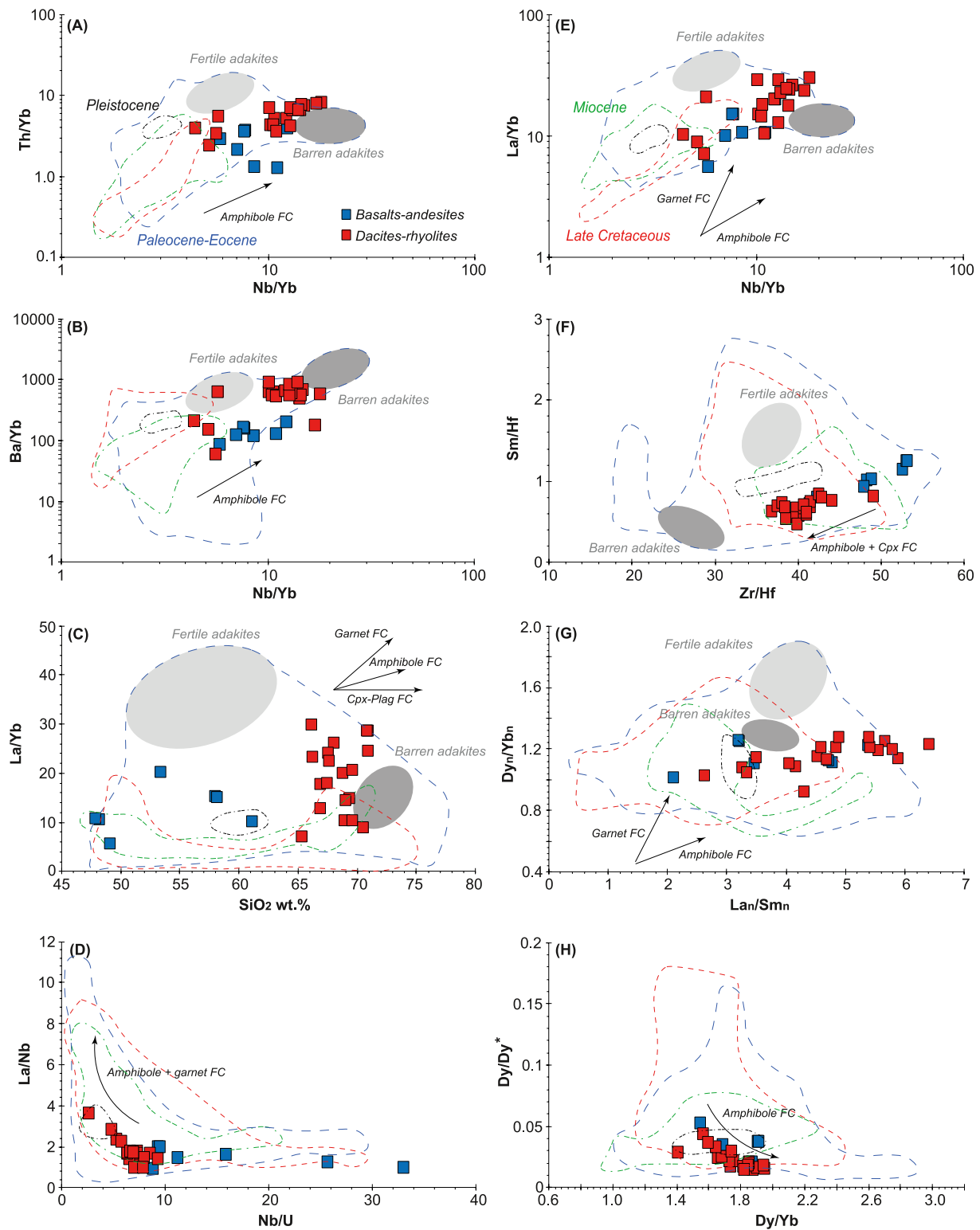
Figure 10. Trace-element ratios including (a) Th/Yb versus Nb/Yb, (b) Ba/Yb versus Nb/Yb, (c) La/Yb versus SiO$_2$, (d) La/Nb versus Nb/U, (e) La/Yb versus Nb/Yb, (f) Sm/Hf versus Zr/Hf, (g) Dy$_{(n)}$/Yb$_{(n)}$ versus La$_{(n)}$/Sm$_{(n)}$, and (h) Dy/Dy* versus Dy/Yb for Quchan volcanic rocks. Most plots show good correlation and some attest to amphibole fractionation. Geochemical data for Late Cretaceous to Pleistocene magmatic rocks are from Moghadam, Li, Li, et al. (2020). For clarity, the domains of Eocene highly fractionated barren silicic rocks with adakitic signatures and fertile (Cu-Au-bearing) adakitic andesites, monzonites and monzo-diorites are shown.

bearing) adakites (andesites, monzonites and monzo-diorites) from S-SW Neyshabour (Moghadam, Li, Li, et al., 2020) (Figure 1b). Quchan felsic rocks (both adakitic and non-adakitic) have negative Ti anomalies but positive anomalies in Sr and Zr-Hf (Figure 7), which probably reflects the assimilation of crustal rocks and amphibole-dominated fractional crystallization.

To test the role of amphibole versus garnet fractionation (and/or garnet as residue) in the formation of the Quchan Oligocene adakites we used a series of plots, for example, La/Yb versus SiO_2 (Figure 10c), La/Nb versus Nb/U (Figure 10d), $Dy_{(n)}/Yb_{(n)}$ versus $La_{(n)}/Sm_{(n)}$ (Figure 10g) and Dy/Dy* versus Dy/Yb (Figure 10h). Amphiboles should have high Nb/U ratios and therefore a decreasing Nb/U along with increasing La/Nb can be considered as an indication of amphibole fractionation. Also, trends observed in Dy/Dy* versus Dy/Yb and $Dy_{(n)}/Yb_{(n)}$ versus $La_{(n)}/Sm_{(n)}$ can be considered as reflecting amphibole fractionation (Davidson et al., 2013). Garnet fractionation would increase La/Yb and $Dy_{(n)}/Yb_{(n)}$ in plots of $Dy_{(n)}/Yb_{(n)}$ versus $La_{(n)}/Sm_{(n)}$ and La/Yb versus SiO_2, which is not the case for Quchan adakites but instead can be seen in fertile adakites from S-SW Neyshabour. There is also a fractionation trend extending from mafic rocks toward dacites-rhyolites in plots of Zr/Hf versus Sm/Hf (Figure 10f), which can show fractionation of clinopyroxene and amphibole. Since amphibole and pyroxene have higher Kd for Hf than for Zr, contributions of trace minerals such as zircon, allanite and xenotime with Kd(Hf)/Kd(Zr) < 1 (Bea et al., 2006) are necessary to explain the fractionation of the Zr/Hf ratio.

There are few geochemical-isotopic data for the Quchan adakites, but available data suggest they were produced by partial melting of the lower continental crust of NE Iran, which has been thickened enough (40–50 km) to generate such melts and/or facilitate high-pressure differentiation of basaltic melts in the deep crust (e.g., Shabanian et al., 2012). However, high-pressure fractionation trends involving garnet cannot be reconciled with our geochemical data, especially the N-MORB-normalized spoon-shaped MREE-HREE patterns for dacites and rhyolites (Figure 7). Instead, we propose that the elemental ratios discussed above suggest that the adakitic signatures of the felsic adakitic rocks (except non-adakitic samples AD12-1, AG12-1, AG12-4, and CG12-1) could have originated from crustal assimilation and extreme fractionation of amphibole ± clinopyroxene ± plagioclase and accessory minerals from a mafic melt similar to the Quchan basaltic melts and/or modeled melt obtained from Section 5.1. In addition, the elemental patterns such as La/Yb versus SiO_2 and/or $Dy_{(n)}/Yb_{(n)}$ versus $La_{(n)}/Sm_{(n)}$ could reflect variable fractionating assemblages, changes in pressure of fractionation and/or the input of new pulses of magma into a pre-existing chamber.

5.3. FC-AFC-REFC Processes and Silicic Magmatism

Our elemental ratios and isotopic data as well as results obtained for amphibole chemistry indicate that crystal fractionation (amphibole dominant) and assimilation of continental crust (AFC) by the Quchan basaltic melts could play an important role in the genesis of silicic magmas (both adakites and non-adakitic rocks) in Quchan. Field, petrography, and isotopic data show evidence for assimilation of crustal host rocks including Cadomian biotite-rich paragneisses. The evidence includes xenoliths in felsic rocks, rounded quartz grains in dacites and rhyolites and variable bulk-rock Sr-isotope compositions as well as zircon εHf(t) values. Major- and trace-element data could also attest to assimilation, which we discuss below. We suggest that the Oligocene Quchan collisional volcanic rocks might represent melts that were extracted from a metasomatized mantle reservoir (see Section 5.1) and evolved via fractional crystallization and assimilation-fractional crystallization in a magmatic plumbing system developed in the Cadomian crust of NE Iran. In order to assess this hypothesis, we tested models invoking Rayleigh FC (e.g., Lucci et al., 2016, 2020; Moghadam et al., 2016; Wanless et al., 2010; White et al., 2009), coupled with AFC (e.g., DePaolo, 1981; Moghadam, Li, Griffin, et al., 2020) and REFC in mafic magmatic reservoirs (Lee et al., 2014). The complete workflow of the FC-AFC-REFC models including, (a) the possible magmatic parental melts and assimilated crustal rocks, (b) calculation of trace-element partition coefficients, and (c) presentation of the FC-AFC-REFC equations is explained in Supporting Information S1. All the parameters and results obtained from FC-AFC-REFC modeling are presented in Tables 4 and 5 and Tables S4 and S5.

5.3.1. Fractional Crystallization (FC)

Major elements mass-balance modeling has been used to simulate the role of FC and AFC processes in the formation of Quchan intermediate and felsic (both adakites and non-adakitic-) rocks from basaltic pre-

Table 4
Bulk Compositions Used in the FC-AFC Models

Rock	Magmatic parental melts		Cadomian assimilant
	MB-av[a]	SB-av[b]	BJ-09-6[c]
SiO_2 (wt%)	48.06	58.10	67.00
TiO_2	1.54	0.70	0.48
Al_2O_3	17.18	17.52	16.69
FeO^{Tot}	8.00	5.29	4.36
MnO	0.14	0.09	0.07
MgO	6.94	4.02	0.95
CaO	8.34	6.91	4.22
Na_2O	4.33	3.69	3.60
K_2O	1.33	1.16	1.41
P_2O_5	0.45	0.25	0.16
Total	96.31	97.73	98.93
Trace elements for FC-AFC models			
Sr (ppm)	729.85	575.38	280.00
y	29.63	19.06	13.00
Dy	4.43	2.73	2.42
Yb	2.32	1.60	1.25
Major elements normalized to 100% on a volatile- and P_2O_5-free basis			
SiO_2 (wt%)	50.14	59.60	67.83
TiO_2	1.60	0.72	0.48
Al_2O_3	17.92	17.97	16.90
FeO^{Tot}	8.34	5.43	4.41
MnO	0.15	0.09	0.07
MgO	7.24	4.12	0.96
CaO	8.70	7.09	4.27
Na_2O	4.51	3.79	3.64
K_2O	1.39	1.19	1.43

[a]Mean composition calculated from MB12-1 and MB12-2 samples. [b]Mean composition calculated from SB12-1 and SB12-2 samples. [c]Cadomian assimilant composition from Moghadam et al. (2020).

cursors. The quality of the calculated models is evaluated through the minimization of the sum of the squared residual (Σr^2) of the *Parental Melt* versus *Daughter Liquid + Fractionating Mineral Assemblage* relationship. Major element mass-balance models are considered acceptable when $\Sigma r^2 < 1.0$. The calculated models show that basaltic samples such as CG12-4 (SiO_2 49.1 wt%) and DA12-1 (SiO_2 53.4 wt%) reflect *ca* 30%–45% FC of an average basaltic parental melt (MB-av; average composition of samples MB12-1 and MB12-2 with MgO values of 7.1 and 6.8 wt%, respectively), with crystallizing assemblages of hornblende + plagioclase together with Cr-spinel and olivine ($Hbl_{14–59} + Pl_{18–67} \pm Spl_{0–28} \pm Ol_{0–17}$; hereafter percentages are given for the total crystallized assemblage; see Tables 4 and 5). However, the resulted crystallizing assemblage fails (Σr^2 ~3.6–16.2), mainly due to the large r^2 for Na, to directly reproduce the differentiation trend from the basaltic source to the Quchan andesites (see representative models 4, 9, and 10 and replicated models 31–33 using plagioclases with different Na_2O contents, in Table S4), and to some dacites and rhyolites (see representative models 34 to 41, in Table S4).

Considering the generally comparable mineralogical assemblages and textures of andesites and felsic rocks, we also explored a possible direct genetic connection between andesites (SB-av; average composition of SB12-1 and SB12-2) and Quchan dacites and rhyolites ($SiO_2 > 60$ wt%). This exercise led us to test new major-element mass-balance models for an average andesitic source (SB-av). The calculated trends (Table S4) clearly show that all Quchan SiO_2-rich melts could be produced by 45%–55% FC of andesite (SB-av) with a fractionating assemblage of hornblende, plagioclase and ilmenite ($Hbl_{50-53} + Pl_{44-47} + Ilm_{2-3}$) (models 11–26, Table S4). Quartz is considered as a fractionating phase for andesite sample AG12-3 (model 27 in Table S4). No acceptable solution (Σr^2 *ca* 2.2–3.1; models 28, 29, and 30 in Table S4) is found for low-K dacites (samples AD12-1, CG12-1, and SM12-3), where the large r^2 values for Al, Mg, Ca, Na and K suggest that postmagmatic albitization or other alteration has affected these samples. This assumption is also consistent with the high $^{87}Sr/^{86}Sr$ of these rocks.

Harker-like geochemical diagrams for major-element mass-balance models are presented in Figure 11, where three representative FC trends are shown: (a) Bas1 ($Hbl_{59} + Pl_{13} + Spl_{28}$) dominated by hornblende (model 2 in Table S4); (b) Bas2 ($Hbl_{14–18} + Pl_{67} \pm Spl_{0–1} \pm Ol_{14–17}$) dominated by plagioclase (models 5 and 8 in Table S4); and (c) And ($Hbl_{52} + Pl_{46} + Ilm_2$) with comparable roles of hornblende and plagioclase (models 11–26 in Table S4).

5.3.2. Assimilation-Fractional Crystallization (AFC)

The failure of fractionation of basalts to yield andesites, dacites, and rhyolites strongly suggest the possible contribution of crustal materials through AFC; mass-addition, mainly during the genesis of fractionated melts (e.g., McBirney et al., 1987; Moghadam, Li, Griffin, et al., 2020). To test this hypothesis, we applied AFC models based on the interaction between Quchan collisional mafic melts (i.e., basalts and andesites) and the Cadomian felsic crust that outcrops in NE Iran and hosted the Quchan plumbing system. Maximum mass-addition (assimilation) trends calculated through the lever-rule method are reported in Table 5 and Figures 11 and 12. In agreement with the method proposed by Moghadam, Li, Griffin, et al. (2020), if a pure crystal-fractionation (FC) trend corresponds to the null-assimilation value, then the compositional space between the FC- and the maximum mass-addition (assimilation) trends correspond to the possible compositions of residual liquids produced by AFC-processes.

Table 5
Major-Element AFC Model for MB-av and SB-av to the Cadomian Crust

Rock	Magma										Cadomian assimilant
AFC parameters	C_0	C_L									C_A
a[a] Composition	MB-av	0.1	0.2	0.3	0.4	0.5	0.6	0.7	0.8	0.9	BJ-09-6
SiO_2 (wt%)	50.14	51.91	53.68	55.45	57.22	58.99	60.75	62.52	64.29	66.06	67.83
TiO_2	17.92	17.82	17.71	17.61	17.51	17.41	17.31	17.20	17.10	17.00	16.90
Al_2O_3	8.34	7.95	7.56	7.16	6.77	6.38	5.99	5.59	5.20	4.81	4.41
FeO^{Tot}	0.15	0.14	0.13	0.12	0.12	0.11	0.10	0.09	0.08	0.07	0.07
MnO	7.24	6.62	5.99	5.36	4.73	4.10	3.47	2.85	2.22	1.59	0.96
MgO	8.70	8.26	7.82	7.37	6.93	6.49	6.04	5.60	5.16	4.72	4.27
CaO	4.51	4.43	4.34	4.25	4.17	4.08	3.99	3.91	3.82	3.73	3.64
Na_2O	1.39	1.39	1.40	1.40	1.41	1.41	1.41	1.42	1.42	1.42	1.43
K_2O	1.60	1.49	1.38	1.27	1.15	1.04	0.93	0.82	0.71	0.59	0.48
Total	100.00	100.00	100.00	100.00	100.00	100.00	100.00	100.00	100.00	100.00	100.00
Rock	Magma										Cadomian assimilant
AFC parameters	C_0	C_L									C_A
a[a] Composition	SB-av	0.1	0.2	0.3	0.4	0.5	0.6	0.7	0.8	0.9	BJ-09-6
SiO_2 (wt%)	59.60	60.42	61.25	62.07	62.89	63.72	64.54	65.36	66.19	67.01	67.83
TiO_2	17.97	17.86	17.76	17.65	17.54	17.43	17.33	17.22	17.11	17.00	16.90
Al_2O_3	5.43	5.32	5.22	5.12	5.02	4.92	4.82	4.72	4.62	4.52	4.41
FeO^{Tot}	0.09	0.09	0.08	0.08	0.08	0.08	0.08	0.07	0.07	0.07	0.07
MnO	4.12	3.81	3.49	3.18	2.86	2.54	2.23	1.91	1.59	1.28	0.96
MgO	7.09	6.81	6.53	6.25	5.96	5.68	5.40	5.12	4.84	4.55	4.27
CaO	3.79	3.77	3.76	3.74	3.73	3.72	3.70	3.69	3.67	3.66	3.64
Na_2O	1.19	1.22	1.24	1.26	1.29	1.31	1.33	1.36	1.38	1.40	1.43
K_2O	0.72	0.70	0.67	0.65	0.63	0.60	0.58	0.55	0.53	0.51	0.48
Total	100.00	100.00	100.00	100.00	100.00	100.00	100.00	100.00	100.00	100.00	100.00

Note. C_0 stands for the initial concentration of an element in the parental liquid, C_A is the concentration of element in assimilant, C_L is the concentration of element in the generated liquid.
[a]Proportion of assimilated rock.

Results obtained from AFC modeling suggest that the Quchan andesites could represent basaltic melts that have undergone *ca* 50% coupled assimilation and fractional crystallization processes. On the other hand, the direct effect of assimilation of the Cadomian felsic rocks appears to be limited in the genesis of dacites and rhyolites from the andesitic melts.

Based on these results, we further investigated the evolution of Quchan melts through FC-AFC modeling applied to representative trace- (Sr and Y) and rare-earth (Dy and Yb) elements (results are in Table S5 for FC and AFC models). Solutions for these FC-AFC models are consistent with those for major-element models, supporting the scenario of Quchan magmatism controlled by FC coupled with assimilation processes. Rayleigh FC models calculated for the Bas1 assemblage generally fail to produce andesites and felsic melts (Figure 11), whereas a combination of fractional crystallization (FC ~ 40–60%) and assimilation up to *ca* 30% (proportion of assimilant to fractionates *r* = 0.3) of Cadomian felsic crust seems capable of generating andesites from Quchan basalts. Dacites and rhyolites (including adakites) are then the residual liquids after 50%–70% FC of an andesitic parental melt (Figure 12). Higher rates of assimilation (>30%) of Cadomian felsic crustal rocks are still recognizable. However, at this stage, we cannot rule out the inheritance of
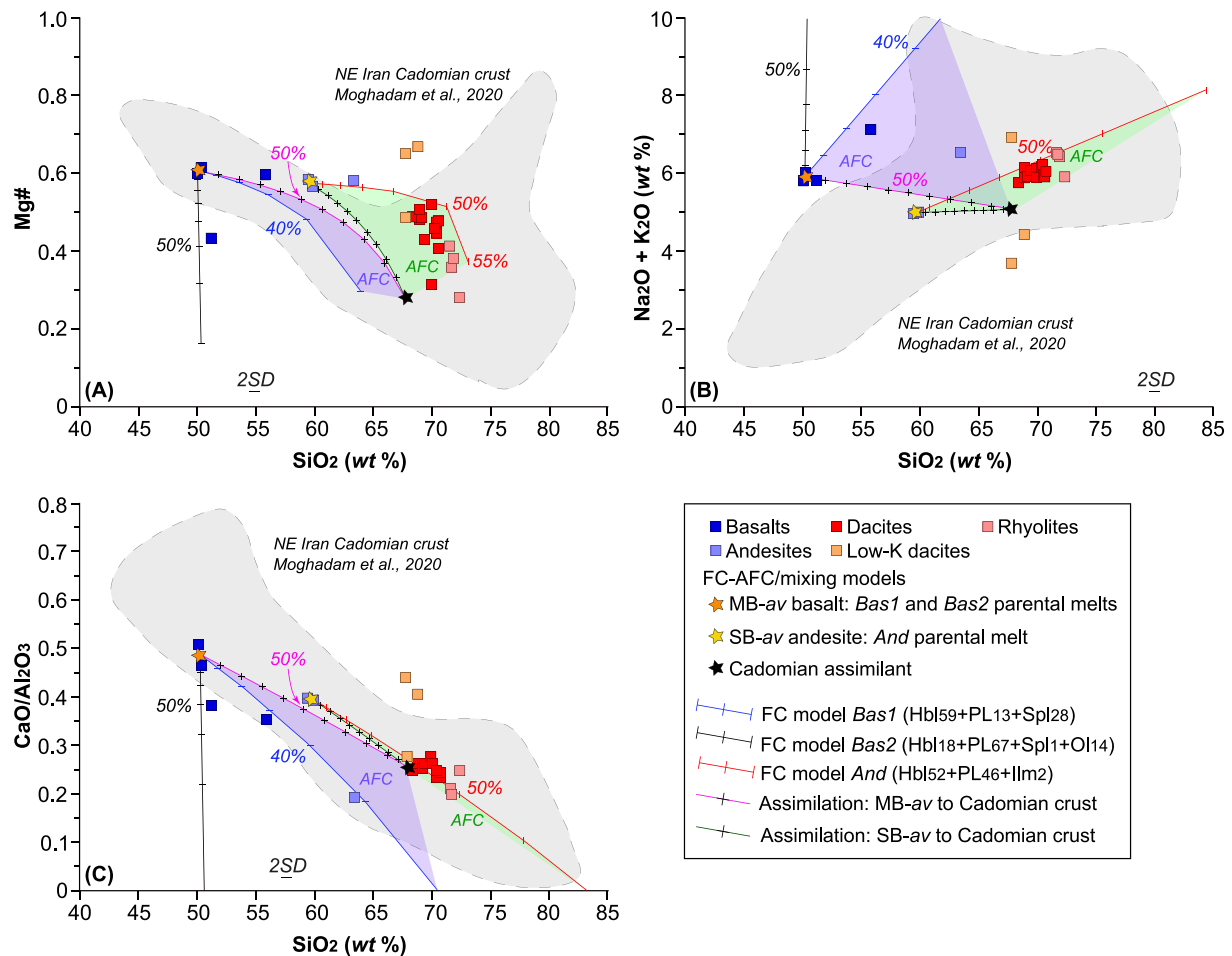
Figure 11. Fractional crystallization (FC) and assimilation-fractional crystallization (AFC) major element modeling of Quchan volcanic rocks. Major elements have been recalculated to 100% anhydrous, in the system SiO_2-TiO_2-Al_2O_3-FeO^*-MnO-MgO-CaO-Na_2O-K_2O. *Orange* and *yellow stars* represent the presumed parental melts; MB-av basalt (*Bas1* and *Bas2* parental melts) and SB-av andesite, respectively. *Blue* and *black lines* represent *Bas1* and *Bas2* fractionation trends respectively, as calculated for MB-av basaltic melt. The Red line represents *And* fractionation trend as calculated for SB-av andesitic melt. *Green* and *pink lines* represent maximum assimilation trends as calculated for the suspected parental SB-av andesitic and MB-av basaltic melts, respectively. The domains of possible AFC processes are presented in *green* and *purple shaded areas* (for SB-av andesitic and MB-av basaltic melts, respectively) situated between maximum assimilation/mixing- and FC- trends. The compositions of the Cadomian assimilant and the NE Iran Cadomian crust are taken from Moghadam, Li, Griffin, et al. (2020). The detailed description of the FC-AFC modeling using major elements is presented in Supporting Information S1.

this signature from the previous AFC processes which were responsible for the genesis of andesites, which can suggest there is no prerequisite for high-degree assimilation of Cadomian rocks.

5.3.3. Recharge, Evacuation, and Fractional Crystallization (REFC)

The wide compositional range of the Oligocene lavas in NE Iran, and the fact that some samples do not follow the AFC trends (Figure 12), together with the complex FC-AFC processes involving different fractionating assemblages and various degrees of crustal assimilation, suggests a magmatic build-up in deep "hot zones" and the persistence of an extensive magmatic feeding system maintained by a continuous recharge and evacuation of mafic magmas at the time of collisional magmatism. This idea can be also supported by the complex zoning of plagioclase and amphibole phenocrysts. A closed magmatic system without a magmatic recharge, in which the evolution of melts is driven only by FC-processes, will produce progressively smaller volumes of more residual liquids (e.g., Albarède, 1996; Lee et al., 2014) with up to 50% of melt cooling and crystallization, <2500 years as a result of the interaction with cold host rocks (Hawkesworth et al., 2000). In contrast, a continuous magmatic recharge in deep crust reservoirs will decrease both cooling and crystallization rates, and thus will sustain the mass of the residual liquids and can trigger a repeated
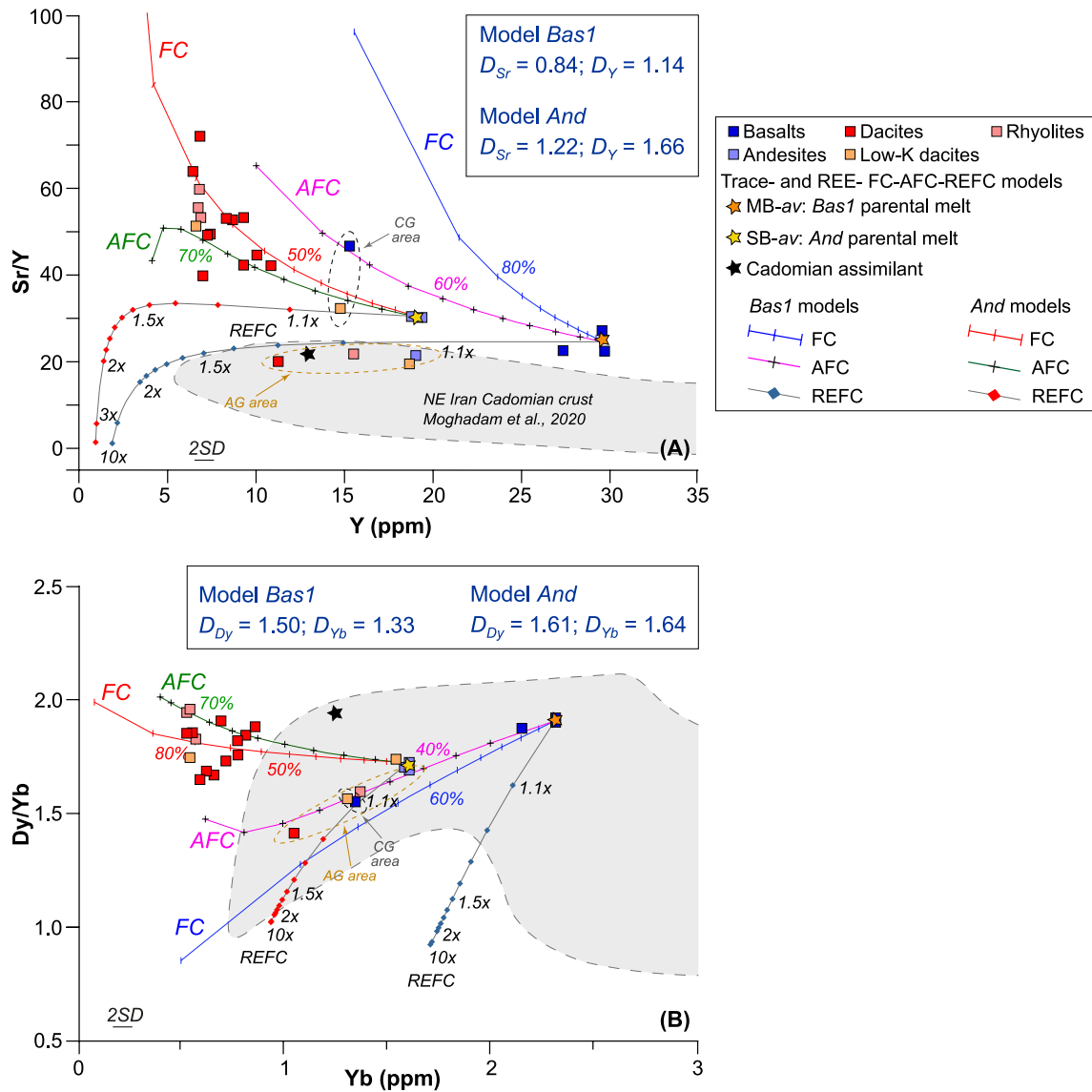
Figure 12. Sr/Y versus Y and Dy/Yb versus Yb diagrams illustrating the genesis of the Quchan volcanic rocks via FC-AFC of basaltic and andesitic parental melts represented by MB-*av* basalt (*Bas1*) and SB-av andesite, respectively. Bulk rock/melt partition coefficients used are reported in diagrams and were calculated following the procedure presented in Supporting Information S1. AFC curves represent De Paolo Assimilation and Fractional Crystallization solutions. The percentages indicate the amounts of fractionating assemblages. Equations and parameters used are presented in Supporting Information S1. We also tested the recharge, evacuation and fractional crystallization (REFC) model of Lee et al. (2014), using the same partition coefficients as for the FC-AFC trends. The REFC modeling was applied to both basaltic (MB-*av*) and andesitic (SB-*av*) parental melts and has been calculated to 10 times (10×) of the initial mass of the magma chamber ($M^0_{ch} = 1$). See text for explanation and Supporting Information S1 for details of the calculations.

ascent of melts into the upper parts of the feeding system (Annen et al., 2006a; Ginibre & Worner, 2007; Lucci et al., 2020). Furthermore, it has been demonstrated through numerical modeling that deep-crustal chambers undergoing prolonged or repeated recharge events are less prone to magma-evacuation concerning the shallower stagnation layers (Karlstrom et al., 2010). Such recharge can produce growing mafic to intermediate magma reservoirs by deforming and assimilating the surrounding lower-to middle crustal rocks (e.g., Karlstrom et al., 2010; Lee et al., 2014).

To evaluate the effect of the growing deep reservoir(s) on Quchan magmatism, we examined the REFC model of Lee et al. (2014). However, since the literature contains few well-documented examples of REFC-type magmatic systems (e.g., Portnyagin et al., 2015 and references therein), we approached the mode-
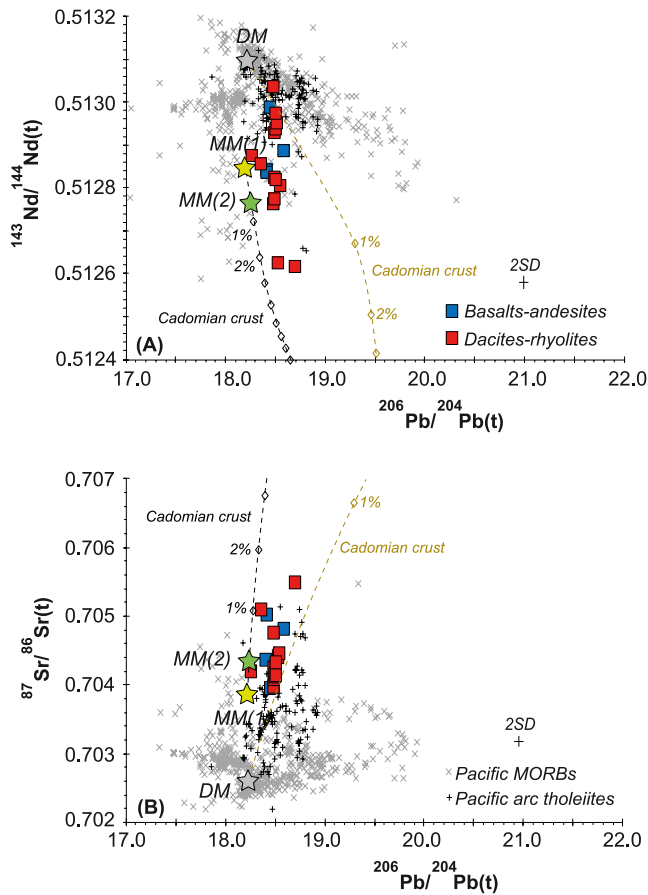
Figure 13. Mixing mass balance modeling of the initial $^{143}Nd/^{144}Nd$ (a) and $^{87}Sr/^{86}Sr$ (b) isotopic ratios versus $^{206}Pb/^{204}Pb$, using the depleted mantle (DM) and Cadomian continental crust endmembers to unravel the isotopic signatures of the Quchan magmatic rocks. Mixing mass balance modeling is also presented between mixed mantle (1) (MM (1), i.e., 90% depleted mantle + 6% subducted sediments + 4% altered oceanic crust, AOC) and the Cadomian continental crust of Iran. Diamond marks on curves show 1%–10% mixing between endmembers. Data for Pacific MORBs and Pacific arc tholeiites are from EarthChem (https://www.earthchem.org). Geochemical data for Late Cretaceous to Pleistocene magmatic rocks are from Moghadam, Li, Li, et al. (2020). All data including those for MORBs and arc tholeiites have been corrected for 24 Ma radiogenic growth.

ling through a conservative hypothesis assuming (a) the recharge rate ($dM_r = 0.4$) is higher than the sum of crystallization and evacuation rates ($dM_x + dM_e = -0.3$), and this corresponds to a magma chamber growth of 10% ($DM_{ch} = +0.1$) at each overturn; and (b) possible large fractionation between incompatible trace and REE elements can be achieved as a function of the crystallizing phases involved (e.g., Lee et al., 2006; Portnyagin et al., 2015). Using the same partition coefficients as in our FC-AFC models, the REFC modeling was applied to both basaltic (MB-av) and andesitic (SB-av) reservoirs and calculated up to 10 times (10×) the initial mass of the magma chamber ($M^0_{ch} = 1$).

Results are reported in Table S5 and presented in Figure 12. Compared to pure FC, the REFC modeling for the basaltic reservoir suggests an interesting scenario characterized by (a) a progressive depletion of Sr in residual liquids compared to the Sr enrichment in the FC-trend, (b) a stronger depletion of Y and (c) less fractionation of HREEs. We emphasize that the progressive growth of the basaltic reservoir seems to have no direct influence on the HREE budget in the evolved melts. On the other hand, nearly all Quchan volcanic rocks are included in the compositional space between FC and REFC trends, when departing from the same MB-av parental melt in the Sr-Y plot (Figure 12a).

The complexity behind the evolution of magmas in the Quchan volcanic system can be described by three samples from the same AG locality: AG-12-3 andesite, AG12-4 dacite and AG12-1 rhyolite. These three samples (a) show Sr-Y signatures close to the Cadomian assimilants (Figure 12a); (b) can be interpreted as daughter liquids after *ca* 50% fractionation of the andesitic SB-av melt; (c) can be interpreted as fractionated melts extracted by a progressive growth (1.3×) of the deeper basaltic reservoir; (d) can be produced by 60%–80% AFC of a pristine basaltic melt; or (e) can represent the evolved melts extracted from a growing (1.1–1.2×) andesitic reservoir (Figure 12a). We suggest that all these scenarios may have occurred during the genesis of AG rocks, as might be expected in a real magmatic plumbing system. However, since non-adakitic sample AG12-1 has higher $\varepsilon Nd(t)$ and $\varepsilon Hf(t)$, we suggest this sample can be considered as a fractionated melt, extracted during the progressive growth of deeper basaltic reservoirs with more juvenile isotopic signatures than the other rocks.

The FC-AFC-REFC models presented in this study highlight the general perspective of magmatic plumbing systems toward an innovative vision of magmatic feeding systems made up of multiple types of transport of basaltic magmas and storage chambers distributed within the crust. In these settings, multi-stage open-system processes such as the FC-AFC processes can lead to the evolution of magmas to yield felsic rocks and/or via AFC and extreme amphibole fractionation to produce adakites.

5.3.4. Isotope Modeling of Subducted Trench Sediments Added to DM

We have used Sr-Nd-Pb isotope modeling (Figure 13) to further investigate the role of mantle heterogeneity as well as crustal contamination (or AFC) in the genesis of the Quchan felsic rocks. However, the other ambiguity is that the Quchan basalts show depletion in Nb-Ta except for sample MB12-2 which lacks such depletion; all these basalts have Nb/La~0.6 to 1. Sample MB12-2 with less of a subduction signature has REE- and trace-element patterns similar to enriched MORBs and shows derivation from an enriched mantle. However, this sample with $\varepsilon Nd(t) = 4.4$ and $\varepsilon Hf(t) = 9.5$, still has radiogenic Pb-isotope ratios with $\Delta 8/4$–60.1, which show the involvement of components from subducted sediments in their mantle source. Using trace elements, we suggested that a 90:6:4 mixture of DM, terrigenous trench sediment and altered

oceanic crust, following 5% aggregated fractional melting (and/or 89:11 mixture of DM and Eastern Mediterranean Sea sediments, following 6% aggregated fractional melting) could produce modeled melts that are geochemically close to the composition of the Quchan basalts (except for sample MB14-2 which needs an enriched mantle with less input from the subducting sediments). Again, we clarify that our trace elements model is not a unique solution to explain the genesis of all basaltic rocks, but this model is geologically reasonable. To better understand the role of mantle heterogeneity and crustal contamination, we have further used mass-balance modeling to calculate the Sr, Nd and Pb isotopic composition of a mixed mantle (1) and (2) (MM(1) and MM(2) in Figure 9) sources using both mixtures of 90:6:4 of DM, terrigenous trench sediment, altered oceanic crust, and 89:11 of DM and Eastern Mediterranean Sea sediment– probably similar to the depleted mantle-sediment melange model suggested by Marschall and Schumacher (2012). The mixed mantle (1) has $^{87}Sr/^{86}Sr = 0.70386$, $^{143}Nd/^{144}Nd = 0.51283$ and $^{206}Pb/^{204}Pb = 18.20$, which are quite similar to the isotopic signatures of the selected basalts (both samples MB12-1 and MB12-2) with $^{87}Sr/^{86}Sr = 0.70434$ to 0.70500, $^{143}Nd/^{144}Nd = 0.512834$ to 0.512884 and $^{206}Pb/^{204}Pb = 18.42$ to 18.59. On other hand, the mixed mantle (2) has $^{87}Sr/^{86}Sr = 0.70434$, $^{143}Nd/^{144}Nd = 0.51276$ and $^{206}Pb/^{204}Pb = 18.22$ isotopic ratios that are slightly unradiogenic in Nd but radiogenic in Sr and Pb compared to the mixed mantle (1) (Figure 13). Then the mixing trends between a depleted mantle (DM) and Cadomian continental crust and also between the mixed mantle (1) (MM(1)) and the Cadomian continental crust have been modeled. All parameters for modeling are presented in Table S6.

Our modeling displays two features. (a) The Quchan samples show two mixing trends (Figure 13), one between the depleted mantle and Cadomian continental crust and the second one between the mixed mantle (1) and the Cadomian continental crust. These trends are better recognized in the Nd versus Pb isotope plot. (b) The mixed mantle (1) can produce the Nd-Pb isotopic signatures of the basalt samples MB12-1 and MB12-2, although the $^{87}Sr/^{86}Sr_{(t)}$ value in sample MB12-2 is a bit higher than in sample MB12-1. This mixed mantle (1) can melt to produce the Quchan basalts, although it should produce basalts with Nb-Ta depletion. Since basalt sample MB12-2 shows no clear Nb-Ta depletion (and together with sample MB12-1 displays less enrichment in Rb, Ba, U and Th compared to the modeled melt), it could be derived from a distinct, but enriched source—compared to the other Quchan basalts– possibly with the addition of lesser amounts of subducting sediments. Therefore, the isotopic data require at least three components, which are also recognized in the trace elements of basalts and felsic rocks using our modeling for the mantle source (Section 5.1) and FC-AFC processes (Section 5.3). Our modeling suggests that the isotopic signatures of the Quchan lavas most likely reside in both the lithospheric mantle and in the Cadomian continental crust of Iran.

5.4. Magmatism in NE Iran

5.4.1. Formation of Quchan Rocks

Our results are graphically summarized in Figure 14 and show that the geochemical-isotopic variations in Quchan lavas can be provided first by both sub-continental lithospheric mantle and then by the Cadomian continental crust of Iran. However, since the Quchan rocks have mostly high $\varepsilon Nd(t)>+4$ and $\varepsilon Hf(t)>+6$, it can be assumed that these isotopic values are not consistent with the presence of a lithospheric mantle (unless that lithospheric mantle was itself a previous subducted slab), but instead could attest to a variably depleted mantle beneath an oceanic back-arc or an intraoceanic arc system. We must emphasize that there is neither any trace of an oceanic back-arc basin during the Late Oligocene in NE Iran nor evidence for an intraoceanic arc within the narrow Sabzevar-Torbat-e-Heydarieh fossilized back-arc basin. However, the radiogenic Nd and Hf isotopes for the Quchan rocks can be inherited from the pre-existing depleted mantle which prevailed beneath the Late Creta-
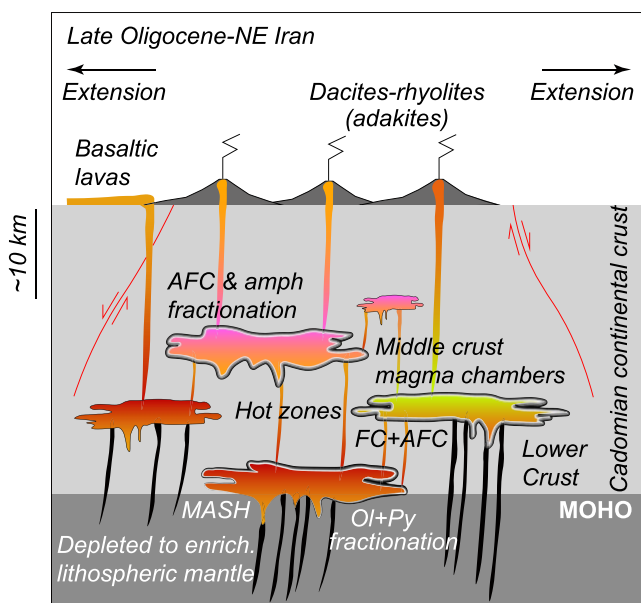

Figure 14. Schematic representation of the magmatic processes to yield the Quchan mafic and felsic rocks. Melting of a depleted to enriched (refertilized) lithospheric mantle and further fractional crystallization of olivine (Ol) and pyroxene (Py) in lower crust magma chambers produce the more evolved melts. These evolved melts further undergone fractional crystallization and assimilation-fractional crystallization in lower to middle magma chambers (hot zones) along with extreme amphibole crystallization to produce felsic and/or adakitic rocks. Black dikes display the melt conduits for primitive basaltic melts to enter the Melting, Assimilation, Storage, and Homogenization (MASH) zones in the deep lower crust, whereas colored dikes show the migration of evolved magmas into shallow magma chambers and/or into the surface.

ceous-Paleocene Sabzevar-Torbat-e-Heydarieh back-arc basin. According to our major- and trace-element and Sr-Nd-Pb modeling, we suggest a four-stage scenario for the formation of the Quchan lavas. (a) Melting of a metasomatized mantle, a DM re-fertilized by altered oceanic crust, trench sediments and/or sediment melts, to produce the original basaltic melts. The refertilization of the mantle can have occurred during the previous subduction, that is, from Late Cretaceous to Oligocene (*ca* 27 Ma). However, our isotopic modeling shows that both depleted and refertilized mantle sources seem to be involved during the magma genesis. (b) Early fractionation of olivine and pyroxene from basaltic melts in lower-to middle-crust hot zones to produce more-evolved (andesitic) melts with higher H_2O contents. (c) Extensive fractionation of amphibole and assimilation of continental crust (AFC) in the middle crust and shallow magma chambers, to produce the adakitic magmas with spoon-like MREE-HREE patterns. This process would further perturb the isotopic ratios of the Quchan magmas. (d) Recharge of magma chambers to perturb the geochemical-isotopic systematics of fractionated magmas, which can further suffer AFC processes to generate the felsic rocks. Empirical models suggest that hydrous basaltic magmas can stall in the lower-middle continental crust, in hot zones, and fractionate to produce crystal mush (e.g., Annen et al., 2006a, 2006b; Bachmann & Bergantz, 2008; Hidalgo & Rooney, 2014; Hidalgo et al., 2007). The crystal mush or the hot zones can be replenished by new pulses of basaltic magmas. These processes that is, replenishment and thus magmatic fractionation, can explain the oscillatory zoning in amphibole and plagioclase and the variable isotopic signatures of the fractionated rocks. Extreme amphibole fractionation could be expected to generate amphibole cumulates in the middle-lower crust. Outcrops of these cumulates are lacking in the Quchan area, which is covered by Oligocene magmatic rocks and younger volcanic-sedimentary rocks, but there are 1–2 m thick layers of amphibole (±<10 clinopyroxenes) cumulates in other outcrops in NE Iran that accompany deep-seated, deformed Eocene granodiorites and diorites. These cumulates are similar to mono-mineralic amphibole cumulates reported from continental arcs worldwide, for example, Antarctica (Tiepolo & Tribuzio, 2008), south China (Sun & Zhou, 2008) and from southern and central American volcanic arcs. Crystallization of amphibole cumulates in the middle crust, along with assimilation of continental crust, could rapidly increase the SiO_2 content of the residual magmas (e.g., Carmichael, 2002), which could produce Quchan dacites and rhyolites upon eruption. Amphibole fractionation and AFC processes further can generate residual magmas with adakitic geochemical compositions (Castillo et al., 1999).

5.4.2. Magmatic Triggers in NE Iran

Zircon U-Pb, K-Ar, and Ar-Ar ages imply that magmatism in the NE Iran back-arc started in the Mid-Late Cretaceous (~110 Ma) and continued until the Pleistocene (e.g., Alaminia et al., 2013; Ghasemi et al., 2010; Jamshidi et al., 2015; Kazemi et al., 2019; Rostami-Hossouri et al., 2020; Shabanian et al., 2012, among others). Late Cretaceous magmatism in the NE Iran back-arc is consistent with subduction initiation along the Zagros suture zone or the Main Zagros Thrust (MZT) at *ca* 110-100 Ma and along the Makran zone in south Iran (e.g., Barbero et al., 2020; Burg, 2018; Esmaeili et al., 2020; Moghadam & Stern, 2011; Moghadam et al., 2010; Moghadam, Khedr, et al., 2014; Monsef et al., 2018) (Figure 1a). Subduction initiation drove extension in the overlying plate of the Iranian plateau, caused exhumation of high-pressure rocks (blueschists) along with the Zagros ophiolites (Angiboust et al., 2016; Moghadam et al., 2017) and triggered the formation of back-arc oceanic basins within the Iranian plateau, such as the Sabzevar-Torbat-e-Heydarieh oceanic back-arc in NE Iran (Moghadam, Corfu, et al., 2014). This extension was also responsible for a high rate of magmatism in the Iranian plateau, mainly in the NE segment. This Mid-Late Cretaceous magmatism in the NE Iran back-arc is represented by arc tholeiites and calc-alkaline rocks (Figure 6).

The NE Iran magmatism entered a waning stage during Paleocene to Early Eocene time coeval with the exhumation of blueschists and thus the closure of the Sabzevar-Torbat-e-Heydarieh back-arc oceanic basin (Bröcker et al., 2021). The Paleocene to Early Eocene magmatism is characterized by highly radiogenic arc-tholeiitic to calc-alkaline igneous rocks. Magmatism began to increase during the Middle Eocene (48–40 Ma), coeval with flare-up magmatism in other segments of both the magmatic front and back-arcs in Iran (Moghadam, Li, Li, et al., 2020; van der Boon et al., 2021). High magmatic fluxes during the Eocene were accompanied by extension throughout the Iranian plateau driven by the roll-back of the Neotethyan slab (Chiu et al., 2013; Verdel et al., 2007). The extension was accompanied by core-complex formation, basin deepening and subsidence, leaving a thick sequence of Nummulite-bearing limestones and green marine pyroclastic rocks, which are accompanied by and/or interlayered with Eocene volcanic rocks (Kargaranbafghi & Neubauer, 2015; Kargaranbafghi et al., 2012, 2015; Moghadam et al., 2018; Verdel et al., 2007). The

Eocene magmatism in NE Iran shows both calc-alkaline and adakitic geochemical signatures (Figure 6). Magmatism seems to have waned during the Late Eocene and restarted during the Mid-Late Oligocene, after the collision between Arabia and Eurasia at ∼27 Ma. Magmatism continued during Miocene and Pleistocene time in NE Iran with the eruption of subaerial andesites from NE Iran (NW Torbat-e-Heydarieh). Oligocene and younger magmatic rocks from NE Iran show enrichment in large ion lithophile elements and depletion in high field strength elements, and these magmas are inferred to be mainly derived from a subduction-modified mantle source, refertilized by subduction components from subducting Neotethyan oceanic lithosphere beneath Iran, before Iran and Arabia collided at *ca* 27 Ma.

Since there is ∼600 km between the magmatic front (Urumieh-Dokhtar magmatic belt, Figure 1) and back-arc region in NE Iran, some believe that the Cenozoic magmatism in NE Iran could be related to the subduction and thus closure of the Neotethyan branches or the Sabzevar-Torbat-e-Heydarieh oceanic back-arc basin in NE Iran (e.g., Moghadam, Khedr, et al., 2015). We would argue that (a) the distance between the magmatic front and back-arcs is controlled mainly by the dip of the subducting slab; (b) in most retreating arcs, the back-arc magmatic belt is mostly restricted to ∼100–300 km from the magmatic front (as in the southern Andean subduction system); (c) in some subduction systems—for example, extensional ones—the back-arc magmatism is located far away from the trench. For example, the Cenozoic back-arc magmatism in the Oligocene San Juan Volcanic Field (USA) could be traced ∼1,000 km away from the trench (Lake & Farmer, 2015).

We cannot rule out the subduction of the Neotethyan back-arc lithosphere in NE Iran, but the polarity of this subduction has been challenged. Many argue that the back-arc lithosphere has been subducted toward the north—beneath the Turan Plate—and thus has produced the Quchan Oligocene rocks (e.g., Ghasemi et al., 2010), but without a trace of Late Cretaceous-Eocene magmatism. However, the "collisional" or "collision-related" terms we use in this study refer to the magmatism occurring after the collision between Iran and Arabia at ∼27 Ma, which is abundant in all parts of Iran. The tectonic forces needed for continental collision—that is, those related to the opening of the Red Sea and convergence between Arabia and Iran– could also be a trigger for the closure of the Sabzevar-Torbat-e-Heydarieh oceanic basin in NE Iran, although the exhumation of the Paleocene-Early Eocene blueschists in the Sabzevar-Torbat-e-Heydarieh oceanic basin (Bröcker et al., 2021) and the deposition of Paleocene-Eocene basal conglomerates (+terrigenous sediments upwards the section) to seal these ophiolites show that this Neotethyan back-arc basin was closed earlier than Late Oligocene.

6. Conclusions

Late Cretaceous to Pleistocene magmatic rocks are common in NE Iran and are related to the subduction initiation beneath the Iranian Plateau during Late Cretaceous and then to a magmatic flare-up in Eocene time due to the Neotethyan rollback, and finally to the collision between Iran and Arabia at *ca* 27 Ma. Late Oligocene volcanic rocks including basalts, andesites, dacites and rhyolites are abundant in NE Iran (south Quchan), with the felsic rocks showing zircon U-Pb ages of 25–24 Ma. These rocks have subduction-related geochemical signatures and are characterized by variable Sr-Nd-Pb-Hf isotope compositions. The geochemical compositions of Quchan basalts are generally in agreement with partial melting of a refertilized mantle, generated by the interaction of a depleted mantle with subducting altered oceanic crust and overlying sediments. However, the Sr-Nd-Pb isotopic ratios and modeling could highlight that both a depleted and an enriched mantle were involved in the genesis of the Quchan rocks. Fractional crystallization and assimilation-fractional crystallization models imply that basaltic melts could pool in the lower crust and fractionation of early olivine and clinopyroxene can yield fractionated, H_2O-rich melts. These evolved melts can foster extreme amphibole fractionation in the lower-middle crustal hot zone, along with assimilation of the Cadomian continental crust, to produce the Quchan felsic rocks and/or adakites.

Data Availability Statement

All data underlying the finding of this paper can be accessed from both Supporting Information S1 and http://dx.doi.org/10.17632/8zm7zkrrnb.1.

References

Ahmadi, P., Ghorbani, M. R., Coltorti, M., Kuritani, T., Cai, Y., Fioretti, A. M., et al. (2017). High-Nb hawaiite–mugearite and high-Mg calc-alkaline lavas from northeastern Iran: Oligo-Miocene melts from modified mantle wedge. *International Geology Review*, *61*(2), 150–174. https://doi.org/10.1080/00206814.2017.1416502

Alaminia, Z., Karimpour, M. H., Homam, S. M., & Finger, F. (2013). The magmatic record in the Arghash region (northeast Iran) and tectonic implications. *International Journal of Earth Sciences*, *102*(6), 1603–1625. https://doi.org/10.1007/s00531-013-0897-1

Alavi, M. (1991). Sedimentary and structural characteristics of the Paleo-Tethys remnants in northeastern Iran. *Geological Society of America Bulletin*, *103*(8), 983–992. https://doi.org/10.1130/0016-7606(1991)103<0983:sascot>2.3.co;2

Albarède, F. (1996). *Introduction to geochemical modeling*. Cambridge University Press.

Alexander, E., Wielicki, M., Harrison, T., DePaolo, D., Zhao, Z., & Zhu, D. (2019). Hf and Nd isotopic constraints on pre-and syn-collisional crustal thickness of southern Tibet. *Journal of Geophysical Research: Solid Earth*, *124*(11), 11038–11054. https://doi.org/10.1029/2019jb017696

Allen, M. B., Kheirkhah, M., Neill, I., Emami, M. H., & Mcleod, C. L. (2013). Generation of arc and within-plate chemical signatures in collision zone magmatism: Quaternary lavas from Kurdistan Province, Iran. *Journal of Petrology*, *54*(5), 887–911. https://doi.org/10.1093/petrology/egs090

Allen, M. B., Mark, D. F., Kheirkhah, M., Barfod, D., Emami, M. H., & Saville, C. (2011). $^{40}Ar/^{39}Ar$ dating of Quaternary lavas in northwest Iran: Constraints on the landscape evolution and incision rates of the Turkish-Iranian plateau. *Geophysical Journal International*, *185*(3), 1175–1188. https://doi.org/10.1111/j.1365-246x.2011.05022.x

Angiboust, S., Agard, P., Glodny, J., Omrani, J., & Oncken, O. (2016). Zagros blueschists: Episodic underplating and long-lived cooling of a subduction zone. *Earth and Planetary Science Letters*, *443*, 48–58. https://doi.org/10.1016/j.epsl.2016.03.017

Annen, C., Blundy, J. D., & Sparks, R. S. J. (2006a). The genesis of intermediate and silicic magmas in deep crustal hot zones. *Journal of Petrology*, *47*(3), 505–539. https://doi.org/10.1093/petrology/egi084

Annen, C., Blundy, J. D., & Sparks, R. S. J. (2006b). The sources of granitic melt in Deep Hot Zones. *Transactions of the Royal Society of Edinburgh-Earth Sciences*, *97*, 297–309. https://doi.org/10.1017/S0263593300001462

Aragon, E., Pinotti, L., D'Eramo, F., Castro, A., Rabbia, O., Coniglio, J., et al. (2013). The Farallon-Aluk ridge collision with South America: Implications for the geochemical changes of slab window magmas from fore- to back-arc. *Geoscience Frontiers*, *4*(4), 377–388. https://doi.org/10.1016/j.gsf.2012.12.004

Azizi, H., Lucci, F., Stern, R. J., Hasannejad, S., & Asahara, Y. (2018). The Late Jurassic Panjeh submarine volcano in the northern Sanandaj-Sirjan Zone, northwest Iran: Mantle plume or active margin? *Lithos*, *308–309*, 364–380. https://doi.org/10.1016/j.lithos.2018.03.019

Azizi, H., & Stern, R. J. (2020). Jurassic igneous rocks of the Sanandaj-Sirjan zone of Iran mark a hotspot track, not a magmatic arc. *Terra Nova*.

Bachmann, O., & Bergantz, G. W. (2008). Rhyolites and their source mushes across tectonic settings. *Journal of Petrology*, *49*(12), 2277–2285. https://doi.org/10.1093/petrology/egn068

Ballato, P., Uba, C. E., Landgraf, A., Strecker, M. R., Sudo, M., Stockli, D. F., et al. (2011). Arabia-Eurasia continental collision: Insights from late Tertiary foreland-basin evolution in the Alborz Mountains, northern Iran. *Geological Society of America Bulletin*, *123*(1–2), 106–131. https://doi.org/10.1130/b30091.1

Barbero, E., Delavari, M., Dolati, A., Saccani, E., Marroni, M., Catanzariti, R., & Pandolfi, L. (2020). The Ganj Complex reinterpreted as a Late Cretaceous volcanic arc: Implications for the geodynamic evolution of the North Makran domain (southeast Iran). *Journal of Asian Earth Sciences*, *195*, 104306. https://doi.org/10.1016/j.jseaes.2020.104306

Bauman, A., Spies, O., & Lensch, G. (1983). *Strontium isotopic composition of post-ophiolitic Tertiary volcanic between Kashmar, Sabzevar and Quchan NE Iran*. Geological Survey of Iran.

Bea, F., Montero, P., & Ortega, M. (2006). A LA–ICP–MS evaluation of Zr reservoirs in common crustal rocks: Implications for Zr and Hf geochemistry, and zircon-forming processes. *The Canadian Mineralogist*, *44*(3), 693–714. https://doi.org/10.2113/gscanmin.44.3.693

Berberian, M., & King, G. C. P. (1981). Towards a paleogeography and tectonic evolution of Iran. *Canadian Journal of Earth Sciences*, *18*(2), 210–265. https://doi.org/10.1139/e81-019

Bröcker, M., Omrani, H., Berndt, J., & Moslempour, J. M. E. (2021). Unravelling metamorphic ages of suture zone rocks from the Sabzevar and Makran areas (Iran): Robust age constraints for the larger Arabia-Eurasian collision zone. *Journal of Metamorphic Geology*, 1–31.

Burg, J.-P. (2018). Geology of the onshore Makran accretionary wedge: Synthesis and tectonic interpretation. *Earth-Science Reviews*, *185*, 1210–1231. https://doi.org/10.1016/j.earscirev.2018.09.011

Carmichael, I. S. (1991). The redox states of basic and silicic magmas: A reflection of their source regions? *Contributions to Mineralogy and Petrology*, *106*(2), 129–141. https://doi.org/10.1007/bf00306429

Carmichael, I. S. E. (2002). The andesite aqueduct: Perspectives on the evolution of intermediate magmatism in west-central (105–99°W) Mexico. *Contributions to Mineralogy and Petrology*, *143*(6), 641–663. https://doi.org/10.1007/s00410-002-0370-9

Castillo, P. R. (2006). An overview of adakite petrogenesis. *Chinese Science Bulletin*, *51*(3), 257–268. https://doi.org/10.1007/s11434-006-0257-7

Castillo, P. R. (2012). Adakite petrogenesis. *Lithos*, *134–135*(0), 304–316. https://doi.org/10.1016/j.lithos.2011.09.013

Castillo, P. R., Janney, P. E., & Solidum, R. U. (1999). Petrology and geochemistry of Camiguin Island, southern Philippines: Insights to the source of adakites and other lavas in a complex arc setting. *Contributions to Mineralogy and Petrology*, *134*(1), 33–51. https://doi.org/10.1007/s004100050467

Chiaradia, M. (2009). Adakite-like magmas from fractional crystallization and melting-assimilation of mafic lower crust (Eocene Macuchi arc, Western Cordillera, Ecuador). *Chemical Geology*, *265*(3–4), 468–487. https://doi.org/10.1016/j.chemgeo.2009.05.014

Chiaradia, M., Muntener, O., Beate, B., & Fontignie, D. (2009). Adakite-like volcanism of Ecuador: Lower crust magmatic evolution and recycling. *Contributions to Mineralogy and Petrology*, *158*(5), 563–588. https://doi.org/10.1007/s00410-009-0397-2

Chiu, H. Y., Chung, S. L., Zarrinkoub, M. H., Mohammadi, S. S., Khatib, M. M., & Iizuka, Y. (2013). Zircon U-Pb age constraints from Iran on the magmatic evolution related to Neotethyan subduction and Zagros orogeny. *Lithos*, *162*, 70–87. https://doi.org/10.1016/j.lithos.2013.01.006

Chung, S.-L., Chu, M.-F., Zhang, Y., Xie, Y., Lo, C.-H., Lee, T.-Y., et al. (2005). Tibetan tectonic evolution inferred from spatial and temporal variations in post-collisional magmatism. *Earth-Science Reviews*, *68*(3–4), 173–196. https://doi.org/10.1016/j.earscirev.2004.05.001

Conticelli, S., Guarnieri, L., Farinelli, A., Mattei, M., Avanzinelli, R., Bianchini, G., et al. (2009). Trace elements and Sr-Nd-Pb isotopes of K-rich, shoshonitic, and calc-alkaline magmatism of the Western Mediterranean Region: Genesis of ultrapotassic to calc-alkaline magmatic associations in a post-collisional geodynamic setting. *Lithos*, *107*(1–2), 68–92. https://doi.org/10.1016/j.lithos.2008.07.016

Cvetkovic, V., Saric, K., Prelevic, D., Genser, J., Neubauer, F., Hock, V., & von Quadt, A. (2013). An anorogenic pulse in a typical orogenic setting: The geochemical and geochronological record in the East Serbian latest Cretaceous to Palaeocene alkaline rocks. *Lithos*, *180*, 181–199.

Davidson, J., Turner, S., Handley, H., Macpherson, C., & Dosseto, A. (2007). Amphibole "sponge" in arc crust? *Geology*, *35*(9), 787–790. https://doi.org/10.1130/g23637a.1

Davidson, J., Turner, S., & Plank, T. (2013). Dy/Dy*: Variations arising from mantle sources and petrogenetic processes. *Journal of Petrology*, *54*(3), 525–537. https://doi.org/10.1093/petrology/egs076

Davidson, J. P. (1996). *Deciphering mantle and crustal signatures in subduction zone magmatism. Subduction: Top to bottom* (Vol. 96, pp. 251–262).

Deer, W. A., Howie, R. A., & Zussman, J. (1992). *An introduction to the rock forming minerals*. Longman.

Defant, M. J., & Drummond, M. S. (1990). Derivation of some modern arc magmas by melting of young subducted lithosphere. *Nature*, *347*(6294), 662–665. https://doi.org/10.1038/347662a0

Deng, C., Wan, B., Dong, L., Talebian, M., Windley, B. F., Dadashzadeh, H., et al. (2018). Miocene porphyry copper deposits in the Eastern Tethyan orogenic belt: Using Sr, O isotopes and Sr/Y ratios to predict the source of ore-related and ore-barren magmas. *Gondwana Research*, *62*, 14–26. https://doi.org/10.1016/j.gr.2018.03.007

DePaolo, D. J. (1981). A neodymium and strontium isotopic study of the Mesozoic calc-alkaline granitic batholiths of the Sierra Nevada and Peninsular Ranges, California. *Journal of Geophysical Research: Solid Earth*, *86*(B11), 10470–10488. https://doi.org/10.1029/jb086ib11p10470

Esmaeili, R., Xiao, W., Griffin, W., Moghadam, H. S., Zhang, Z., Ebrahimi, M., et al. (2020). Reconstructing the source and growth of the Makran Accretionary Complex: Constraints from detrital zircon U-Pb geochronology. *Tectonics*, *39*(2), e2019TC005963. https://doi.org/10.1029/2019tc005963

Gamshidi, K. H., Mirtohidi, I., & Nozari, A. (2000). *Geological map of Mashkan, Sheet 7563*. Geological Survey of Iran.

Ghasemi, H., Sadeghian, M., Khanalizadeh, A., & Tanha, A. (2010). Petrology, geochemistry and radiometric ages of high silica adakitic domes of Neogene continental arc, south of Quchan. *Iranian Journal of Crystallography and Mineralogy*, *18*(3), 347–370.

Ginibre, C., & Worner, G. (2007). Variable parent magmas and recharge regimes of the Parinacota magma system (N. Chile) revealed by Fe, Mg and Sr zoning in plagioclase. *Lithos*, *98*(1–4), 118–140. https://doi.org/10.1016/j.lithos.2007.03.004

Gómez-Tuena, A., Cavazos-Tovar, J. G., Parolari, M., Straub, S. M., & Espinasa-Pereña, R. (2018). Geochronological and geochemical evidence of continental crust 'relamination' in the origin of intermediate arc magmas. *Lithos*, *322*, 52–66. https://doi.org/10.1016/j.lithos.2018.10.005

Grove, T. L., Chatterjee, N., Parman, S. W., & Medard, E. (2006). The influence of H_2O on mantle wedge melting. *Earth and Planetary Science Letters*, *249*(1–2), 74–89. https://doi.org/10.1016/j.epsl.2006.06.043

Grove, T. L., Elkins-Tanton, L. T., Parman, S. W., Chatterjee, N., Muntener, O., & Gaetani, G. A. (2003). Fractional crystallization and mantle-melting controls on calc-alkaline differentiation trends. *Contributions to Mineralogy and Petrology*, *145*(5), 515–533. https://doi.org/10.1007/s00410-003-0448-z

Grove, T. L., Parman, S. W., Bowring, S. A., Price, R. C., & Baker, M. B. (2002). The role of an H_2O-rich fluid component in the generation of primitive basaltic andesites and andesites from the Mt. Shasta region, N California. *Contributions to Mineralogy and Petrology*, *142*(4), 375–396. https://doi.org/10.1007/s004100100299

Grove, T. L., Till, C. B., & Krawczynski, M. J. (2012). The role of H_2O in subduction zone magmatism. *Annual Review of Earth and Planetary Sciences*, *40*(40), 413–439. https://doi.org/10.1146/annurev-earth-042711-105310

Hart, S. R. (1984). A large-scale isotope anomaly in the Southern-Hemisphere mantle. *Nature*, *309*(5971), 753–757. https://doi.org/10.1038/309753a0

Hawkesworth, C., Blake, S., Evans, P., Hughes, R., Macdonald, R., Thomas, L., et al. (2000). Time scales of crystal fractionation in magma chambers—Integrating physical, isotopic and geochemical perspectives. *Journal of Petrology*, *41*(7), 991–1006. https://doi.org/10.1093/petrology/41.7.991

Hidalgo, P. J., & Rooney, T. O. (2014). Petrogenesis of a voluminous Quaternary adakitic volcano: The case of Baru volcano. *Contributions to Mineralogy and Petrology*, *168*(3), 1011. https://doi.org/10.1007/s00410-014-1011-9

Hidalgo, P. J., Vogel, T. A., Rooney, T. O., Currier, R. M., & Layer, P. W. (2011). Origin of silicic volcanism in the Panamanian arc: Evidence for a two-stage fractionation process at El Valle volcano. *Contributions to Mineralogy and Petrology*, *162*(6), 1115–1138. https://doi.org/10.1007/s00410-011-0643-2

Hidalgo, S., Monzier, M., Martin, H., Chazot, G., Eissen, J. P., & Cotten, J. (2007). Adakitic magmas in the Ecuadorian volcanic front: Petrogenesis of the Iliniza volcanic complex (Ecuador). *Journal of Volcanology and Geothermal Research*, *159*(4), 366–392. https://doi.org/10.1016/j.jvolgeores.2006.07.007

Huang, F., Rooney, T. O., Xu, J.-F., & Zeng, Y.-C. (2019). Magmatic record of continuous Neo-Tethyan subduction after initial India-Asia collision in the central part of southern Tibet. *GSA Bulletin*, *133*(7–8), 1600–1612.

Iveson, A. A., Rowe, M. C., Webster, J. D., & Neill, O. K. (2018). Amphibole-, clinopyroxene- and plagioclase-melt partitioning of trace and economic metals in halogen-bearing rhyodacitic melts. *Journal of Petrology*, *59*(8), 1579–1604. https://doi.org/10.1093/petrology/egy072

Jacques, G., Hoernle, K., Gill, J., Hauff, F., Wehrmann, H., Garbe-Schönberg, D., et al. (2013). Across-arc geochemical variations in the Southern Volcanic Zone, Chile (34.5–38.0°S): Constraints on mantle wedge and slab input compositions. *Geochimica et Cosmochimica Acta*, *123*, 218–243. https://doi.org/10.1016/j.gca.2013.05.016

Jacques, G., Hoernle, K., Gill, J., Wehrmann, H., Bindeman, I., & Lara, L. E. (2014). Geochemical variations in the Central Southern Volcanic Zone, Chile (38–43°S): The role of fluids in generating arc magmas. *Chemical Geology*, *371*, 27–45. https://doi.org/10.1016/j.chemgeo.2014.01.015

Jahn, B.-M., Wu, F., Lo, C.-H., & Tsai, C.-H. (1999). Crust–mantle interaction induced by deep subduction of the continental crust: Geochemical and Sr–Nd isotopic evidence from post-collisional mafic–ultramafic intrusions of the northern Dabie complex, central China. *Chemical Geology*, *157*(1–2), 119–146. https://doi.org/10.1016/s0009-2541(98)00197-1

Jamshidi, K., Ghasemi, H., Troll, V. R., Sadeghian, M., & Dahren, B. (2015). Magma storage and plumbing of adakite-type post-ophiolite intrusions in the Sabzevar ophiolitic zone, northeast Iran. *Solid Earth*, *6*(1), 49–72. https://doi.org/10.5194/se-6-49-2015

Kamenetsky, V. S., Crawford, A. J., & Meffre, S. (2001). Factors controlling chemistry of magmatic spinel: An empirical study of associated olivine, Cr-spinel and melt inclusions from primitive rocks. *Journal of Petrology*, *42*(4), 655–671. https://doi.org/10.1093/petrology/42.4.655

Kargaranbafghi, F., & Neubauer, F. (2015). Lithospheric thinning associated with formation of a metamorphic core complex and subsequent formation of the Iranian plateau. *Geological Society of America Today*, *25*(7), 4–8. https://doi.org/10.1130/gsatg229a.1

Kargaranbafghi, F., Neubauer, F., & Genser, J. (2015). Rapid Eocene extension in the Chapedony metamorphic core complex, Central Iran: Constraints from $^{40}Ar/^{39}Ar$ dating. *Journal of Asian Earth Sciences*, *106*, 156–168. https://doi.org/10.1016/j.jseaes.2015.03.010

Kargaranbafghi, F., Neubauer, F., Genser, J., Faghih, A., & Kusky, T. (2012). Mesozoic to Eocene ductile deformation of western Central Iran: From Cimmerian collisional orogeny to Eocene exhumation. *Tectonophysics*, *564*, 83–100. https://doi.org/10.1016/j.tecto.2012.06.017

Karlstrom, L., Dufek, J., & Manga, M. (2010). Magma chamber stability in arc and continental crust. *Journal of Volcanology and Geothermal Research*, *190*(3–4), 249–270. https://doi.org/10.1016/j.jvolgeores.2009.10.003

Kay, R. W., & Kay, S. M. (2002). Andean adakites: Three ways to make them. *Acta Petrologica Sinica*, *18*(3), 303–311.

Kazemi, Z., Ghasemi, H., Tilhac, R., Griffin, W., Moghadam, H. S., O'Reilly, S., & Mousivand, F. (2019). Late Cretaceous subduction-related magmatism on the southern edge of Sabzevar basin, NE Iran. *Journal of the Geological Society*, *176*(3), 530–552. https://doi.org/10.1144/jgs2018-076

Kelemen, P. B., & Behn, M. D. (2016). Formation of lower continental crust by relamination of buoyant arc lavas and plutons. *Nature Geoscience*, *9*(3), 197–205. https://doi.org/10.1038/ngeo2662

Kheirkhah, M., Neill, I., & Allen, M. B. (2015). Petrogenesis of OIB-like basaltic volcanic rocks in a continental collision zone: Late Cenozoic magmatism of Eastern Iran. *Journal of Asian Earth Sciences*, *106*, 19–33. https://doi.org/10.1016/j.jseaes.2015.02.027

Kheirkhah, M., Neill, I., Allen, M. B., & Ajdari, K. (2013). Small-volume melts of lithospheric mantle during continental collision: Late Cenozoic lavas of Mahabad, NW Iran. *Journal of Asian Earth Sciences*, *74*, 37–49. https://doi.org/10.1016/j.jseaes.2013.06.002

Kimura, J. I., & Ariskin, A. A. (2014). Calculation of water-bearing primary basalt and estimation of source mantle conditions beneath arcs: PRIMACALC2 model for WINDOWS. *Geochemistry, Geophysics, Geosystems*, *15*(4), 1494–1514. https://doi.org/10.1002/2014gc005329

Kimura, J.-I., Hacker, B. R., van Keken, P. E., Kawabata, H., Yoshida, T., & Stern, R. J. (2009). Arc Basalt Simulator version 2, a simulation for slab dehydration and fluid-fluxed mantle melting for arc basalts: Modeling scheme and application. *Geochemistry, Geophysics, Geosystems*, *10*(9). https://doi.org/10.1029/2008gc002217

Klaver, M., Djuly, T., de Graaf, S., Sakes, A., Wijbrans, J., Davies, G., & Vroon, P. (2015). Temporal and spatial variations in provenance of Eastern Mediterranean Sea sediments: Implications for Aegean and Aeolian arc volcanism. *Geochimica et Cosmochimica Acta*, *153*, 149–168. https://doi.org/10.1016/j.gca.2015.01.007

Kolb, M., Von Quadt, A., Peytcheva, I., Heinrich, C. A., Fowler, S. J., & Cvetkovic, V. (2013). Adakite-like and normal arc magmas: Distinct fractionation paths in the East Serbian segment of the Balkan-Carpathian arc. *Journal of Petrology*, *54*(3), 421–451. https://doi.org/10.1093/petrology/egs072

Lake, E. T., & Farmer, G. L. (2015). Oligo-Miocene mafic intrusions of the San Juan Volcanic Field, southwestern Colorado, and their relationship to voluminous, caldera-forming magmas. *Geochimica et Cosmochimica Acta*, *157*, 86–108. https://doi.org/10.1016/j.gca.2015.02.020

Leake, B. E., Woolley, A. R., Arps, C. E. S., Birch, W. D., Gilbert, M. C., Grice, J. D., et al. (1997). Nomenclature of amphiboles: Report of the subcommittee on amphiboles of the International Mineralogical Association Commission on new minerals and mineral names. *Canadian Mineralogist*, *35*, 219–246.

Leake, B. E., Woolley, A. R., Birch, W. D., Gilbert, M. C., Grice, J. D., Hawthorne, F. C., et al. (1997). Nomenclature of amphiboles: Report of the subcommittee on amphiboles of the International Mineralogical Association Commission on new minerals and mineral names. *European Journal of Mineralogy*, *9*(3), 623–651. https://doi.org/10.1127/ejm/9/3/0623

Lebas, M. J., Lemaitre, R. W., Streckeisen, A., & Zanettin, B. (1986). A chemical classification of volcanic rocks based on the total alkali silica diagram. *Journal of Petrology*, *27*(3), 745–750. https://doi.org/10.1093/petrology/27.3.745

Lee, C.-T. A., Cheng, X., & Horodyskyj, U. (2006). The development and refinement of continental arcs by primary basaltic magmatism, garnet pyroxenite accumulation, basaltic recharge and delamination: Insights from the Sierra Nevada, California. *Contributions to Mineralogy and Petrology*, *151*(2), 222–242. https://doi.org/10.1007/s00410-005-0056-1

Lee, C. T. A., Lee, T. C., & Wu, C. T. (2014). Modeling the compositional evolution of recharging, evacuating, and fractionating (REFC) magma chambers: Implications for differentiation of arc magmas. *Geochimica et Cosmochimica Acta*, *143*, 8–22. https://doi.org/10.1016/j.gca.2013.08.009

Li, X.-H., Zhou, H., Chung, S.-L., Lo, C.-H., Wei, G., Liu, Y., & Lee, C.-y. (2002). Geochemical and Sr-Nd isotopic characteristics of late Paleogene ultrapotassic magmatism in southeastern Tibet. *International Geology Review*, *44*(6), 559–574. https://doi.org/10.2747/0020-6814.44.6.559

Lin, Y.-C., Chung, S.-L., Bingöl, A. F., Yang, L., Okrostsvaridze, A., Pang, K.-N., et al. (2020). *Diachronous initiation of post-collisional magmatism in the Arabia-Eurasia collision zone. Lithos*. (Vol. *356*, p. 105394). https://doi.org/10.1016/j.lithos.2020.105394

Liu, D., Zhao, Z., Zhu, D.-C., Niu, Y., DePaolo, D. J., Harrison, T. M., et al. (2014). Postcollisional potassic and ultrapotassic rocks in southern Tibet: Mantle and crustal origins in response to India–Asia collision and convergence. *Geochimica et Cosmochimica Acta*, *143*, 207–231. https://doi.org/10.1016/j.gca.2014.03.031

Lucci, F., Carrasco-Núñez, G., Rossetti, F., Theye, T., White, J. C., Urbani, S., et al. (2020). Anatomy of the magmatic plumbing system of Los Humeros Caldera (Mexico): Implications for geothermal systems. *Solid Earth*, *11*(1), 125–159. https://doi.org/10.5194/se-11-125-2020

Lucci, F., Rossetti, F., White, J. C., Moghadam, H. S., Shirzadi, A., & Nasrabady, M. (2016). Tschermak fractionation in calc-alkaline magmas: The Eocene Sabzevar volcanism (NE Iran). *Arabian Journal of Geosciences*, *9*–10. https://doi.org/10.1007/s12517-016-2598-0

Marschall, H. R., & Schumacher, J. C. (2012). Arc magmas sourced from melange diapirs in subduction zones. *Nature Geoscience*, *5*(12), 862–867. https://doi.org/10.1038/ngeo1634

Maunder, B., van Hunen, J., Magni, V., & Bouilhol, P. (2016). Relamination of mafic subducting crust throughout Earth's history. *Earth and Planetary Science Letters*, *449*, 206–216. https://doi.org/10.1016/j.epsl.2016.05.042

Mayen, J. F., Laurent, O., Chelle-Michou, C., Couzinie, S., Vanderhaeghe, O., Zeh, A., et al. (2017). Collision vs. subduction-related magmatism: Two contrasting ways of granite formation and implications for crustal growth. *Lithos*, *277*, 154–177.

Mazhari, S. A., Klötzli, U., & Safari, M. (2019). Petrological investigation of Late Cretaceous magmatism in Kaboodan area, NE Iran: Evidence for an active continental arc at Sabzevar zone. *Lithos*, *348*, 105183. https://doi.org/10.1016/j.lithos.2019.105183

McBirney, A., Taylor, H., & Armstrong, R. (1987). Paricutin re-examined: A classic example of crustal assimilation in calc-alkaline magma. *Contributions to Mineralogy and Petrology*, *95*(1), 4–20. https://doi.org/10.1007/bf00518026

McQuarrie, N., & van Hinsbergen, D. J. J. (2013). Retrodeforming the Arabia-Eurasia collision zone: Age of collision versus magnitude of continental subduction. *Geology*, *41*(3), 315–318. https://doi.org/10.1130/g33591.1

Meade, F. C., Troll, V. R., Ellam, R. M., Freda, C., Font, L., Donaldson, C. H., & Klonowska, I. (2014). Bimodal magmatism produced by progressively inhibited crustal assimilation. *Nature Communications*, *5*, 4199. https://doi.org/10.1038/ncomms5199

Miller, D. M., Goldstein, S. L., & Langmuir, C. H. (1994). Cerium lead and lead-isotope ratios in arc magmas and the enrichment of lead in the continents. *Nature*, *368*(6471), 514–520. https://doi.org/10.1038/368514a0

Mirnejad, H., Lalonde, A. E., Obeid, M., & Hassanzadeh, J. (2013). Geochemistry and petrogenesis of Mashhad granitoids: An insight into the geodynamic history of the Paleo-Tethys in northeast of Iran. *Lithos*, *170*, 105–116. https://doi.org/10.1016/j.lithos.2013.03.003

Moghadam, H. S., Bröcker, M., Griffin, W. L., Li, X. H., Chen, R. X., & O'Reilly, S. Y. (2017). Subduction, high-P metamorphism, and collision fingerprints in South Iran: Constraints from zircon U-Pb and mica Rb-Sr geochronology. *Geochemistry, Geophysics, Geosystems*, *18*(1), 306–332. https://doi.org/10.1002/2016gc006585

Moghadam, H. S., Corfu, F., Chiaradia, M., Stern, R. J., & Ghorbani, G. (2014). Sabzevar Ophiolite, NE Iran: Progress from embryonic oceanic lithosphere into magmatic arc constrained by new isotopic and geochemical data. *Lithos*, *210*, 224–241. https://doi.org/10.1016/j.lithos.2014.10.004

Moghadam, H. S., Griffin, W. L., Kirchenbaur, M., Garbe-Schönberg, D., Zakie Khedr, M., Kimura, J.-I., et al. (2018). Roll-back, extension and mantle upwelling triggered Eocene potassic magmatism in NW Iran. *Journal of Petrology*, *59*(7), 1417–1465. https://doi.org/10.1093/petrology/egy067

Moghadam, H. S., Khedr, M. Z., Arai, S., Stern, R. J., Ghorbani, G., Tamura, A., & Ottley, C. J. (2015). Arc-related harzburgite–dunite–chromitite complexes in the mantle section of the Sabzevar ophiolite, Iran: A model for formation of podiform chromitites. *Gondwana Research*, *27*(2), 575–593. https://doi.org/10.1016/j.gr.2013.09.007

Moghadam, H. S., Khedr, M. Z., Chiaradia, M., Stern, R. J., Bakhshizad, F., Arai, S., et al. (2014). Supra-subduction zone magmatism of the Neyriz ophiolite, Iran: Constraints from geochemistry and Sr-Nd-Pb isotopes. *International Geology Review*, *56*(11), 1395–1412. https://doi.org/10.1080/00206814.2014.942391

Moghadam, H. S., Li, Q. L., Griffin, W. L., Stern, R. J., Ishizuka, O., Henry, H., et al. (2020). Repeated magmatic buildup and deep "hot zones" in continental evolution: The Cadomian crust of Iran. *Earth and Planetary Science Letters*, *531*, 115989. https://doi.org/10.1016/j.epsl.2019.115989

Moghadam, H. S., Li, Q. L., Griffin, W. L., Stern, R. J., Santos, J. F., Lucci, F., et al. (2021). Prolonged magmatism and growth of the Iran-Anatolia Cadomian continental arc segment in Northern Gondwana. *Lithos*, *384–385*, 105940. https://doi.org/10.1016/j.lithos.2020.105940

Moghadam, H. S., Li, Q. L., Li, X. H., Stern, R. J., Levresse, G., Santos, J. F., et al. (2020). Neotethyan subduction ignited the Iran arc and backarc differently. *Journal of Geophysical Research: Solid Earth*, *125*(5), e2019JB018460. https://doi.org/10.1029/2019jb018460

Moghadam, H. S., Li, X. H., Ling, X. X., Santos, J. F., Stern, R. J., Li, Q. L., & Ghorbani, G. (2015). Eocene Kashmar granitoids (NE Iran): Petrogenetic constraints from U-Pb zircon geochronology and isotope geochemistry. *Lithos*, *216*, 118–135. https://doi.org/10.1016/j.lithos.2014.12.012

Moghadam, H. S., Rossetti, F., Lucci, F., Chiaradia, M., Gerdes, A., Martinez, M. L., et al. (2016). The calc-alkaline and adakitic volcanism of the Sabzevar structural zone (NE Iran): Implications for the Eocene magmatic flare-up in Central Iran. *Lithos*, *248*, 517–535. https://doi.org/10.1016/j.lithos.2016.01.019

Moghadam, H. S., & Stern, R. J. (2011). Geodynamic evolution of Upper Cretaceous Zagros ophiolites: Formation of oceanic lithosphere above a nascent subduction zone. *Geological Magazine*, *148*(5–6), 762–801. https://doi.org/10.1017/s0016756811000410

Moghadam, H. S., Stern, R. J., & Rahgoshay, M. (2010). The Dehshir ophiolite (central Iran): Geochemical constraints on the origin and evolution of the Inner Zagros ophiolite belt. *Geological Society of America Bulletin*, *122*(9–10), 1516–1547. https://doi.org/10.1130/b30066.1

Monsef, I., Monsef, R., Mata, J., Zhang, Z. Y., Pirouz, M., Rezaeian, M., et al. (2018). Evidence for an early-MORB to fore-arc evolution within the Zagros suture zone: Constraints from zircon U-Pb geochronology and geochemistry of the Neyriz ophiolite (South Iran). *Gondwana Research*, *62*, 287–305. https://doi.org/10.1016/j.gr.2018.03.002

Moore, G., & Carmichael, I. S. E. (1998). The hydrous phase equilibria (to 3 kbar) of an andesite and basaltic andesite from western Mexico: Constraints on water content and conditions of phenocryst growth. *Contributions to Mineralogy and Petrology*, *130*(3–4), 304–319. https://doi.org/10.1007/s004100050367

Morimoto, N. (1988). Nomenclature of pyroxenes. *Mineralogy and Petrology*, *39*(1), 55–76. https://doi.org/10.1007/bf01226262

Müntener, O., Kelemen, P. B., & Grove, T. L. (2001). The role of H_2O during crystallization of primitive arc magmas under uppermost mantle conditions and genesis of igneous pyroxenites: An experimental study. *Contributions to Mineralogy and Petrology*, *141*(6), 643–658. https://doi.org/10.1007/s004100100266

Nandedkar, R. H., Hürlimann, N., Ulmer, P., & Müntener, O. (2016). Amphibole–melt trace element partitioning of fractionating calc-alkaline magmas in the lower crust: An experimental study. *Contributions to Mineralogy and Petrology*, *171*(8–9). https://doi.org/10.1007/s00410-016-1278-0

Neill, I., Meliksetian, K., Allen, M. B., Navarsardyan, G., & Karapetyan, S. (2013). Pliocene-Quaternary volcanic rocks of NW Armenia: Magmatism and lithospheric dynamics within an active orogenic plateau. *Lithos*, *180*, 200–215. https://doi.org/10.1016/j.lithos.2013.05.005

Pang, K.-N., Chung, S.-L., Zarrinkoub, M. H., Li, X.-H., Lee, H.-Y., Lin, T.-H., & Chiu, H.-Y. (2016). New age and geochemical constraints on the origin of Quaternary adakite-like lavas in the Arabia–Eurasia collision zone. *Lithos*, *264*, 348–359. https://doi.org/10.1016/j.lithos.2016.08.042

Pang, K.-N., Chung, S.-L., Zarrinkoub, M. H., Wang, F., Kamenetsky, V. S., & Lee, H.-Y. (2015). Quaternary high-Mg ultrapotassic rocks from the Qal'eh Hasan Ali maars, southeastern Iran: Petrogenesis and geodynamic implications. *Contributions to Mineralogy and Petrology*, *170*(3), 27. https://doi.org/10.1007/s00410-015-1183-y

Patchett, P. J. (1980). Thermal effects of basalt on continental-crust and crustal contamination of magmas. *Nature*, *283*(5747), 559–561. https://doi.org/10.1038/283559a0

Portnyagin, M., Duggen, S., Hauff, F., Mironov, N., Bindeman, I., Thirlwall, M., & Hoernle, K. (2015). Geochemistry of the late Holocene rocks from the Tolbachik volcanic field, Kamchatka: Quantitative modelling of subduction-related open magmatic systems. *Journal of Volcanology and Geothermal Research*, *307*, 133–155. https://doi.org/10.1016/j.jvolgeores.2015.08.015

Rapp, R. P., Irifune, T., Shimizu, N., Nishiyama, N., Norman, M. D., & Inoue, T. (2008). Subduction recycling of continental sediments and the origin of geochemically enriched reservoirs in the deep mantle. *Earth and Planetary Science Letters*, *271*(1–4), 14–23. https://doi.org/10.1016/j.epsl.2008.02.028

Rapp, R. P., & Watson, E. B. (1995). Dehydration melting of metabasalt at 8–32 kbar: Implications for continental growth and crust-mantle recycling. *Journal of Petrology*, *36*(4), 891–931. https://doi.org/10.1093/petrology/36.4.891

Reid, M. R., Schleiffarth, W. K., Cosca, M. A., Delph, J. R., Blichert-Toft, J., & Cooper, K. M. (2017). Shallow melting of MORB-like mantle under hot continental lithosphere, Central Anatolia. *Geochemistry, Geophysics, Geosystems*, *18*(5), 1866–1888. https://doi.org/10.1002/2016gc006772

Ridolfi, F., Renzulli, A., & Puerini, M. (2010). Stability and chemical equilibrium of amphibole in calc-alkaline magmas: An overview, new thermobarometric formulations and application to subduction-related volcanoes. *Contributions to Mineralogy and Petrology*, *160*(1), 45–66. https://doi.org/10.1007/s00410-009-0465-7

Rooney, T. O., Franceschi, P., & Hall, C. M. (2011). Water-saturated magmas in the Panama Canal region: A precursor to adakite-like magma generation? *Contributions to Mineralogy and Petrology*, *161*(3), 373–388. https://doi.org/10.1007/s00410-010-0537-8

Rossetti, F., Asti, R., Faccenna, C., Gerdes, A., Lucci, F., & Theye, T. (2017). Magmatism and crustal extension: Constraining activation of the ductile shearing along the Gediz detachment, Menderes Massif (western Turkey). *Lithos*, *282*, 145–162. https://doi.org/10.1016/j.lithos.2017.03.003

Rostami-Hossouri, M., Ghasemi, H., Pang, K.-N., Shellnutt, J. G., Rezaei-Kahkhaei, M., Miao, L., et al. (2020). Geochemistry of continental alkali basalts in the Sabzevar region, northern Iran: Implications for the role of pyroxenite in magma genesis. *Contributions to Mineralogy and Petrology*, *175*(5). https://doi.org/10.1007/s00410-020-01687-z

Sadofsky, S. J., Portnyagin, M., Hoernle, K., & van den Bogaard, P. (2007). Subduction cycling of volatiles and trace elements through the Central American volcanic arc: Evidence from melt inclusions. *Contributions to Mineralogy and Petrology*, *155*(4), 433–456. https://doi.org/10.1007/s00410-007-0251-3

Saginor, I., Gazel, E., Condie, C., & Carr, M. J. (2013). Evolution of geochemical variations along the Central American volcanic front. *Geochemistry, Geophysics, Geosystems*, *14*(10), 4504–4522. https://doi.org/10.1002/ggge.20259

Seghedi, I., Besutiu, L., Mirea, V., Zlagnean, L., Popa, R.-G., Szakács, A., et al. (2019). Tectono-magmatic characteristics of post-collisional magmatism: Case study East Carpathians, Călimani-Gurghiu-Harghita volcanic range. *Physics of the Earth and Planetary Interiors*, *293*, 106270. https://doi.org/10.1016/j.pepi.2019.106270

Sepidbar, F., Mirnejad, H., Ma, C., & Moghadam, H. S. (2018). Identification of Eocene-Oligocene magmatic pulses associated with flare-up in east Iran: Timing and sources. *Gondwana Research*, *57*, 141–156. https://doi.org/10.1016/j.gr.2018.01.008

Sepidbar, F., Shafaii Moghadam, H., Zhang, L., Li, J.-W., Ma, J., Stern, R. J., & Lin, C. (2019). Across-arc geochemical variations in the Paleogene magmatic belt of Iran. *Lithos*, *344–345*, 280–296. https://doi.org/10.1016/j.lithos.2019.06.022

Shabanian, E., Acocella, V., Gioncada, A., Ghasemi, H., & Bellier, O. (2012). Structural control on volcanism in intraplate post collisional settings: Late Cenozoic to Quaternary examples of Iran and Eastern Turkey. *Tectonics*, *31*. https://doi.org/10.1029/2011tc003042

Stampfli, G. M., & Borel, G. D. (2002). A plate tectonic model for the Paleozoic and Mesozoic constrained by dynamic plate boundaries and restored synthetic oceanic isochrons. *Earth and Planetary Science Letters*, *196*(1–2), 17–33. https://doi.org/10.1016/s0012-821x(01)00588-x

Stern, C. R., & Kilian, R. (1996). Role of the subducted slab, mantle wedge and continental crust in the generation of adakites from the Andean Austral Volcanic Zone. *Contributions to Mineralogy and Petrology*, *123*(3), 263–281. https://doi.org/10.1007/s004100050155

Stracke, A. (2012). Earth's heterogeneous mantle: A product of convection-driven interaction between crust and mantle. *Chemical Geology*, *330*, 274–299. https://doi.org/10.1016/j.chemgeo.2012.08.007

Straub, S. M., Goldstein, S. L., Class, C., Schmidt, A., & Gomez-Tuena, A. (2010). Slab and mantle controls on the Sr-Nd-Pb-Hf isotope evolution of the post 42 Ma Izu-Bonin volcanic arc. *Journal of Petrology*, *51*(5), 993–1026. https://doi.org/10.1093/petrology/egq009

Sun, S.-S., & McDonough, W. F. (1989). Chemical and isotopic systematics of oceanic basalts: Implications for mantle composition and processes. *Geological Society, London, Special Publications*, *42*(1), 313–345. https://doi.org/10.1144/gsl.sp.1989.042.01.19

Sun, W. H., & Zhou, M. F. (2008). The similar to 860-Ma, Cordilleran-type Guandaoshan dioritic pluton in the Yangtze Block, SW China: Implications for the origin of neoproterozoic magmatism. *Journal of Geology*, *116*(3), 238–253. https://doi.org/10.1086/587881

Tian, S.-H., Yang, Z.-S., Hou, Z.-Q., Mo, X.-X., Hu, W.-J., Zhao, Y., & Zhao, X.-Y. (2017). Subduction of the Indian lower crust beneath southern Tibet revealed by the post-collisional potassic and ultrapotassic rocks in SW Tibet. *Gondwana Research*, *41*, 29–50. https://doi.org/10.1016/j.gr.2015.09.005

Tiepolo, M., & Tribuzio, R. (2008). Petrology and U–Pb zircon geochronology of amphibole-rich cumulates with sanukitic affinity from Husky Ridge (Northern Victoria Land, Antarctica): Insights into the role of amphibole in the petrogenesis of subduction-related magmas. *Journal of Petrology*, *49*(5), 937–970. https://doi.org/10.1093/petrology/egn012

van der Boon, A., Kuiper, K. F., van der Ploeg, R., Cramwinckel, M. J., Honarmand, M., Sluijs, A., & Krijgsman, W. (2021). Exploring a link between the Middle Eocene Climatic Optimum and Neotethys continental arc flare-up. *Climate of the Past*, *17*(1), 229–239. https://doi.org/10.5194/cp-17-229-2021

Verdel, C., Wernicke, B. P., Hassanzadeh, J., & Guest, B. (2011). A Paleogene extensional arc flare-up in Iran. *Tectonics*, *30*(3). https://doi.org/10.1029/2010tc002809

Verdel, C., Wernicke, B. P., Ramezani, J., Hassanzadeh, J., Renne, P. R., & Spell, T. L. (2007). Geology and thermochronology of Tertiary Cordilleran-style metamorphic core complexes in the Saghand region of central Iran. *Geological Society of America Bulletin*, *119*(7–8), 961–977. https://doi.org/10.1130/b26102.1

Vervoort, J. D., & Blichert-Toft, J. (1999). Evolution of the depleted mantle: Hf isotope evidence from juvenile rocks through time. *Geochimica et Cosmochimica Acta*, *63*(3), 533–556. https://doi.org/10.1016/s0016-7037(98)00274-9

Walker, B. A., Bergantz, G. W., Otamendi, J. E., Ducea, M. N., & Cristofolini, E. A. (2015). A MASH zone revealed: The mafic complex of the Sierra Valle Fertil. *Journal of Petrology*, *56*(9), 1863–1896. https://doi.org/10.1093/petrology/egv057

Wan, B., Deng, C., Najafi, A., Hezareh, M. R., Talebian, M., Dong, L., et al. (2018). Fertilizing porphyry Cu deposits through deep crustal hot zone melting. *Gondwana Research*, *60*, 179–185. https://doi.org/10.1016/j.gr.2018.04.006

Wanless, V., Perfit, M., Ridley, M., & Klein, E. (2010). Dacite petrogenesis on mid-ocean ridges: Evidence for oceanic crustal melting and assimilation. *Journal of Petrology*, *51*(12), 2377–2410. https://doi.org/10.1093/petrology/egq056

White, J. C., Parker, D. F., & Ren, M. (2009). The origin of trachyte and pantellerite from Pantelleria, Italy: Insights from major element, trace element, and thermodynamic modelling. *Journal of Volcanology and Geothermal Research*, *179*(1–2), 33–55. https://doi.org/10.1016/j.jvolgeores.2008.10.007

Willbold, M., & Stracke, A. (2006). Trace element composition of mantle end-members: Implications for recycling of oceanic and upper and lower continental crust. *Geochemistry, Geophysics, Geosystems*, *7*(4). https://doi.org/10.1029/2005gc001005

Willbold, M., & Stracke, A. (2010). Formation of enriched mantle components by recycling of upper and lower continental crust. *Chemical Geology*, *276*(3–4), 188–197. https://doi.org/10.1016/j.chemgeo.2010.06.005

Workman, R. K., & Hart, S. R. (2005). Major and trace element composition of the depleted MORB mantle (DM). *Earth and Planetary Science Letters*, *231*(1–2), 53–72. https://doi.org/10.1016/j.epsl.2004.12.005

Xu, J.-F., Shinjo, R., Defant, M. J., Wang, Q., & Rapp, R. P. (2002). Origin of Mesozoic adakitic intrusive rocks in the Ningzhen area of east China: Partial melting of delaminated lower continental crust? *Geology*, *30*(12), 1111–1114. https://doi.org/10.1130/0091-7613(2002)030<1111:oomair>2.0.co;2

Xu, W.-C., Zhang, H.-F., Luo, B.-J., Guo, L., & Yang, H. (2015). Adakite-like geochemical signature produced by amphibole-dominated fractionation of arc magmas: An example from the Late Cretaceous magmatism in Gangdese belt, south Tibet. *Lithos*, *232*, 197–210. https://doi.org/10.1016/j.lithos.2015.07.001

Zanchetta, S., Berra, F., Zanchi, A., Bergomi, M., Caridroit, M., Nicora, A., & Heidarzadeh, G. (2013). The record of the Late Palaeozoic active margin of the Palaeotethys in NE Iran: Constraints on the Cimmerian orogeny. *Gondwana Research*, *24*(3–4), 1237–1266. https://doi.org/10.1016/j.gr.2013.02.013

Zhang, B., Hu, X., Li, P., Tang, Q., & Zhou, W. (2019). Trace element partitioning between amphibole and hydrous silicate glasses at 0.6–2.6 GPa. *Acta Geochimica*, *38*(3), 414–429. https://doi.org/10.1007/s11631-019-00322-4.,

Zindler, A., & Hart, S. (1986). Chemical geodynamics. *Annual Review of Earth and Planetary Sciences*, *14*(1), 493–571. https://doi.org/10.1146/annurev.ea.14.050186.002425

References From the Supporting Information

Albarède, F. (1996). *Introduction to geochemical modeling*. Cambridge University Press.

Annen, C., Blundy, J. D., & Sparks, R. S. J. (2006). The genesis of intermediate and silicic magmas in deep crustal hot zones. *Journal of Petrology*, *47*(3), 505–539. https://doi.org/10.1093/petrology/egi084

Bacon, C. R., & Druitt, T. H. (1988). Compositional evolution of the zoned calcalkaline magma chamber of Mount Mazama, Crater Lake, Oregon. *Contributions to Mineralogy and Petrology*, *98*(2), 224–256.

Bindeman, I. N., & Davis, A. M. (2000). Trace element partitioning between plagioclase and melt: Investigation of dopant influence on partition behavior. *Geochimica et Cosmochimica Acta*, *64*(16), 2863–2878.

Bindeman, I. N., Davis, A. M., & Drake, M. J. (1998). Ion microprobe study of plagioclase-basalt partition experiments at natural concentration levels of trace elements. *Geochimica et Cosmochimica Acta*, *62*(7), 1175–1193.

Bowles, J., Howie, R., Vaughan, D., & Zussman, J. (2011). *Rock-forming minerals: Volume 5A non-silicates: Oxides, hydroxides and sulphides* (2nd ed., pp. 237–239). The Geological Society.

Brenan, J. M., Shaw, H. F., Ryerson, F. J., & Phinney, D. L. (1995). Experimental-determination of trace-element partitioning between pargasite and a synthetic hydrous andesitic melt. *Earth and Planetary Science Letters*, *135*(1–4), 1–11.

Bryan, W. B., Finger, L. W., & Chayes, F. (1969). Estimating proportions in petrographic mixing equations by least-squares approximation. *Science*, *163*(3870), 926–927.

Daneshvar, N., Maanijou, M., Azizi, H., & Asahara, Y. (2019). Petrogenesis and geodynamic implications of an Ediacaran (550 Ma) granite complex (metagranites), southwestern Saqqez, northwest Iran. *Journal of Geodynamics*, *132*, 101669.

Deer, W., Howie, R., & Zussman, J. (1997). Rock-forming minerals. *Double chain silicates* (Vol. *2B*, p. 764). The Geological Society Publishing House.

Deer, W. A., Howie, R. A., & Zussman, J. (2001). *Rock-forming minerals: Feldspars* (Vol. *4A*). Geological Society of London.

DePaolo, D. J. (1981a). A neodymium and strontium isotopic study of the Mesozoic calc-alkaline granitic batholiths of the Sierra Nevada and Peninsular Ranges, California. *Journal of Geophysical Research: Solid Earth*, *86*(B11), 10470–10488.

Depaolo, D. J. (1981b). Trace element and isotopic effects of combined wallrock assimilation and fractional crystallization. *Earth and Planetary Science Letters*, *53*(2), 189–202.

Elkins, L., Gaetani, G., & Sims, K. (2008). Partitioning of U and Th during garnet pyroxenite partial melting: Constraints on the source of alkaline ocean island basalts. *Earth and Planetary Science Letters*, *265*(1–2), 270–286. https://doi.org/10.1016/j.epsl.2007.10.034

Ewart, A., & Griffin, W. (1994). Application of proton-microprobe data to trace-element partitioning in volcanic rocks. *Chemical Geology*, *117*(1–4), 251–284.

Fujimaki, H., Tatsumoto, M., & Aoki, K. i. (1984). Partition coefficients of Hf, Zr, and REE between phenocrysts and groundmasses. *Journal of Geophysical Research: Solid Earth*, *89*(S02), B662–B672.

Galer, S. J. G., & Abouchami, W. (1998). Practical application of lead triple spiking for correction of instrumental mass discrimination. *Mineralogical Magazine*, *62*, 491–492.

Garbe-Schönberg, C. D. (1993). Simultaneous determination of thirty-seven trace elements in twenty-eight international rock standards by ICP-MS. *Geostandards Newsletter*, *17*(1), 81–97.

Ginibre, C., & Worner, G. (2007). Variable parent magmas and recharge regimes of the Parinacota magma system (N. Chile) revealed by Fe, Mg and Sr zoning in plagioclase. *Lithos*, *98*(1–4), 118–140. https://doi.org/10.1016/j.lithos.2007.03.004

Griffin, W. L., Wang, X., Jackson, S. E., Pearson, N. J., O'Reilly, S. Y., Xu, X. S., & Zhou, X. M. (2002). Zircon chemistry and magma mixing, SE China: In-situ analysis of Hf isotopes, Tonglu and Pingtan igneous complexes. *Lithos*, *61*(3–4), 237–269. https://doi.org/10.1016/S0024-4937(02)00082-8

Hawkesworth, C., Blake, S., Evans, P., Hughes, R., Macdonald, R., Thomas, L., et al. (2000). Time scales of crystal fractionation in magma chambers—Integrating physical, isotopic and geochemical perspectives. *Journal of Petrology*, *41*(7), 991–1006.

Hidalgo, P. J., Vogel, T. A., Rooney, T. O., Currier, R. M., & Layer, P. W. (2011). Origin of silicic volcanism in the Panamanian arc: Evidence for a two-stage fractionation process at El Valle volcano. *Contributions to Mineralogy and Petrology*, *162*(6), 1115–1138. https://doi.org/10.1007/s00410-011-0643-2

Higuchi, H., & Nagasawa, H. (1969). Partition of trace elements between rock-forming minerals and the host volcanic rocks. *Earth and Planetary Science Letters*, *7*(3), 281–287.

Hirata, T. (1996). Lead isotopic analysis of NIST standard reference materials using multiple-collector-inductively coupled plasma mass spectrometry coupled with modified external correction method for mass discrimination effect. *Analyst*, *121*, 1407–1411.

Irving, A. J., & Frey, F. A. (1984). Trace element abundances in megacrysts and their host basalts: Constraints on partition coefficients and megacryst genesis. *Geochimica et Cosmochimica Acta*, *48*(6), 1201–1221.

Karlstrom, L., Dufek, J., & Manga, M. (2010). Magma chamber stability in arc and continental crust. *Journal of Volcanology and Geothermal Research*, *190*(3–4), 249–270. https://doi.org/10.1016/j.jvolgeores.2009.10.003

Kay, R. W. (1980). Volcanic arc magmas: Implications of a melting-mixing model for element recycling in the crust-upper mantle system. *Journal of Geology*, *88*(5), 497–522.

Klein, M., Stosch, H.-G., & Seck, H. (1997). Partitioning of high field-strength and rare-earth elements between amphibole and quartz-dioritic to tonalitic melts: An experimental study. *Chemical Geology*, *138*(3–4), 257–271.

Klemme, S., Günther, D., Hametner, K., Prowatke, S., & Zack, T. (2006). The partitioning of trace elements between ilmenite, ulvospinel, armalcolite and silicate melts with implications for the early differentiation of the moon. *Chemical Geology*, *234*(3–4), 251–263. https://doi.org/10.1016/j.chemgeo.2006.05.005

Korkisch, J., & Hazan, I. (1965). Anion exchange separations in hydrobromic acid-organic solvent media. *Analytical Chemistry*, *37*, 707–710.

LaTourrette, T., Hervig, R. L., & Holloway, J. R. (1995). Trace element partitioning between amphibole, phlogopite, and basanite melt. *Earth and Planetary Science Letters*, *135*(1–4), 13–30.

Lee, C. T. A., Lee, T. C., & Wu, C. T. (2014). Modeling the compositional evolution of recharging, evacuating, and fractionating (REFC) magma chambers: Implications for differentiation of arc magmas. *Geochimica et Cosmochimica Acta*, *143*, 8–22. https://doi.org/10.1016/j.gca.2013.08.009

Li, X. H., Long, W. G., Li, Q. L., Liu, Y., Zheng, Y. F., Yang, Y. H., et al. (2010). Penglai zircon megacrysts: A potential new working reference material for microbeam determination of Hf-O isotopes and U-Pb age. *Geostandards and Geoanalytical Research*, *34*(2), 117–134. https://doi.org/10.1111/j.1751-908X.2010.00036.x

Li, X. H., Tang, G. Q., Gong, B., Yang, Y. H., Hou, K. J., Hu, Z. C., et al. (2013). Qinghu zircon: A working reference for microbeam analysis of U-Pb age and Hf and O isotopes. *Chinese Science Bulletin*, *58*(36), 4647–4654. https://doi.org/10.1007/s11434-013-5932-x

Lucci, F., Carrasco-Núñez, G., Rossetti, F., Theye, T., White, J. C., Urbani, S., et al. (2020). Anatomy of the magmatic plumbing system of Los Humeros Caldera (Mexico): Implications for geothermal systems. *Solid Earth*, *11*(1), 125–159. https://doi.org/10.5194/se-2019-86

Lucci, F., Rossetti, F., White, J. C., Moghadam, H. S., Shirzadi, A., & Nasrabady, M. (2016). Tschermak fractionation in calc-alkaline magmas: The Eocene Sabzevar volcanism (NE Iran). *Arabian Journal of Geosciences*, *9*(10), 573. https://doi.org/10.1007/s12517-016-2598-0

Ludwig, K. R. (2003). *User's manual for isoplot 3.00: A geochronological toolkit for Microsoft Excel.*

Luhr, J. F., & Carmichael, I. S. (1980). The colima volcanic complex, Mexico. *Contributions to Mineralogy and Petrology*, *71*(4), 343–372.

Mahood, G., & Hildreth, W. (1983). Large partition coefficients for trace elements in high-silica rhyolites. *Geochimica et Cosmochimica Acta*, *47*(1), 11–30.

McKenzie, D., & O'nions, R. (1991). Partial melt distributions from inversion of rare earth element concentrations. *Journal of Petrology*, *32*(5), 1021–1091.

Moghadam, H. S., Khademi, M., Hu, Z. C., Stern, R. J., Santos, J. F., & Wu, Y. B. (2015). Cadomian (Ediacaran-Cambrian) arc magmatism in the ChahJam-Biarjmand metamorphic complex (Iran): Magmatism along the northern active margin of Gondwana. *Gondwana Research*, *27*(1), 439–452. https://doi.org/10.1016/j.gr.2013.10.014

Moghadam, H. S., Li, Q. L., Griffin, W. L., Stern, R. J., Ishizuka, O., Henry, H., et al. (2020). Repeated magmatic buildup and deep "hot zones" in continental evolution: The Cadomian crust of Iran. *Earth and Planetary Science Letters*, *531*. https://doi.org/10.1016/j.epsl.2019.115989

Moghadam, H. S., Li, Q. L., Griffin, W. L., Stern, R. J., Santos, J., Lucci, F., et al. (2021). Prolonged magmatism and growth of the Iran-Anatolia Cadomian continental arc segment in Northern Gondwana. *Lithos*, *384–385*, 105940. https://doi.org/10.1016/j.lithos.2020.105940

Moghadam, H. S., Li, X. H., Santos, J. F., Stern, R. J., Griffin, W. L., Ghorbani, G., & Sarebani, N. (2017). Neoproterozoic magmatic flare-up along the N. margin of Gondwana: The Taknar complex, NE Iran. *Earth and Planetary Science Letters*, *474*, 83–96. https://doi.org/10.1016/j.epsl.2017.06.028

Munker, C., Weyer, S., Scherer, E., & Mezger, K. (2001). Separation of high field strength elements (Nb, Ta, Zr, Hf) and Lu from rock samples for MC-ICPMS measurements. *Geochemistry, Geophysics, Geosystems*, *2*. https://doi.org/10.1029/2001GC000183

Nasdala, L., Hofmeister, W. G., Norberg, N., Mattinson, J. M., Corfu, F., Dorr, W., et al. (2008). Zircon M257 - A homogeneous natural reference material for the ion microprobe U-Pb analysis of zircon. *Geostandards and Geoanalytical Research*, *32*(3), 247–265. https://doi.org/10.1111/j.1751-908X.2008.00914.x

Nicholls, I., & Harris, K. (1980). Experimental rare earth element partition coefficients for garnet, clinopyroxene and amphibole coexisting with andesitic and basaltic liquids. *Geochimica et Cosmochimica Acta*, *44*(2), 287–308.

Paster, T. P., Schauwecker, D. S., & Haskin, L. A. (1974). The behavior of some trace elements during solidification of the Skaergaard layered series. *Geochimica et Cosmochimica Acta*, *38*(10), 1549–1577.

Pin, C., Gannoun, A., & Dupont, A. (2014). Rapid, simultaneous separation of Sr, Pb, and Nd by extraction chromatography prior to isotope ratios determination by TIMS and MC-ICP-MS. *Journal of Analytical Atomic Spectrometry*, *29*(10), 1858–1870. https://doi.org/10.1039/C4JA00169A

Pin, C., & Zalduegui, J. F. S. (1997). Sequential separation of light rare-earth elements, thorium and uranium by miniaturized extraction chromatography: Application to isotopic analyses of silicate rocks. *Analytica Chimica Acta*, *339*, 79–89.

Powell, R. (1984). Inversion of the assimilation and fractional crystallization (AFC) equations; characterization of contaminants from isotope and trace element relationships in volcanic suites. *Journal of the Geological Society*, *141*(3), 447–452.

Rayleigh, L. (1896). L. Theoretical considerations respecting the separation of gases by diffusion and similar processes: The London, Edinburgh, and Dublin. *Philosophical Magazine and Journal of Science*, *42*(259), 493–498.

Ridolfi, F., Renzulli, A., & Puerini, M. (2010). Stability and chemical equilibrium of amphibole in calc-alkaline magmas: An overview, new thermobarometric formulations and application to subduction-related volcanoes. *Contributions to Mineralogy and Petrology*, *160*(1), 45–66. https://doi.org/10.1007/s00410-009-0465-7

Rossetti, F., Nasrabady, M., Theye, T., Gerdes, A., Monie, P., Lucci, F., & Vignaroli, G. (2014). Adakite differentiation and emplacement in a subduction channel: The late Paleocene Sabzevar magmatism (NE Iran). *Geological Society of America Bulletin*, *126*(3–4), 317–343. https://doi.org/10.1130/B30913.1

Schnetzler, C., & Philpotts, J. A. (1970). Partition coefficients of rare-earth elements between igneous matrix material and rock-forming mineral phenocrysts—II. *Geochimica et Cosmochimica Acta*, *34*(3), 331–340.

Schuth, S., Konig, S., & Münker, C. (2011). Subduction zone dynamics in the SW Pacific plate boundary region constrained from high-precision Pb isotope data. *Earth and Planetary Science Letters*, *311*(3–4), 328–338. https://doi.org/10.1016/j.epsl.2011.09.006

Sepidbar, F., Moghadam, H. S., Li, C., Stern, R. J., Jiantang, P., & Vesali, Y. (2020). Cadomian magmatic rocks from zarand (SE Iran) formed in a retro-arc basin. *Lithos*, *366–367*. https://doi.org/10.1016/j.lithos.2020.105569

Sisson, T. (1994). Hornblende-melt trace-element partitioning measured by ion microprobe. *Chemical Geology*, *117*(1–4), 331–344.

Slama, J., Kosler, J., Condon, D. J., Crowley, J. L., Gerdes, A., Hanchar, J. M., et al. (2008). Plesovice zircon—A new natural reference material for U-Pb and Hf isotopic microanalysis. *Chemical Geology*, *249*(1–2), 1–35. https://doi.org/10.1016/j.chemgeo.2007.11.005

Stacey, J. S., & Kramers, J. D. (1975). Approximation of terrestrial lead isotope evolution by a 2-stage model. *Earth and Planetary Science Letters*, *26*(2), 207–221.

White, J. C., Parker, D. F., & Ren, M. (2009). The origin of trachyte and pantellerite from Pantelleria, Italy: Insights from major element, trace element, and thermodynamic modelling. *Journal of Volcanology and Geothermal Research*, *179*(1–2), 33–55. https://doi.org/10.1016/j.jvolgeores.2008.10.007

Whitney, D. L., & Evans, B. W. (2010). Abbreviations for names of rock-forming minerals. *American Mineralogist*, *95*(1), 185–187. https://doi.org/10.2138/am.2010.3371

Wu, F. Y., Yang, Y. H., Xie, L. W., Yang, J. H., & Xu, P. (2006). Hf isotopic compositions of the standard zircons and baddeleyites used in U-Pb geochronology. *Chemical Geology*, *234*(1–2), 105–126. https://doi.org/10.1016/j.chemgeo.2006.05.003

Zack, T., & Brumm, R. (1998). Ilmenite/liquid partition coefficients of 26 trace elements determined through ilmenite/clinopyroxene partitioning in garnet pyroxenites. *Proceedings International Kimberlite Conference: Extended Abstracts* (Vol. *7*, pp. 986–988).